Ph.D. Thesis

Université de Limoges

University of Limoges

ED 609 - Sciences et Ingénierie des Matériaux, Mécanique, Énergétique (SIMME)

Institut de Recherche sur les Céramiques (IRCER)

A thesis submitted to University of Limoges
in partial fulfilment of the requirements of the degree of
Doctor of Philosophy

Discipline / Speciality : Matériaux céramiques et traitements de surface

Presented and defensed by
Nilesh DHONDOO

On May 24, 2022

Non-OXIde ceramic SHAPing: towards an integrated multi-analysis platform to monitor in situ polycarbosilane syntheses

Thesis supervisor: Romain LUCAS and Maggy COLAS

JURY:

President of jury
Mme. Anne LERICHE – Professeur, LMCPA, Université de Valenciennes

Reporters
M. Guy SCHLATTER – Professeur, ICPEES, Université de Strasbourg
M. Patrice BOURSON – Professeur, LMOPS, Université de Lorraine

Examiners
Mme. Sylvie FOUCAUD – Professeur, IRCER, Université de Limoges
Mme. Anne LERICHE – Professeur, LMCPA, Université de Valenciennes
M. Romain LUCAS – Maître de Conférences, IRCER, Université de Limoges
Mme. Maggy COLAS – Chargé de Recherche CNRS, IRCER, Université de Limoges

Guests
Mme. Julie CORNETTE – Ingénieure d'études, IRCER, Université de Limoges

The highest forms of understanding we can achieve are laughter and human compassion.
Richard P. Feynman

Acknowledgements

This research work has been carried out within the Institute of Research on Ceramics (IRCER, UMR CNRS 7315) in Limoges.

First of all, I would like to thank Philippe THOMAS, director of the IRCER, for having welcomed me in the laboratory during these three years and a half.

I also want to thank Professor Anne LARICHE from Laboratoire des Matériaux Céramiques et Procédés Associés (LMCPA) – University of Valenciennes for having accepted to chair the thesis jury. I express my sincere thanks to both examiners of my work Professor Guy SCHLATTER from L'Institut de chimie et procédés pour l'énergie, l'environnement et la santé (ICPEES) – University of Strasbourg and Professor Patrice BOURSON from Laboratoire Matériaux Optiques, Photonique et Systèmes (LMOPS) – University of Lorraine.

Moreover, I thank sincerely my supervisors: Mr Romain Lucas, Mrs Maggy Colas, Mrs Sylvie Foucaud and Mrs Julie Cornette for their constant guidance, availability and especially their unconditional support during those three years and a half. I am grateful to have grown both professionally and humanely along their side and to have benefited from their scientific knowledge.

A big thank you to all the people with whom I had the pleasure to work and exchange about everything and anything. I think of Maxime.B, David, Lucas, Remi, Maxime.C, Camille, Mariana, Eva, Gabriel, Innocent, Khaoula, Hatim, Melanie and Sam.

I would like to thank my Romanian family who took care of me while I was in Romania for my studies namely: Camelia Radulescu who had a big influence on my life and who was always here for me when needed. She instilled the love of Mathematics and helped to develop my curiosity towards Science. Thank you for everything you do for me on a daily basis. Stefan Simionescu, Alin Alesce, Robert Maria and Miruna Ramsamy accompanied me during my journey abroad. I value their friendship as I would not be where I am today without them. A special thanks to Professor Corneliu Balan who took me under his wing during my undergraduate study. Thank you Professor to be among one of my gurus in my life. A special mention to everyone in the Rheolab; Professor Diana Brobana, Nicoleta, Rodica, Ioana, Miga, Claudiu, Eugen and Istvan.

I would like to thank my group of friends in France (Luciana, Silvia, Pauline, Ricardo, Melanie and Polo) who have supported me during my thesis. Without them I would not have been able to finish my thesis. They took care of me when I was sick and for this I will be forever thankful. Thank you guys for being part of my life. Virgil, Sofia,

Innocent, Nassim and Ida are other people who deserve to be mentioned in my thank you list.

Last but not the least thanks go to my dear parents and my sister who sacrificed a lot to see me succeed. If I got here it is because of their unwavering support during all these years. Thank you mum and dad for guiding me in the right path since day one. I feel your love every day in my life. Thanks also to the rest of my childhood friends (Ramjee, Ryan Ravi, Akheelesh, Toshan,Divesh, Vidish and Sandeep) and family for always being there to support me.

Rights

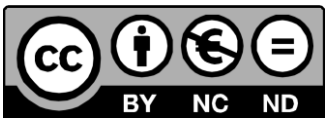

Table of Contents

List of abbreviations

Abbreviation	Significance
AM	Additive Manufacturing
AlOR-PCS	Al-O-Si bonded with PCS
Alac	Aluminium acetylacetonate
ATR	Attenuated Total Reflectance
BDAM	Bis(azidomethyl)dimethysilane
BDSB	1,4-bis(dimethylsilyl)benzene
CMC	Ceramic Matrix Composite
CP	Cone-Plate configuration
CVD	Chemical Vapour Deposition
DA	Diels-Alder
DFT	Density Function Theory
DIW	Direct Ink Writing
EMS	Expandable Microspheres
FTIR	Fourier Transform Infrared
G’	Storage modulus
G’’	Loss modulus
HIPS	High-Impact Polystyrene
HPCS	Hydridopolycarbosilanes
LHBPCS	Liquid hyperbranched polycarbosilane
MALS	Multi-angle Light Scattering
MTES	Methyltriethoxysilane
NMR	Nuclear Magnetic Resonance Spectroscopy
PAN	Polyacrylonitrile
PDMS	Poly(dimethylsilane)
PDCs	Polymer Derived Ceramics
PCMS	Polycarbomethysilane sample
PCS	Polycarbosilanes
PHB	Poly(3-hydroxybutyrate)
Polymer MK	Polymethysilsesquioxane
PP	Plate-Plate configuration
RBF	Round Bottom Flask
Rheo-Raman	Rheometer coupled with a Raman

	spectrometer
Rheo-FTIR	Rheometer coupled with a FTIR spectrometer
Rheo-Raman-FTIR	Rheometer coupled with FTIR and Raman spectrometers
RMS	Root mean square radius
SEC	Size Exclusion Chromatography
SEM	Scanning Electron Microscopy
TA	Tannic Acid
TAS	TetraAllySilane
TBPB	Tert-Butyl PeroxyBenzoate
TEOS	Tetraethoxysilane
TGA	Thermogravimetric Analysis
TPA	TriPropargylAmine
VER	Vinyl Ester Resin
XRD	X-Ray Diffraction

List of Figures

List of Tables

General introduction

Non-oxide ceramics are considered potential candidates for high-temperature applications, due to their good refractoriness and thermomechanical properties. Among non-oxide ceramics, silicon carbide is of particular interest in this project. One way of obtaining SiC is *via* the polymer derived ceramics (PDCs) route. Through the PDCs strategy, several preceramic precursors containing silicon element were initially studied. In this study, as our interest is in developing silicon carbide, from a polymer having elements such as Si, C and H, polycarbosilanes (PCSs) are the appropriate choice. The structures of these polymers influence the chemical composition, ceramic yield, oxidation resistance and the mechanical properties of the resulting ceramic. A perfect knowledge of the synthesised polymers is the best way to understand and to predict their shaping and thermal behaviour. This involves the use of controlled polymerisation reactions, to generate well-defined microstructures of the materials during the ceramisation of the precursor. In addition, the PDCs route can be combined with numerous shaping processes such as casting, fibre drawing or aerosolspraying. However, the link between the rheology of preceramic polymers and the shaping processes is not well documented in the literature. Therefore, the objective of this thesis is to study the evolution of viscosity during the polymerisation of preceramic precursors and to correlate it to shaping processes. However, the viscosity depends on the developing macromolecular structure during the polymerisation reaction. Hence, it is essential to carry out both structural and rheological monitoring of the polymerisation process.

To achieve this goal, the development of a unique platform dedicated to the monitoring of carbosilane polymerisation has therefore been carried out. The newly designed platform can be divided into two parts. The first one includes a rheometer coupled with a Fourier transform infrared spectrometer (FTIR) and a Raman spectrophotometer (Rheo-Raman-FTIR setup). The second part is made of a Size-Exclusion Chromatography with a Multi-Angle Light Scattering (SEC-MALS). The link between these two parts is made by the conversion rate of the preceramic polymer obtained in each case by vibrational spectroscopy (Raman/IR).

The challenge is to adapt, for each part of the platform, the collection of vibrational information to the dedicated assembly. The Rheo-Raman-FTIR setup consists of an attenuated total reflectance (ATR) and a Raman spectrometer, coupled on a rheometer. This setup will combine both the rheological properties and the conversion rate obtained by vibrational spectroscopies as a function of the polymerisation time. As mentioned above, knowledge of the macromolecular structure in real time would be an important asset in understanding the rheology of these systems. During the polymerisation reaction, sampling in round bottom flask (RBF) will be carry out followed by an analysis of the samples with the help of the SEC-MALS. The SEC-MALS will provide real-time information about the structure

of the macromolecules in terms of average molar mass, molar-mass dispersity or conformation of the polymer. A Raman spectrometer associated to an immersion probe will then monitor the polymerisation reaction in RBF, the conversion rate will be determined. The monitoring performed by the Raman spectroscopy can, thus, synchronise the kinetics of the reactions in RBF to that on the rheometer. The establishment of this unique platform therefore constitutes an important step in the understanding the rheology of preceramic polymers.

The first chapter of this manuscript will be devoted to the bibliographical study of SiC systems, focusing firstly on their intrinsic physico-chemical properties and the different routes to synthesise SiC carbide. Moreover, the different steps to obtain a ceramic material *via* the PDCs route are presented. The existing studies on the rheology of preceramic polymers will be reviewed, with a particular focus on two shaping processes *i.e.* fibre drawing and direct ink writing (DIW). In addition, the relationship between changes in molecular structure and rheology will be highlighted with an emphasis on existing coupling setups such as Rheo-Raman and Rheo-FTIR. Finally, the development of the new platform will be presented with the risks associated with the real-time monitoring of preceramic precursors.

The second chapter will present the various physico-chemical characterisation techniques used, as well as the polymerisation protocol for the synthesis of a hyperbranched polycarbosilanes. Vibrational characterisation of reagents will be detailed. Moreover, post processing of Raman and FTIR spectra will be explained and a theoretical approach *via* the theory of the functional density will point out the specificities of the vibrational responses of the molecules studied.

The third chapter will highlight the relationship between kinetics of polymerisation and rheological behaviour of preceramic polymer. The characterisation of the synthesised polycarbosilanes will be performed *via* ^{1}H, ^{13}C and ^{29}Si NMR spectroscopies, TGA, SEM and XRD. The optimisation of the Rheo-Raman-FTIR setup in terms of gap distance, intensity of the Raman signal, impact of catalyst concentration, homogeneity of the reaction medium across the geometry will be presented. Ultimately, after optimising the Rheo-Raman-FTIR setup, the results obtained from monitoring the polymerisation reaction in real time will be discussed.

The fourth and last chapter will highlight how the structure of the macromolecules affect the rheological behaviour of preceramic polymer. The optimisation of the sampling process in RBF will be carried out and the collected samples will be analysed *via* the SEC-MALS in terms of average molar mass, molar-mass dispersity, and conformation of the polymer structure. Finally, the relationship between monomer conversion, average molar mass of the collected sample and the viscosity of the medium will be illustrated.

This manuscript will end with a general conclusion that will summarise the main results obtained in the different chapters and will propose some perspectives drawn from this thesis work.

Chapter 1.

Bibliographic study

1.1. Introduction

The challenges lying ahead in the structural material area consist in the development of materials operating in severe environments, such as at high temperatures (T > 1400 °C), heavy loads, and high corrosion or under oxidising atmospheres. The targeted application sectors are nuclear, aeronautic propulsion, or the steel industry [PI18]. In these different application areas, the issues are: to enhance the performance and the lightness of structural materials, to reduce the fabrication cycles by decreasing the assemblage operations, to improve the lifetime, the performance, and the consumption of these systems [SA13] [RI92] [RI98]. To answer these criteria, non-oxide ceramics are good candidates [CO02] [RI06]. Among them, silicon-based ceramics and composites present excellent thermomechanical properties such as high strength, hardness, and low density [BO87]. In addition, their oxidation, and corrosion resistance make them valuable high-temperature materials [BA96] [LI09]. Several types of processing techniques such as chemical vapour deposition (CVD), arc discharging, powder technology, or even self-propagating high-temperature synthesis (SHS) have been developed to produce non-oxide ceramics [LE17] [VA06] [NA86]. However, even among these different techniques, powder technology is still considered the most popular one for the manufacturing of non-oxide ceramics. Limitations arising from these conventional techniques such as lack of control on oxygen content and the search for novel covalently bonded materials (e.g.SiBCN) have encouraged the development of alternative processing technologies. Since Yajima and co-workers reported the conversion of polycarbosilanes to silicon carbide, much attention has been focused on the structure and properties of polycarbosilanes and more generally on the polymer-derived ceramics (PDCs) [YA76]. Before describing the PDCs route, the focus will be on the structures, properties, and synthesis of SiC.

1.2. Structures and properties of SiC

For the last ten years, SiC has gained significant importance for high power, high-temperature electronic devices as well as abrasion and cutting applications, due to its distinct properties [SA04]. SiC is accessible in amorphous, single-crystalline, or polycrystalline structures [AB11]. The relationship between Si atoms and C atoms in SiC crystal structure is such that each Si atom is tetrahedrally bonded to four carbon atoms or vice versa as shown in Figure 1.1a [RA17]. The distance between the carbon and silicon atom is 189 pm while between the carbon atoms is 308 pm.

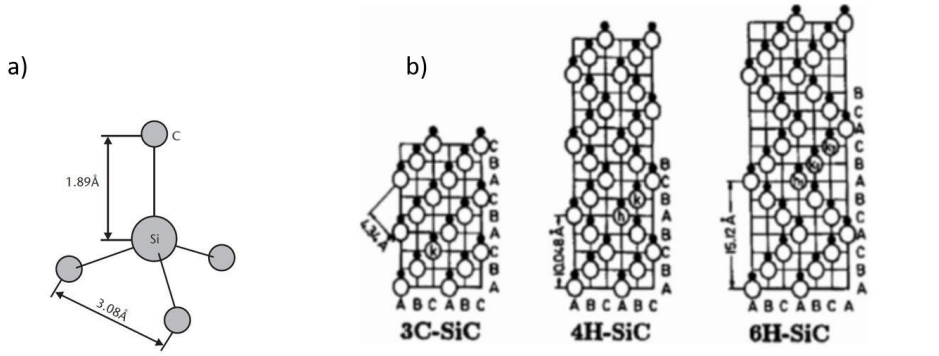

Figure 1.1. a) SiC crystal structure; b) stacking sequence of famous polytypes with Ramsdell notation [RA17].

Nowadays, approximately 50 different polytypes are known. However, among them, the most famous SiC polytypes are 3C-SiC, 4H-SiC, and 6H-SiC (Figure 1.1b). This is due to their attractive electrical and physical characteristics. 3C-Si referrs to as beta silicon carbide (β-SiC), has a zinc blende structure that is the substitution structure of diamond. The remaining two (4H-SiC and 6H-SiC) are known as alpha silicon carbides (α-SiC), which are represented by a combination of zinc blende and Wurtzite structures. α-SiC displays polytypes in which the stacking sequence changes but the layer units are similar. SiC is made up of light elements (Si, C) and has a strong covalency. It is lightweight, has high hardness, high thermal conductivity, a low thermal expansion coefficient, and a high strength. Furthermore, it is a promising ceramic for substituting conventional metals and ionic-bonded oxide ceramics such as aluminum. Moreover, SiC is useful in many industrial fields for its mechanical properties as well as its ability to withstand abrasion [MO94]. At room temperature, it reacts poorly with any known material demonstrating that it is chemically inert. It is practically unachievable to diffuse anything into SiC, even dopants need to be grafted or grown into the material [FA13]. Finally, SiC has outstanding chemical and thermal stability which enables it to operate at high temperatures in hostile environments such as corrosive atmospheres, thanks to its physicochemical properties [HI13]. The oxidation resistance of SiC has been reported extensively in literature review [BA92] [BA96] [BR18] [GU72] [HA13] [HE90] [HI76] [JA13] [VA90]. Oxidation of silicon carbide obeys indeed two different mechanisms namely passive and active oxidation. These mechanisms depend on both the oxygen partial pressure and temperature. According to equation 1.1, the passive oxidation that occurs generally at low temperature and high oxygen partial pressure forms a silica protective layer under these conditions that acts as a diffusion barrier against gaseous oxidant species and limits the kinetics of SiC oxidation [JA13].

$$SiC(s) + \frac{3}{2}O_2(g) \rightarrow SiO_2(s) + CO(g). \qquad \text{Eq. (1.1)}$$

In contrast, active oxidation, which takes place at high temperatures and low oxygen partial pressures, results in the formation of volatile oxides such as SiO(g) and CO(g) (equation 1.2). Consequently, no protective silica layer is developed [JA13]. A significant mass loss of SiC is noted according to the reaction:

$$SiC(s) + O_2(g) \rightarrow SiO(g) + CO(g) \qquad \text{Eq. (1.2)}$$

High hardness and strength, chemical and thermal stability, oxidation resistance are among some notable properties of SiC. However, these properties are influenced by the synthesis process selected. Indeed, the properties of SiC will vary according to various synthesis methods of SiC. Therefore, a processing method that allows us to have control over the final properties of the SiC will be favoured.

1.3. Synthesis of SiC

Since Acheson reported the production process of SiC in 1893, numerous works have since been published on the synthesis of SiC [AC93]. Different synthesis routes of SiC will be presented starting with the traditional Acheson process, which paved the way for the commercialisation of SiC. An overview of the most common methods of elaboration of SiC will be focused on such as chemical vapour deposit, sol-gel, or even polymer-derived ceramics (PDCs). These miscellaneous synthesis approaches proposed in the literature review can be classified into solid, gas, or liquid routes.

1.3.1. Solid route

Jöns Jacob Berzelius is mostly known for his discovery of silicon. In 1824, he published a paper where he figured out that there was a chemical bond between silicon atom Si and carbon C in one of the samples he had produced [BE24]. Years later, in 1893, E.G. Acheson came up with SiC during an experiment on the synthesis of diamond. He named the new substance carborundum since he thought it was a compound of the carbon used in the experiment [AC93]. The Acheson process developed the mass production of silicon carbide [GU97]. The chemical reaction for manufacturing SiC was carried out at high temperatures (above 2500 °C) between silica (SiO_2) and carbon and the overall reaction is written as:

$$SiO_2(s) + 3C(s) \rightarrow SiC(s) + 2CO(g) \qquad \text{Eq. (1.3)}$$

The carbothermal reduction of SiO_2 with carbon in an inert atmosphere at a given temperature is one of the most common methods in the industrial synthesis of carbides as it is simple to implement. However, the reaction time is normally too long, around 10-20 h, and the reduction reaction does not favour homogeneity due to diffusion gradients. Another drawback is that the produced SiC possesses large grains and batches, normally demanding grinding, and purification processes for further usage [WE93] [KO98]. Consequently, poor

quality material is obtained from synthesising SiC powder by the traditional carbothermal reduction method.

1.3.2. Gas route

Elaboration techniques such as chemical vapour deposition (CVD) are employed where metallic elements are converted into a gaseous metal halide. The latter will react with methane or hydrogen by the substitution reaction to produce gaseous SiC that condenses on a substrate. SiC has common precursors such as methyltrichlorosilane (CH_3SiCl_3) or silanes SiH_4 [LO95] [LI89]. The synthesis by CVD generates powders with a low concentration of impurities and a fine particle size (less than one micrometre). It also has the advantage of using lower temperatures and shorter reaction times compared to the solid route. The principal uses of CVD for SiC are coating of materials to inhibit oxidation, densification of porous ceramics, and fabrication of structural parts such as turbine wheels [MI87]. However, disadvantages concerning this route are the presence of excess carbon obtained in the final product and the safety measures needed when dealing with silane gas due to its flammability, toxicity, and explosiveness [SC13] [KU04]. In addition, more time and development are needed to convert the laboratory synthesis process into an industrial scale process.

1.3.3. Liquid route

The last route to be considered to synthesise silicon carbide is the liquid route which can be categorised into two types: a) sol-gel method and b) the polymer-derived ceramics (PDCs) route. The PDCs route can undergo numerous shaping processes, unlike the solid route. Compared to the sol-gel, the PDCs route have the advantage of not having drying difficulties which could prevent the production of bulk components. Moreover, they require less processing time (the long processing time for drying and gelation are bypassed), flammable solvents are not needed, they can be processed in a molten state and their solutions are stable in time. In addition, like the PDCs route, the sol-gel method is able to manufacture fibres, coatings, and aerogels by using liquid forming machinery.

1.3.3.1. Sol-gel route

In the 1970s and early 1980s, the sol-gel technique received considerable attention, as researchers aspired to explore new, low-temperature methods for producing common ceramics. The sol-gel approach helped to bypass the difficulties encountered in traditional processing techniques such as volatilisation, high temperature (above 2500 °C), or crystallisation. Hydrolysis and polycondensation are the two steps involved in the sol-gel process. The first step consists in mixing inorganic metal salts or metal alkoxide compounds with a mutual solvent (most often alcoholic) followed by low-temperature hydrolysis and

subsequent condensation. The resulting gels or sols undergo drying and pyrolysis processes that lead to the formation of nanometric size oxides [AB11] [RA95]. The oxides go through carboreduction – the small synthesised oxides size and their high reactivity mean that the carboreduction temperatures are lower than those used in conventional methods.

SiC can be synthesised *via* the sol-gel process from silicon precursors such as tetraethoxysilane (TEOS) ($C_8H_{20}O_4Si$), methyltriethoxysilane (MTES) ($C_7H_{18}O_3Si$), or a mixture of TEOS and MTES while for carbon sources phenolic resin, methylcellulose, or polyacrylonitrile (PAN) can be utilised [OM15] [LI00]. The sol is maintained at 40 °C for gelling, aging, and drying after the hydrolysis process. Moreover, the gel is submitted to heat treatment so as carbothermal reduction would synthesise silicon carbide. The sol-gel route presents with the advantage of synthesising submicron size carbides (d < 200 nm) at low temperatures (T < 1600 °C). Nevertheless, to reach a maximum reaction yield, high-temperature post treatments are often indispensable.

1.3.3.2. The polymer derived ceramic (PDC) route

The fabrication of non-oxide ceramics from molecular precursors was mentioned in the early 1960s by Ainger *et al.* and Chantrell *et al.* [AI60] [CH65]. A decade after, Veebeek *et al*. reported the polymer to ceramic transformation of polysilazanes, polysiloxanes, and polycarbosilanes in order to manufacture small-diameter Si_3N_4/SiC ceramic fibres for high-temperature applications [VE74] [VER74] [WI74]. Around the same time both Fritz *et al.*, and Yajima *et al.* achieved the synthesis of SiC ceramic materials by thermolysis of polycarbosilanes [FR56] [YA78] [YA75]. This was a breakthrough as it gave rise to PDCs. The birth of the PDCs route to manufacture new materials and components has come with various advantages over the powder synthesis of ceramics. Some of the major advantages are: 1) the possibility to modify the molecular structure of the precursors by a variety of chemical reactions; 2) the application of shaping technologies from well-known conventional polymer-forming techniques such as polymer infiltration pyrolysis (PIP), injection molding; 3) an easy machining of formed green body; 4) a relatively low synthesis temperature ranging from 1100 °C to 1300 °C which present an economical interest; 5) the possibility of reaching ternary and multinary ceramics containing the elements SiCN and SiCO; 6) achievement of high purity ceramics with an outstanding homogeneity at rather low temperatures varying from 1000 °C to 1400 °C [AL98] [CO10] [IO12]. Through the PDCs' pathway, several preceramic polymers with silicon atoms were initially studied. These polymers have a general structure as presented in Figure 1.2, which consists of a group or element X, and of substitutes, R^1 and R^2 linked to the silicon atom.

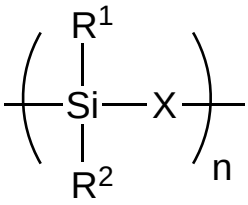

Figure 1.2. Simplified chemical structure of silicon-containing preceramic polymers [CO10].

It is possible to modify at the molecular level the group X of the polymer backbone, or the substituents R^1 and R^2 attached to silicon [CO10]. Changing the group X will result in numerous families of silicon organometallic polymers as shown in Figure 1.3. For instance, polycarbosilanes with X=CH_2, polysiloxanes with X=O, polysilazanes with X=NH and polysilylcarbodiimides with X=[N=C=N]. In parallel, adjustment and modification in terms of chemical and thermal stability, the solubility of preceramic polymers, as well as their electronic, optical, and rheological properties, can be achieved by changing the functional groups R^1 and R^2 attached to the silicon atoms.

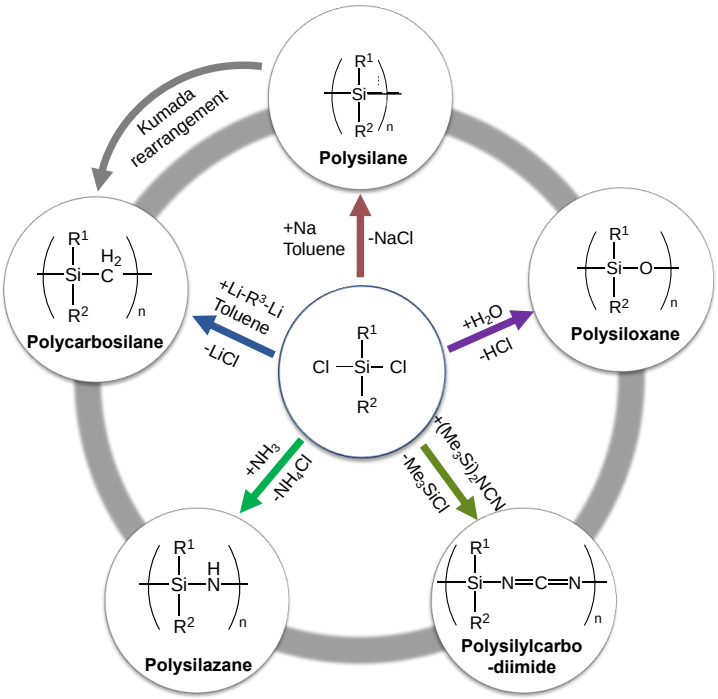

Figure 1.3. Schematic representation of typical preceramic polymers in the Si-C-N-O system (e.g., R^1 = R^2 = H, CH_3, $CH{=}CH_2$, etc.).

Polycarbosilanes (PCS) are polymers of interest in this study as we focus on developing silicon carbide, which can be obtained from a polymer having elements such as Si, C, and H. PCS has been described as an organosilicon polymer whose backbone consisted of silicon-carbon bonds [IN00]. It has a significant technological importance attributed to its high thermal, chemical, and oxidative environment. Therefore, it is not difficult to predict a large variety of applications that could be suited for these polymers in areas such

as (1) nanotechnology, (2) new ceramic materials organic-inorganic hybrids, (3) surface science, or even catalysis [MA15]. Moreover, being well known as ceramic material precursors, polycarbosilanes have been used in the production of silicon carbide, monoliths, fibres, composites, or refractory materials [GU14]. To synthesise polycarbosilanes, it is possible, to begin with suitable monomers such as carbosilanes. After polymerisation, the polycarbosilanes obtained can under heat treatment, generate an amorphous ceramic that, for temperatures above 1000 °C leads to a crystalline ceramic. Greil *et al*. have summarised these four steps (synthesis, crosslinking/shaping, pyrolysis, and crystallisation) as shown in Figure 1.4 [GE00].

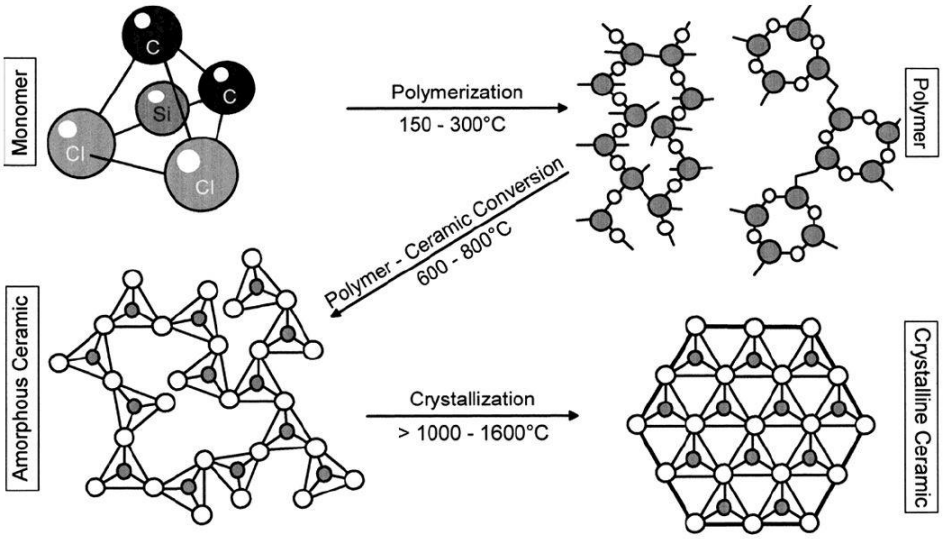

Figure 1.4. Scheme of molecular and microstructural transitions during ceramic manufacturing from preceramic polymers [GE00].

During the heat treatments, the polymer undergoes structural rearrangements accompanied by mass losses and the ceramic yield obtained can be calculated as follows:

$$\eta_{ceramic} = \frac{m_{ceramic\ obtained}}{m_{polymer\ pyrolysis}} \times 100. \qquad \text{Eq. (1.4)}$$

Ceramic yield can be defined as the mass of ceramic expressed as a percentage of the mass of the ceramic precursor used in the crystallisation process. The attributes of the preceramic polymer strongly impact its ceramic yield, which must be as high as possible in order to limit, the quantity of the material used in the fabrication of ceramics. As mentioned before, the physical and chemical properties of PDCs can be altered significantly by modifying the polymer precursors [MI89]. Therefore, the synthesis of polycarbosilanes is a crucial step in obtaining PDCs and their composites.

1.4. Synthesis of polycarbosilanes *via* different reaction routes

PCSs of the general structure (-R^1R^2Si-CR^3R^4-]$_n$-(R^1, R^2, R^3, R^4 being organic groups or H) have been synthesised by a variety of reaction pathways. The Kumada rearrangement of poly(dimethylsilane), Grignard polycondensation reactions of chlorosilanes, ring-opening polymerisation of 1,3-disilacyclobutanes catalysed by Pt-containing complexes, and hydrosilylation of vinylhydridosilanes are among the new routes that have been considered to synthesise polycarbosilanes [GR00] [ME15].

The most pivotal and strongly explored access to PCSs certainly is the Yajima process [YA75]. It gained much attention as it could thermally convert insoluble and not meltable poly(dimethylsilane) (PDMS) into soluble and processable poly[(methylsilylene(methylene)] as shown in Figure 1.5 [SO13] [YR78]. The essential step in the Yajima process is a rearrangement of the polymer backbone involving methyl groups, and occurring at around 400 °C. This reaction is also known as the Kumada rearrangement or Kumada reaction [CH08]. The process is radically induced when methylene migrated from one of the silicon bonded methyl groups attached to the polymer backbone, into the polymer chain. During the initiation steps, silyl radicals are formed when the Si-Si bonds are cleaved by heating, followed by the migration of the H-radical from the methyl group to the silyl radical. In the Kumada rearrangement step, the generated methylene radical is inserted into a Si-Si bond through which a new silyl radical is generated. The propagation steps are carried forward by a repeated H-radical migration to the silicon radical resulting in the methylene radical. The last step (termination step) takes place when the radical is recombined [BO92] [LO15].

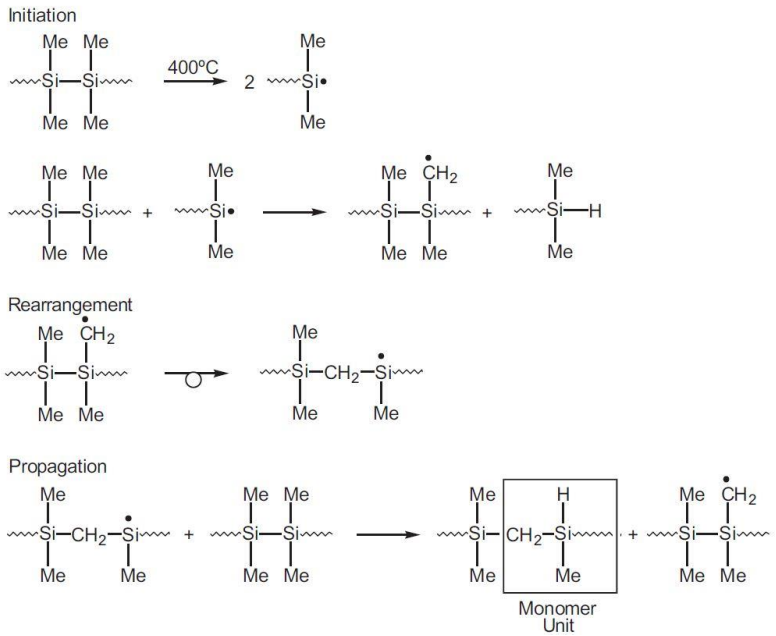

Figure 1.5. Key steps in the Kumada rearrangement of poly (dimethylsilane) [SO13].

Kim *et al*. pointed that this method generates several serious operational problems such as the release of gaseous by-products such as CH_4, Me_3SiH, SiH_4, etc. [KI05]. Hence, the polymerisation must be carried out in a pressure resistant equipment to be able to withstand the pressure for a period as long as 10 to 15 hours. Moreover, provision for potential fire hazards is necessary. Subsequently, Yajima *et al.* made use of catalysts to synthesise polycarbosilanes at normal pressure by adding small amounts of polyborodimethylsiloxane to PDMS. Another concern was the importance of removing low molecular weight compounds from the polycarbosilane before the shaping process. This was done to avoid the brittleness, the poor tensile properties, or the breakage of these fibres that might occur in the final step. This process of producing silicon carbide by pyrolysis of polycarbosilanes resulted in silicon carbide with an excess of carbon, low yields as well as unwanted impurities as SiO_2. It was announced that the highest ceramic yield based on thermogravimetric analysis was 60 % [SM86] [SO13].

Interrante *et al.* have developed hyperbranched polycarbosilanes namely hydridopolycarbosilanes (HPCS) to overcome the presence of an excess of carbon in the final material of PCS and to increase the ceramic yield [IN02]. Unlike alternatives in existing SiC precursors, this polymer retained its initial 1:1 stoichiometry after pyrolysis, with H_2 as the main volatile product. It is an oily liquid, which is soluble in common solvents like ether or hexane [IN97] [SR10]. This precursor HPCS has a rather low molecular weight (M_n = 600-1000 $g \cdot mol^{-1}$), with a hyperbranched structure of $[H_3SiCH_2–]_x[–SiH_2CH_2–]_y[–SiH(CH_2–)_{1.5}]_z[–Si(CH_2–)_2]_l$. An overall composition of $[SiCH_4]$ was obtained by Grignard coupling of chloromethyltrichlorosilane leading to poly(dichlorosilylenemethylene). Chlorine atoms are substituted by hydrogen atoms by the treatment of the as-obtained poly(dichlorosilylenemethylene) with $LiAlH_4$. Consequently, branched PCS with an idealised structure $[-H_2Si\text{-}CH_2-]_n$ were generated as shown in Figure 1.6 [KA16] [SO13].

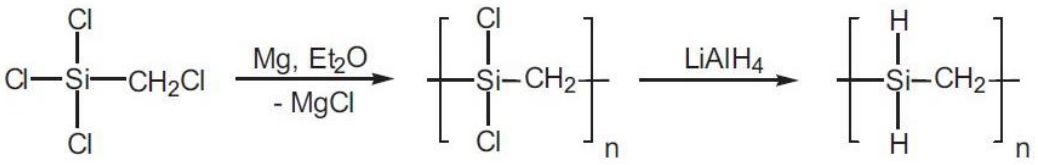

Figure 1.6. Synthèse du HPCS [SO13].

Improvement in the synthesis route has been conducted by carrying structural modification to increase the purity and the yield of the product. Prior to the reduction with $LiAlH_4$, the substitution of some chlorine atoms with a small amount (10%) of allyl groups yielded a polymer with improved ceramic yields. This produced allylhydridopolycarbosilane (AHPCS) which is commercially available under the name SMP-10 by Starfire System, Inc. It

is a translucent yellow soluble liquid with a chemical structure represented in Figure 1.7. AHPCS was found to undergo pyrolysis with a ceramic yield of approximately 70-80 % [KA16] [SO13]. However, the Grignard reaction times was considered too long to obtain a polymer with higher yields.

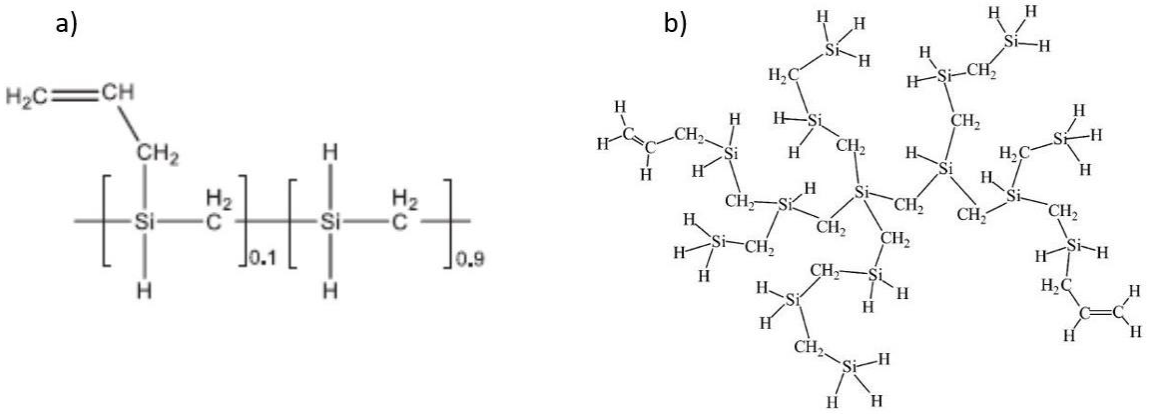

Figure 1.7. a) Chemical structure of AHPCS [SR10] b) AHPCS “average” structure, as derived from NMR and GPC studies [IN02].

In the search for high yield ceramics, linear polycarbosilanes are usually disregarded as upon heat treatment above 1000 °C, there is a significant loss of Si and C, which often results in a low ceramic yield. This is normally due to polycarbosilanes consisting of inert groups such as methyl as the substituents on Si or simply as a consequence of low molecular weight polymers. Wu and Interrante reported a new route to generate linear polymer, which would provide a higher molecular weight polycarbosilane with improved physical properties and ceramic yields [WU02]. To achieve this amelioration, the polycarbosilane polymer utilised in the pyrolysis is a polysilaethylene obtained by polymerising 1,3-disilacyclobutane with a ring opening polymerisation using Pt-group metal complexes such as chloroplatinic acid as catalyst (Figure 1.8). By beginning with an inexpensive, commercially available compound, methyltrichorosilane, (Cl_3Si-CH_3) the authors established a revised multistep poly(silaethylene) synthesis. Chloromethyltrichlorosilane Cl_3Si-CH_2Cl was produced *via* halogenation using chlorine in the presence of ultraviolet light. Nevertheless, it could not be directly altered into 1,1,3,3-tetrachloro-1,3-disilacyclobutane. Hence before the reduction coupling, two of the silicon-bonded chlorine atoms were replaced by ethoxy (R = OEt) achieved by an alcoholysis reaction. The ethoxy groups in 1,1,3,3-tetraethoxy-1, 3-disilacyclobutane were subsequently substituted with chlorine atoms by a treatment with acetyl chloride together with $FeCl_3$. Pt-catalysed ring opening polymerisation occurred prior to the reduction with $LiAlH_4$ [SM86] [SO13] [WU92]. Consequently, by starting with 1,3-disilacyclobutane as a monomer, ROP generated a linear polymer with 85 % ceramic yield [WU89].

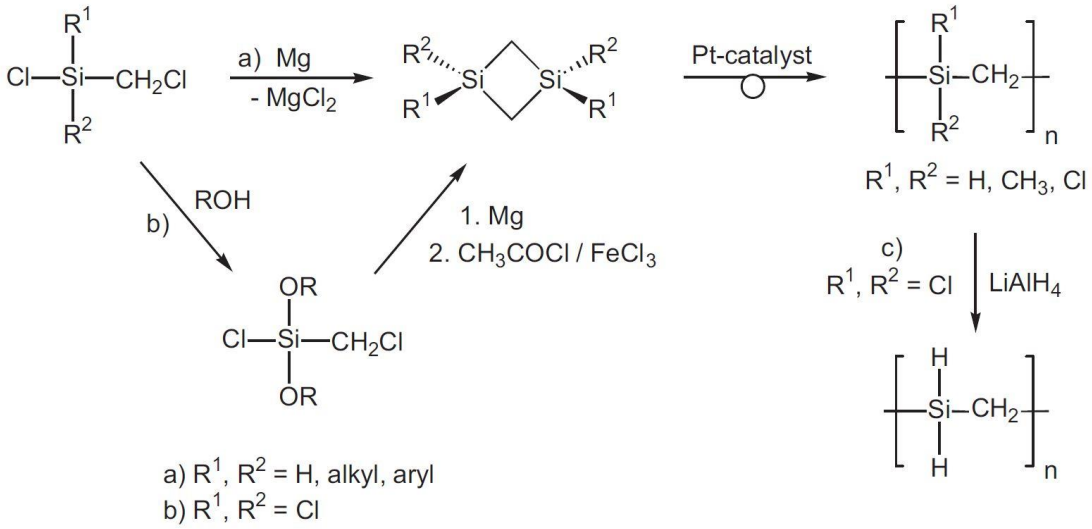

Figure 1.8. Synthesis of PCSs by Pt-catalysed ring opening polymerisation (ROP) of 1,3 disilacyclobutane derivatives [SO13].

Moreover, another way to synthesise PCS is through hydrosilylation reactions that are widely implemented to produce functional silanes and siloxanes. A hydrosilylation reaction consists in the addition of a silicon-hydrogen bond across an unsaturated bond by the catalysis of transition metal complexes forming both valid hydrogen-carbon and silicon-carbon bonds [HA07] [MA08]. There are different catalysts that can be used for the hydrosilylation reaction; the most common one is the Karstedt's catalysts (Figure 1.9). Lately, a lot of efforts have been directed towards the development of new catalysts due to the scarcity and high price of platinum. Therefore, research for alternative platinum-free catalysts with low-cost transition metals is being conducted. For the time being, industries and researchers still prefer the use of platinum-based catalysts since their catalytic activity is unparalleled [MEI16]. Hydrosilylation reactions catalysed by platinum catalysts commonly follow Chalk-Harrod and modified Chalk-Harrod mechanisms.

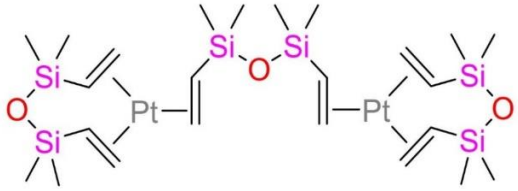

Figure 1.9. Chemical formula of the Kastedt's catalyst [HO17].

The mechanism as shown in Figure 1.10 consists of four elemental steps: the oxidative addition of silanes on the platinum metal leading to have an oxidation state of (+II). The second stage of the mechanism is the coordination of ethylene to the metal. The third step consists of either the Chalk Harrod mechanism route or the modified Chalk Harrod pathway where there is an insertion of the Pt-H bond into the olefin (Figure 1.10). In the end, the

mechanism will undergo a reductive elimination of the hydrosilylation product. The catalytic cycle is concluded with the regeneration of the metal with an oxidation state zero, which is found available for a new oxidative addition step [CH65].

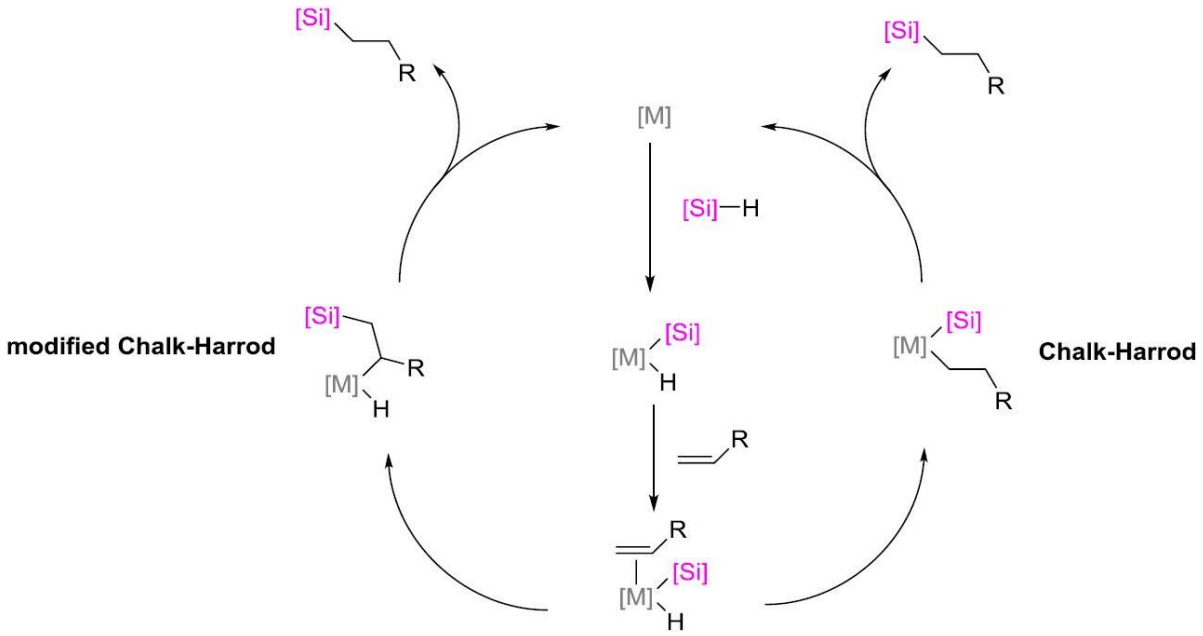

Figure 1.10. Chalk-Harrod mechanism and Chalk Harrod modify mechanism [HO17].

The advantages of this route are: i) the synthesis from adapted monomers instead of using commercially available polymer, thus controlling the composition of the material from the start. ii) the reaction can take place in one step. iii) the reaction is usually rapid since no need for purification step. To have an insight during the polymerisation, suitable characterisation techniques need to be selected. This will help to better control the polymerisation reaction to obtain a final ceramic product with desired properties. The synthesis of polycarbosilanes forms part of the first step in the different stages of PDC route. The other stages of the PDC route are as essential as the chemical synthesis of polymer from molecular precursors. Therefore, the description of the different stages of the PDC route is thereafter reported with a particular emphasis on shaping/crosslinking, pyrolysis, and crystallisation.

1.5. Different stages of PDC route

The structures of generated ceramics obtained after thermal decomposition are greatly influenced by the chemistry and architecture of the precursors, the synthesis route, and conditions (inert or reactive atmosphere, heating rate, imposed time) under which heat treatment took place. During the polymer to ceramic transformation, the preceramic polymer experiences several processes as a function of temperature. After the synthesis of the

polymeric precursors, the polymer can be crosslinked/shaped into a desired green body. Under heat treatment, an amorphous ceramic will be generated that, for temperatures above 1000 °C leads to a crystalline ceramic. Figure 1.11 illustrates the general four steps processes in the fabrication of ceramics from polymeric precursors. An overview on each step will be discussed.

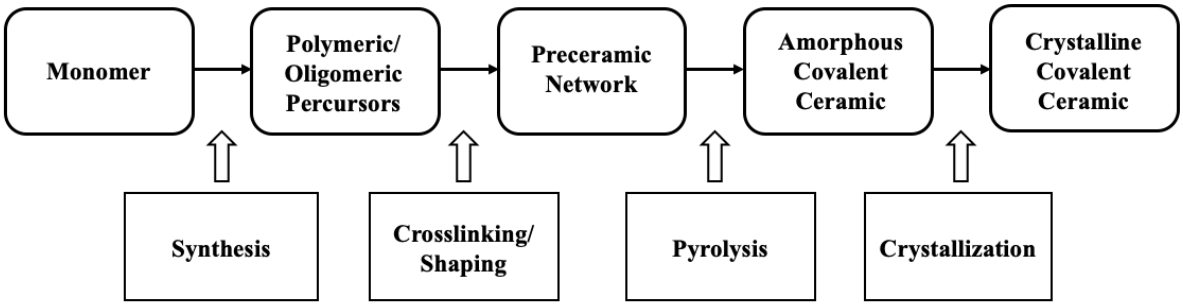

Figure 1.11. Description of different classic steps in the PDCs path.

1.5.1. Chemical synthesis of polymers from molecular precursors

The first step is the chemical synthesis of the polymer from molecular precursors. It consists of the polymerisation (thermal or chemical) of the starting monomer [CO10]. With the growing interest in materials of complex composition made of three or even four elements, this step allows for the chemical incorporation of metalloids/metals in the monomeric precursor [LI15]. In addition, this makes it possible to play on many physicochemical properties of the precursor (such as its viscosity, fusibility, solubility, glass transition temperature, or its physical state) in order to adjust it to the targeted shaping process, to improve its ceramic performance, as well as ensuring that its shaping is maintained during ceramic processing [CH92] [ME13] [MI07] [WA04] [WE00] [WE98] [ZI99].

1.5.2. Crosslinking

A particular characteristic of processing parts utilising preceramic polymers is that after shaping, the components need to be altered into a thermoset material capable of maintaining its shape during ceramisation. The integration of suitable functional groups facilitates the formation of a thermoset material *via* condensation or addition that happen spontaneously, ordinary below 200 °C for thermal crosslinking. The utilisation of catalysts can reduce the crosslinking temperature as well as preventing the evaporation of oligomers with formation of bubbles and increase the ceramic yield [HA04], [IS15]. The addition of a catalyst often enables for the crosslinking reactions to occur during shaping and not after the pyrolysis treatment.

Curing can also be accomplished after shaping as well by oxidative treatments. However, a decrease of its high temperature stability is noted due to a considerable oxygen

contamination in the ceramic generated [OK06] [TA87] [HQ01]. E-beam curing is a solution to obtain oxygen-free ceramics, however the penetration depth restricts the usage of this method to obtain components such as fibres [NA99] [ID04] [ID01]. Otherwise grafting photo-sensitive functional groups onto the backbone of the preceramic polymer can facilitate UV-Curing, mostly for micro-component [LI02] [PH07] [SC04]. It should be mentioned that the degree of crosslinking greatly influences the rheological behaviour of preceramic polymers and has to be controlled accordingly. This crosslinking step is therefore very important for the production of flawless ceramics [BE05] [CH91] [ME15] [MU04] [WE01].

1.5.3. Shaping

Preceramic polymers are still polymeric in nature at the temperature at which shaping processes are performed. Consequently, they are subjected to numerous shaping processes, with some having distinct approaches or can be operated with more ease than in the case of ceramic powders. Various shaping techniques are being used in processing of PDCs such as deposition or impregnation, tape casting, additive manufacturing or pressing (Figure 1.12) [DU07] [CO10]. Warm pressing, fibre drawing, extrusion and injection moulding are plastic forming technologies that can be employed to shape preceramic polymers due to the flexibility that the PDC route provides. For any shaping methods implemented, understanding the rheology of the system is essential to shape the material in any desired forms.

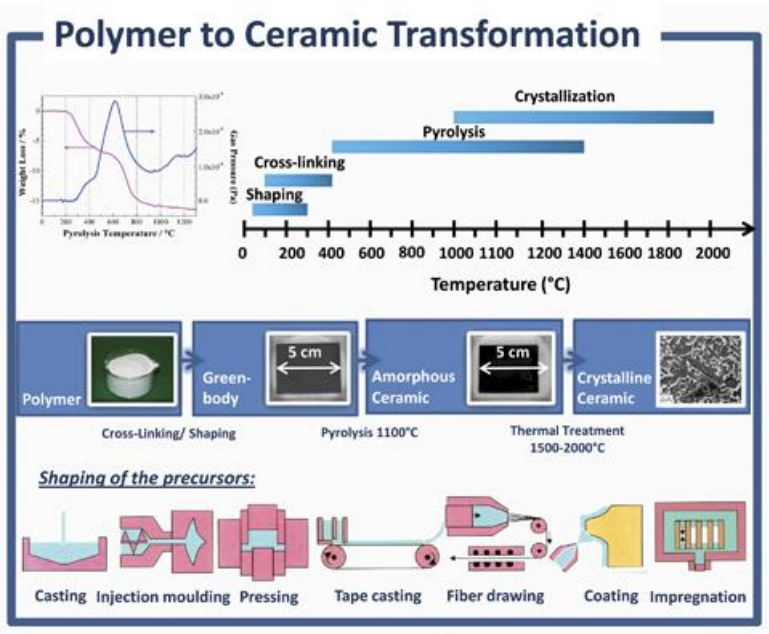

Figure 1.12. Different shaping processes [CO10].

1.5.4. Pyrolysis

The third stage essentially concerns the physical and chemical transformation of the polymer network into an amorphous ceramic. This conversion is carried out by heat treatment of around 1000 °C, of which the experimental conditions (e.g., temperature ramps, nature of the atmosphere gas in the chamber, etc.) directly influence the ceramic conversion efficiency and the composition of the latter. For example, the use of ammonia can significantly reduce its carbon content and develop nitrides. During this conversion between 10 % and 50 % of the initial mass of the polymer is expelled in various gaseous forms while the density of the material increases [RI96]. These gases are produced by the reactions that take place during heat treatments between the organic groups contained in the polymer or by decomposition of the latter into small fragments or even oligomers, at the start of the conversion. Regarding its microstructure, the material is an amorphous solid exhibiting a homogeneous distribution of its different elements [TR02].

1.5.5. Crystallisation

The final stage is the crystallisation of the amorphous ceramics through a second heat treatment above 1000 °C and under a controlled atmosphere. The crystalline phases for polycarbosilanes are often β-SiC and $C_{Graphite}$ since crystallisation occurs between 1100 and 1500 °C. This crystallisation is obtained by the segregation of the different phases contained in the ceramic (redistribution of chemical bonds) with increasing temperature [MU00]. These amorphous segregations then crystallise locally: this is the nucleation step. Nanocrystals are first contained in an amorphous matrix then, their growth by diffusion leads to nanocomposites fully crystallised [BI95]. This is accompanied by a volume shrinkage resulting from the densification. The thermal stability of these ceramics depends on their composition; for SiCN ceramics, it is mainly limited by the presence of silicon nitride. Indeed, Si_3N_4 reacts in solid phase with free carbon (carboreduction reaction) from 1484 °C and it decomposes at 1876 °C. Si-N bonds are broken and free carbon is consumed, forming crystallites of SiC and causing the release of N_2. This induces a mass loss, the formation of porosities and considerably modifies the composition of the ceramic. To conclude on this transformation of the polymeric precursor into ceramic, it is useful to specify that the pyrolysis /crystallisation atmosphere will impact the temperature and the occurrence of crystallisation of the various phases, as well as the temperature of the decomposition reactions.

The different steps used in the PDC route to transform the organic/organometallic material into ceramics have been presented. Among them, shaping is of particular interest since it can generate complex-shaped ceramics. Nevertheless, few information is available on the relationship between the rheological behaviour of preceramic polymers and shaping

processes. Consequently, studies that have put in evidence the rheological behaviour of preceramic polymers and their influence on the shaping processes are reported.

1.6. Rheological behaviour of preceramic polymers

Rheological analysis of polymeric materials presents two major aims. Firstly, it is employed to facilitate the shaping processes of polymers. Secondly, it provides rheological insights of the molecular structure of the polymer. Rheological investigation can contribute in tailoring the polymer materials for different applications. The rheological properties of polymers are closely linked to their molecular structure. The molecular structures are normally characterised by the number and weight average molar mass (M_n, M_w) and molar-mass dispersity (M_w/M_n). Since polymers are viscoelastic materials, they can be characterised by the use of a rheometer. Moreover, temperature, atmosphere and geometry of the flow device are parameters that affect the polymer processing since they have a direct influence on the rheological behaviour of the polymer. Choosing to modify the chemical structure of the polymer, to improve the properties of the final ceramics, will imply to study the effect of the structural changes on the viscoelastic behaviour of the polymer. There are many different processing techniques to shape polymers - for example extrusion, injection moulding, compression moulding, reaction injection moulding, or fibre spinning [CO10]. Since during the fabrication process the polymer flows through a shaping device, normally a die or a mould, it is primordial to study its rheological properties. Depending on the application and fabrication techniques to be used, the understanding and the control of the rheological behaviour of the polymer will help in optimising the processing conditions. To apply this approach to the PDCs' field, parameters influencing the rheological behaviour of polycarbosilanes will be presented first followed by two shaping processes: Fibre drawing and Direct Ink Writing (DIW).

1.6.1. Parameters influencing the rheological behaviour of polycarbosilanes

Rheology plays an important role in characterising organosilicon polymers such as polycarbosilanes, polysiloxanes, polysilazanes, polysilycarbodiimide or polysilsesquioxanes. The different preceramic polymers mentioned have all different backbone structures. The properties (mechanical behaviour, thermal resistance, corrosion resistance) of the final ceramic would depend on the starting composition of the preceramic composition. Viscosity has a direct influence on the shaping process since it depends on the macromolecular structures and on the extent of reaction during the synthesis of the polymers. By starting with tailored preceramic structures and by making use of a rheometer to control the rheological properties at various stages of the ceramic processing, ceramics with numerous shaping

variants could be obtained. Moreover, external parameters such as temperature, atmosphere, catalyst or fillers (Figure 1.13) can influence the rheological behaviour of the preceramic polymers. They directly influenced the polymerisation/crosslinking processes to modulate the rheological behaviour sought to improve the shaping ability. Figure 1.13 summarise fundamental studies found in the literature review of rheology of preceramic polymers. As SiC preceramic precursors are polymers of great interest, studies on polycarbosilanes were reported [GU10] [GU14] [WA20]. In addition, the following paragraphs will present two papers that deal with a linear polymer (PCS, Al-O-Si bonded with PCS and Al-Si bonded with PCS) and a hyperbranched polymer (Liquid hyperbranched polycarbosilane - LHBPCS).

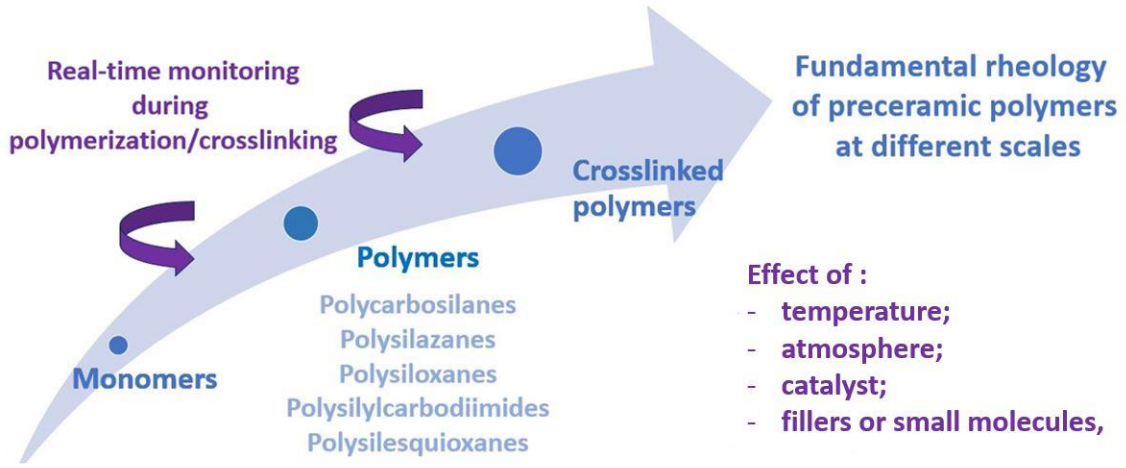

Figure 1.13. Summary of the essence of the fundamental study of rheology of preceramic polymer.

1.6.1.1. Effect of time, temperature and atmosphere

Polycarbosilanes (PCS) and hetero-metal substituted PCS (M-PCS) are ceramic precursors used for the preparation of silicon carbide fibres obtained by melt spinning processes, monoliths, composites, and refractory materials for high temperature applications [CH06] [CH08] [SH04] [YA78]. To better understand the processing of PCS melts, a fundamental study on their rheological behaviour was needed. Therefore, Gupta *et al.* carried out a study on the rheological behaviour of PCS with respect to time, temperature, and atmosphere [GU10]. PCSs with different softening points were synthesised *via* the thermal backbone rearrangement of a polydimethylsilane (PDMS) $[Si(CH_3)_2CH_2SiH(CH_3)CH_2]_n$. The melt viscosity variation and thermosetting behaviours were studied under different parameters such as atmosphere (inert and air), temperature, time evolution and shear rate. This investigation was carried out using synthesised PCS samples having different softening point ranging from 90 °C to 190 °C. The authors found out that in an argon atmosphere, the viscosity of all PCSs decreased with increasing temperature. However, under a constant temperature, the viscosity remained constant for low softening point samples, whereas for

high softening point samples the viscosity rose. Furthermore, it has been observed that all the PCSs crosslinked rapidly in air as compared to when exposed to an inert atmosphere of argon. Irrespective of the atmosphere, the high molecular weight PCS (6,259 $g \cdot mol^{-1}$) like PCS-190 (softening point at 190 °C) thermoset faster due to higher number of susceptible available sites enhancing the crosslinking effect as compared to a lower molecular weight PCS (6,144 $g \cdot mol^{-1}$) like PCS-90. The authors hypothesised that lower molecular weight PCS acted as a plasticizer under air atmosphere. PCS conveyed a thermosetting nature due to Si-H groups reacting with oxygen forming Si-OH and Si-O-Si linkages. In lower shear region, the material showed a shear thinning behaviour (viscosity of fluid decreases whenever the shear rate increases) and in the intermediate range of shear rates, the viscosity remained constant. The authors concluded that, to avoid undesired crosslinking during the processing of the PCS, it is important to have a sample with a high molar-mass dispersity and to sustain an inert atmosphere.

1.6.1.2. Effect of heterometal content and nature of bonding with polycarbosilane

To enhance the possibility of applications of these ceramics, the inclusion of a heterometal into PCS was often performed. The rheological impact of a heterometal on PCS was not reported until recently by Gupta *et al*. [GU14]. This study consisted in exploring the rheological behaviour of alumino-polycarbosilane (Al-PCS) having either Al bonded directly or through oxygen bond to the silicon (Figure 1.14) in different quantities, with respect to time, temperature, and atmosphere (inert and air). Hence, a comparison between Al-O-Si bonded with PCS (AlOR-PCS) and Al-Si directly bonded with PCS derivatives (Alac-PCS) prepared using aluminium acetylacetonate (Alac), was conducted to investigate their rheological behaviour.

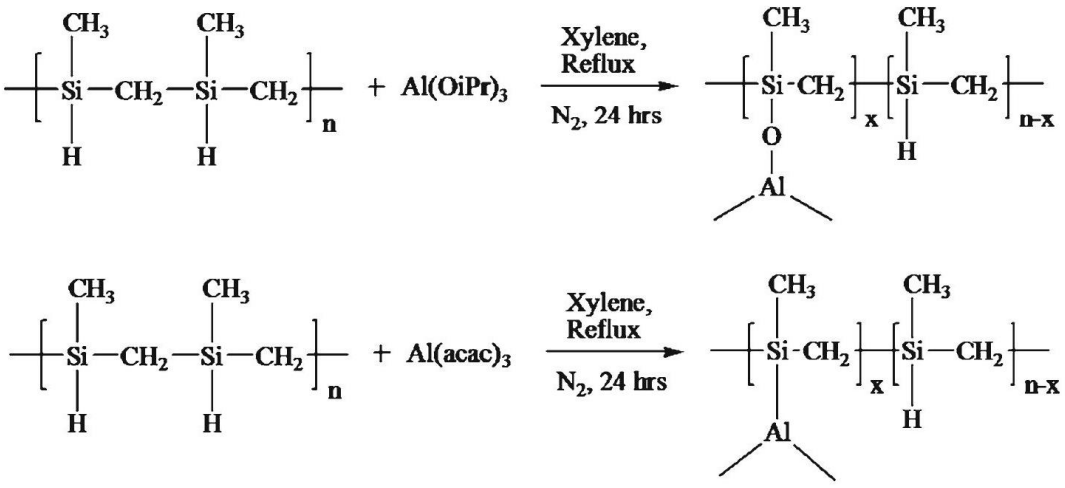

Figure 1.14. Reaction of $Al(acac)_3$ and $Al(OiPr)_3$ with PCS [GU14].

The authors found out that, the increase in viscosity was related to an increase in metal salt content, and that it was more noticeable in Alac-PCS than in AlOR-PCS. This might be due to the higher reactivity of the acetylacetonate ligands in Alac-PCS with Si-H groups of PCS. Under inert atmosphere, the melt viscosity could be maintained for a longer period for both Alac-PCS and AlOR-PCS as compared to an air atmosphere. Since Alac-PCSs had a higher degree of crosslinking than AlOR-PCSs in any atmosphere, AlOR-PCS was more suitable for fibre spinning (as processing takes longer). In both studies carried out by Gupta *et al.* an (Fourier transform infrared spectroscopy) an FTIR spectrometer was used to monitor the fingerprint of chemical groups present at the beginning of the reaction and the eventual changes occurred during the reaction. This allowed the authors to make the correlation between the changes in chemistry using data obtained from FTIR spectroscopy and the rheological measurements. However, the rheological and FTIR measurements were carried out in an *ex-situ* setup, which might bring experimental inconsistency as compared to an experiment carried out with an *in-situ* experimental setup.

1.6.1.3. Effect of structure of the polycarbosilane

Concerning hyperbranched polymers, Wang *et al.* obtained SiC foams that were prepared based on a precursor conversion method. A liquid hyperbranched polycarbosilane (LHBPCS) $[SiH_{1.9}(CH_2CH{=}CH_2)_{0.1}CH_2]_n$ was used as the preceramic polymer together with expandable microspheres (EMS) as pore foaming agents [WA20]. The optimisation of the crosslinking reaction rate of LHBPCS was carried out by regulating the content of free radical initiator *tert*-butyl peroxybenzoate (TBPB) as well as temperature. The forming rate of EMS was synchronised with the thermal crosslinking behaviour of the mixture of LHBPCS with varying contents of free-radical initiator TBPB at 120 °C by using rheology tests. The rheological measurements helped in monitoring the evolution of the crosslinking process by analysing the evolution of the **complex viscosity** *(the measure of the total resistance to flow as a function of angular frequency)*, **storage modulus** (G': the energy stored in the elastic structure of a sample) and **loss modulus** (G'': the viscous part or amount of energy dissipated in the sample) of the two samples namely LHBPCS with 0.2 wt. % TBPB and LHBPCS with 0.5 wt. % TBPB.

At the beginning, LHBPCS with different TBPB contents demonstrated a low complex viscosity of about 0.02 Pa·s. as shown in Figure 1.15a. However, the complex viscosity increased drastically with time indicating the formation of the network structure of LHBPCS during chemical cross-linking.

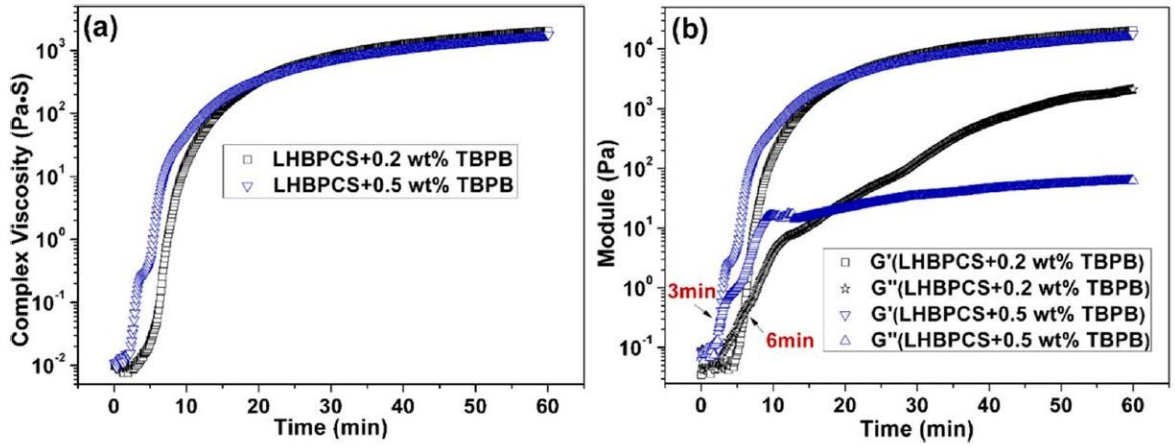

Figure 1.15. (a) Evolution of complex viscosity of LHBPCS vs time after adding different contents of TBPB at 120 °C; (b) Evolution of storage modulus (G') and loss modulus (G'') of LHBPCS vs time after adding different contents of TBPB at 120 °C [WA20].

At the end of the test, LHBPCS was converted from a liquid to a solid. LHBPCS with 0.5 wt. % and 0.2 % TBPB reported a gelation time (the point at which $G' > G''$) of 3 and 6 min at 120 °C, respectively (Figure 1.15b). The faster crosslinking reaction was recorded in LHBPCS with 0.5 wt. % TBPB due to the presence of the higher amount of TBPB. LHBPCS having 0.2 wt. % of TBPB had a gelation time that corresponded to the foaming time of EMS. Hence, different amounts of EMS were incorporated into the LHBPCS having 0.2 wt. % TBPB for subsequent foaming and pyrolysis. Porous SiC with porosities of 87.4 - 91.2 % with pore sizes of 20 - 30 µm was obtained when the mass ratio of EMS to LHBPCS was increased from 60 wt. % to 120 wt. %. Moreover, SiC foam with low thermal conductivity was achieved, due to its small size pore, low density, and amorphous structure. The resulted foam manufactured by this method could be a promising high-temperature thermal insulation material candidate since it combined high thermal stability together with good thermal insulation properties.

Temperature, atmosphere, time, heterometal such as aluminium and the nature of the bonding of Si to polycarbosilanes are among some parameters that affect the rheological behaviour of polycarbosilanes. By understanding their influence on the rheology of polycarbosilanes, a satisfactory ceramic material, in terms of ceramic yield, shaping and thermal behaviour can be obtained. Moreover, as discussed, hyperbranched PCS can be employed to manufacture SiC foam with good physical and chemical properties. In this way, PCS can be utilised for other applications such as fibre forming or inks.

1.7. Shaping process

Among the numerous shaping techniques used in PDC processing: fibre drawing and DIW are the ones that have been considered. These two techniques were selected since they constitute among the most published work in the PDC field.

1.7.1. Fibres drawing

In 1970s, precursor-derived ceramic fibres having Si/C/N(O) elements in their structure were put forward by Yajima and Verbeck [VER74]. As a result of which several fibrous systems have been developed consisting mostly of Si-based (e.g. Si/C/N) or B-based (e.g. BN) ceramics fibres. The production of fibres consists of four major steps: i) the synthesis of a designated precursor comprising of constitutive elements of the desired ceramics; ii) the conversion of the precursor into a preceramic network with the desired rheological behaviour to ensure good processing capabilities; iii) the achievement of green fibres through the spinning of preceramic polymer; iv) a thermal treatment under oxygen free atmospheres to obtain intended ceramic fibres. Furthermore, to achieve acceptable PDCs fibres, it is essential to control the spinning and the pyrolysis processes. However, spinning of preceramic polymers is possible with materials possessing suitable viscoelastic properties. Melt spinning polymers need to express a shear thinning behaviour during extrusion. It is also pivotal that the polymer flows without necking from the spinneret hence avoiding deformation instabilities. To understand the key parameters influencing the flow behaviour of preceramic polymers during the fibre spinning process, studies about the rheological behaviour of fibre have been reported. Studies carried out on silicon and boron-based ceramic materials will be presented.

1.7.1.1. Silicon-based material ceramics

Si-based preceramic polymer is normally required to be tractable, thereby presenting a broad range of viscoelastic properties that render it potential for shaping processes. Normally, this can be accomplished by tailoring their chemical composition as well as their molecular structure. However, the difficulties lie in controlling the numerous requirements to process preceramic polymers. This can be observed in melt spinning equipment in which stretching deformation prevailed the shaping processes. In this way, Ouyang *et al.* conducted an experimental and numerical modelling of fibre spinning flows of a preceramic polymer melt [OU10]. The authors set up a procedure, which could measure the fibre diameter in real time during the fibre spinning process. The study used a polycarbomethysilane sample (PCMS). To determine the temperature influence on the samples and the repeatability of the measurements, the sample was exposed to a frequency sweep test carried out in the linear viscoelastic regime with four distinct temperatures namely 110 °C, 115 °C, 120 °C and 125 °C. The rheological results indicated that low molecular weight PCS showed a constant

viscosity along the whole frequency range. Moreover, the loss modulus was constantly higher than the storage modulus by one order of magnitude proving the liquid-like component of the material dominated the elastic part. A gel-like structure was observed at higher frequency when temperature of the samples increased. Two groups of PCS samples were spun under different spinning conditions. The first one was spun with varying temperature while keeping the take-up velocity constant, and the second experiment consisted in varying the take-up velocity with constant spinning temperature. In both cases the flow rate (Q) and piston velocity (V_p) were kept constant. The first group of PCMS with a chemical formula of $(C_2H_6Si)_n$ [purchased from Aldrich Co] consisted of PCS samples named S1-A, S1-B, S1-C that were spun at temperatures of 117 °C, 120 °C and 125 °C, respectively. Figure 1.16 displayed the evolution of fibre diameters during the spinning process along the spinline Z of the first group of PCMS samples.

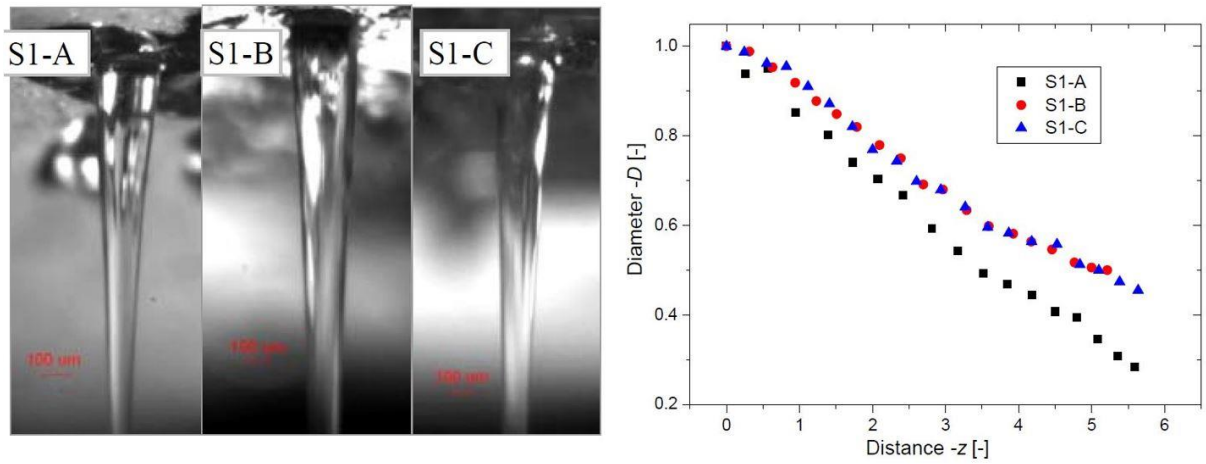

Figure 1.16. Pictures of PCS in fibre spinning process and their measured dimensionless fibre diameter *D*(z) along spinline z [OU10].

The authors observed that the evolution of the curve of fibre diameter S1-A, which was spun at a temperature of 117 °C, had the steepest slope compared to the S1-B (spun at 120 °C) and S1-C (spun at 125 °C). It was associated to its the higher viscosity obtained during the rheology test. However, since all samples had the similar take-up velocity, samples with higher viscosity experienced a higher resistance when an extensional force was applied. Thus, S1-A was more apt to keep their shape. At the same time, under stretch forces, samples having spinning temperature of 120 °C (S1-B) and 125 °C (S1-C) experienced no apparent change in the fibre diameter as a result of their approximately close viscosity values.

A second batch of samples having varying take-up velocities with constant spinning temperature and flow rate demonstrated that the diameter of the fibre decreased with increasing take-up velocities. The numerical computations together with the rheological

measurements allowed for a complete rheological characterisation of the samples. Both the shear properties and the extensional thinning viscosity (a fluid for which the extensional viscosity is decreasing with increasing strain rate) obtained during spinning process confirmed a satisfactory spinnability of the samples. However, it might have been better to match the shear rheology with the extensional rheology (extensional rheology focuses on pulling on a piece of material in a purely extensional manner *i.e.* no shear) to have general criteria of quantitative as well as qualitative appreciation of the fibre spinnability of PDCs.

1.7.1.2. Boron-based ceramic materials

In addition to SiC based material, some papers based on boron materials are presented due to their promising rheological findings on fibre forming. Hexagonal boron nitride (*h*-BN) is a non-oxide advanced ceramic which provides great capabilities as fibrous consolidating agents in targeted applications. *h*-BN had been presented with appealing properties such as high stiffness and toughness, a good non-wettability in contact with metallic and silicate melts, and an oxidative resistance up to 1000 °C. Furthermore, poorly dense ceramic showed promising potentialities in infrared and microwave-transparent structures as well as they offered outstanding electrical insulation properties due to inadequate dense ceramics.

Several studies have been carried out to investigate the rheological properties of boron-based ceramic materials required for fibre spinning process. Thus, a series of preceramic *B*-(methylamino)borazine-based polymers as fibre precursors have been designed by Duperrier *et al.* [DU07]. The authors carried out an investigation on the synthesis and spinning processes on a batch of *B*-(methylamino)borazine to inquire about the influence of the architecture, thermal and rheological behaviour upon melt spinning. It was noted that architectural changes had a greater impact on the thermal behaviour as well as on the melt spinnability of the polymer than on the chemical composition itself. The authors reported that a temperature between 160 °C and 185 °C was most suited for melt spinnable poly[*B*-(methylamino)borazine]. Two major troubleshooting that might occur during polymer melt extrusion were: 1) a wall depletion event inside the spinneret; 2) a thickening of extensional viscosity along the spinning line. As a result, shear and extension rheology tests were carried out to counteract these effects. In this way, Duperrier *et al.* investigated the most appropriate conditions for melt-spinning of poly[*B*-(methylamino)borazine] in terms of complex viscosity, storage modulus and loss modulus [DUS07]. With increasing oscillatory angular frequency, the complex viscosity decreased showing a shear thinning behaviour of the polymer melt during extrusion as shown in Figure 1.17. In addition, the dynamic moduli rose steadily with increasing oscillatory frequency. A cross-over point was marked at ω = 90 s^{-1}, indicating the viscous component had a greater magnitude value than the elastic

component within almost the whole oscillatory frequency range. Thus, this polymer exhibited an elastic-dominant characteristic for the melt spinning process.

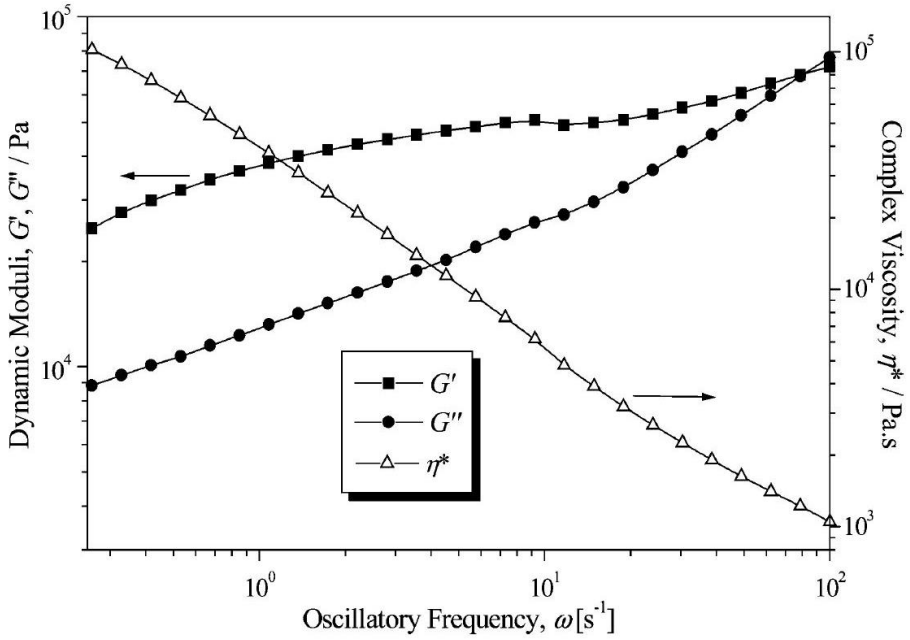

Figure 1.17. Frequency dependence of G', G'', and η^* for sample 6 ($B_{3.0}N_{4.2}C_{1.9}H_{8.7}$) at T_{test} = 195 °C [DUS07].

The authors concluded from the reported results that an appropriate ratio between the viscous ($\boldsymbol{G'}$) and the elastic part ($\boldsymbol{G''}$) *i.e.* $\mathbf{1 < tan\,\delta < 2.3}$ is necessary to facilitate fibre formation during the extrusion polymer process ($\boldsymbol{tan\,\delta}$ representing the ratio of the viscous ($\boldsymbol{G''}$) to elastic ($\boldsymbol{G'}$) response of a viscoelastic material). Furthermore, it was also pivotal to have a minimum level of elasticity $\mathbf{1 \cdot 10^4\ Pa < G' < 3 \cdot 10^4\ Pa}$ for drawing the molten filament into fibres. Polymers manufactured between 160 °C and 180 °C demonstrated appropriate rheological properties to favourably prepare high performance BN fibres. The novelty of this study was to be able to correlate the effect of the architecture on the rheology of the polymers and providing the necessary conditions to forecast the melt-spinnability of poly[*B*-(methylamino)borazine].

1.7.2. Direct ink writing

3-D printing is an additive manufacturing (AM) technique for fabricating a wide range of structures and complex geometries from three-dimensional (3D) model data. 3D printing technology of ceramics mainly includes power bed techniques, laser selective sintering, selective laser melting, DIW, ink-jet printing and stereolithography. In recent years, ceramic fabrication through AM has attracted interest since AM technology permitted to start the manufacturing process from the beginning, consequently, reducing the waste of raw materials. Among the AM methods, the DIW is the one that is primarily concerned with

rheology of PDCs. The following studies have used a MK (polymethysilsesquioxane) resin in the DIW techniques [ZO16] [FR18]. In this way, Zocca *et al*. carried out an investigation on the DIW of a preceramic polymer and fillers to manufacture hardystonite ($Ca_2ZnSi_2O_7$) bioceramic scaffolds [ZO16]. For the ink preparation, the authors made use of a commercially available polymethysilsesquioxane $[CH_3SiO_{3/2}]_n$ (Silres MK polymer, Wacker Chemie, Munich, Germany) which was used as a preceramic polymer. Fumed silica known as a thickening and thixotropic agent in low molecular weight solvents was utilised to alter the rheological properties of the paste. Hence, the inks prepared namely H0, and HF contained a preceramic polymer (MK), fumed silica dissolved in isopropanol and ceramic fillers like ZnO and $CaCO_3$. The difference between H0 and HF is that H0 contained hardystonite filler as well. Rheological tests were carried out such as dynamic oscillation, viscosity recovery and flow curve tests. The dynamic oscillation experiments indicated that the material had a gel-like behaviour with a noticeable plateau at lower shear stress (Figure 1.18a). Moreover, a sudden decrease in storage modulus was noted above a certain yield stress threshold. This could be due to the changes occurring in the microstructural arrangement of the material, which had an influence on the rheological behaviour. The shear-thinning behaviour of the ink was improved as a consequence of the presence of fumed silica.

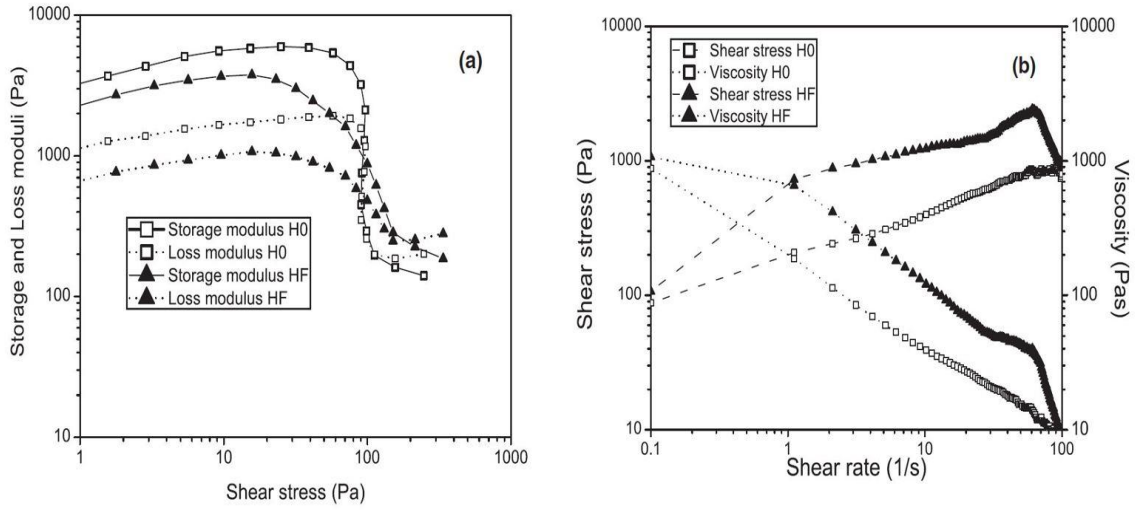

Figure 1.18. (a) Dynamic moduli of the inks as a function of the shear stress (frequency 1 Hz); (b) Flow curve for the inks, showing the shear stress and the corresponding calculated viscosity as a function of the shear rate [ZO16].

Furthermore, a steady-rate sweep test was carried out where the shear rate had a steady raise from 0.1 to 100 s^{-1}. This investigation was performed to verify if the inks had the desired shear-thinning behaviour for DIW applications. Both inks had a high viscosity of the order of 10^3 Pa·s at low shear rate (0.1 s^{-1}) but a decrease of two order magnitudes was

reported when there was an increase of shear rate up to 100 s^{-1} (Figure 1.18b). This behaviour further confirmed the shear thinning behaviour of the inks. In addition, after a preshear of 30 s at a shear rate of 50 s^{-1}, the change of viscosity as a function of time was plotted at a shear stress of 25 Pa as shown in Figure 1.19.

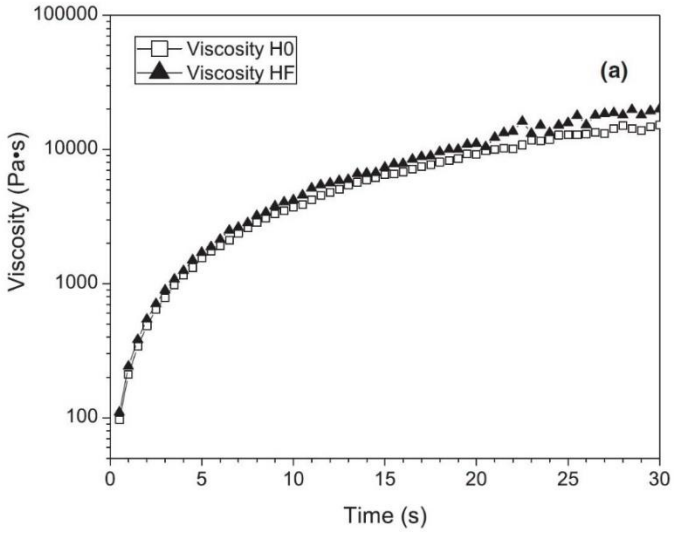

Figure 1.19. Viscosity recovery test for the inks (viscosity/time plot at a constant shear rate of *0.1* s^{-1}, at a *25* Pa shear stress) [ZO16].

Both inks H0 and HF showed a resembling curve. At the start the viscosity was low (<100 Pa·s), but in the first 20 s it rose by two order of magnitude to reach a plateau value. The results obtained support the fact that the two inks have suitable rheology properties for DIW as the viscosity increases happened within a short time span, hence reducing the deformation of the printed, unsupported structures of the scaffold. The authors concluded that the filament deformed within seconds after being extruded but the viscosity of the inks quickly increased and as a result of which the deformation reached a plateau. This increase in viscosity stopped further deformation from happening. The fabricated scaffold had the proper mechanical properties for non-load-bearing bioengineering applications.

In parallel, much interest has been drawn lately in using DIW to obtain ceramic matrix composite (CMC) *via* preceramic polymers. Franchin *et al*. reported for the first time the investigation of an ink consisting of chopped fibres that was appropriate for DIW [FR17]. Their findings suggested that a stronger gel-like behaviour was necessary to keep the structure of the component with respect to the design. Consequently, some adjustments were still needed to optimise the ink rheology, nevertheless a complex CMC structure with a porosity of 75 % and compressive strength of 4 MPa was seemingly achieved. Within a space of one year the authors reported the optimisation and characterisation of preceramic inks for direct ink writing of ceramic matrix composite structures [FR18]. Two inks namely Ink A (composition: isopropyl alcohol, poly(methyl-silsesquioxane) Silres MK*,* SiC carbon fibre,

fumed silica, crosslinker geniosil GF91 and Dispersant BYK180), and Ink B (same components as ink A except it didn't have fumed silica in the mixture) were reported for the rheological tests. Dynamic oscillation tests were carried out to determine the inks transition phase from low rigidity systems at higher shear stress values. Figure 1.20a reports a log-log plot of loss moduli G'' (Pa), storage moduli G' (Pa), and shear stress (Pa) of the inks against strain γ %. The curves of both the inks were alike and could be divided into 3 regions. From low to intermediate strain both G' and G'' displayed a plateau region where $G' > G''$; the shear stress increased constantly. At higher strain, a decrease in the slope of shear stress is observed while G' and G'' decreased promptly before crossing each other.

The behaviour of the inks could be categorised as shear thinning in a large amplitude oscillatory shear (LAOS) system due to the chain orientation. The result of viscosity recovery test performed on the inks is displayed on Figure 1.20b. A recovery of more than two orders of magnitude is noted in ink A before a plateau value of about 50 kPa·s is reached. While ink B started from a relatively higher value than ink A approximately 125 Pa·s and demonstrated a more modest recovery. Around 60 s, both inks appeared to have the same viscosity of about *7.5* kPa·s. The fastest recovery was recorded for Ink A which can be attributed to the fast reconstruction of hydrogen bonds between silica particles. Over a prolonged time, both inks reported different viscosities.

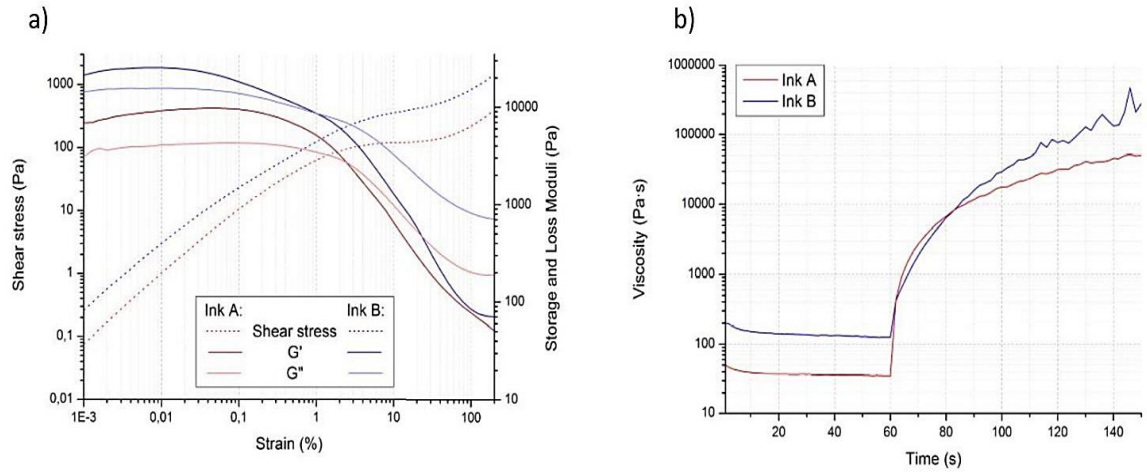

Figure 1.20. a) Storage modulus G' (Pa), loss modulus G'' (Pa); b) η (Pa·s) against t (s) [FR18].

As a conclusion, the results demonstrated that both inks have suitable rheology for DIW, as there is a reduction of deformation of the printed structures due to a rapid increase of viscosity. Ink B had higher values of viscosity over a range of time therefore avoiding the collapse of the layers of the structure during printing. In addition, printed materials could maintain the desired shape and not adding fumed silica in the mixture led to structures

enabled to be used at higher temperatures. Although DIW 3D ceramic composites material showed promising signs, very few studies have been reported.

Most of the studies described above tried to obtain a rheology adapted to their shaping process by either adding additives or modifying the preceramic polymer composition. However, rheology depends as well on the evolution of macromolecular structures during the polymerisation reaction. Consequently, we have turned to other characterisation techniques such as vibrational spectroscopy that could be useful, especially when coupled with a real-time online rheometer. Hence, the combination of these techniques could provide a powerful approach in monitoring chemical and rheological changes in any systems.

1.8. Relationship between changes in molecular structure and rheological behaviour

Most of the studies coupling rheological to vibrational approach use either Fourier transform infrared spectroscopy (FTIR) or Raman spectroscopy. Consequently, studies describing the relationship between changes in molecular structure and rheological behaviour have been divided into two parts. The first one will illustrate studies where an FTIR spectrometer and rheometer were employed while the second part will report studies where a rheometer is coupled with a Raman spectrometer. Among the studies presented in this section, only one study dealt with the PDCs framework (Darsy *et al.* [DA15]).

From the literature, few studies have been described on the coupling of a rheometer with a Fourier transform infrared (FTIR) spectroscopy. In this way in 1997, Chiou *et al.* were the first to mention the use of an FTIR spectrometer and a rheometer to characterise the UV curing kinetics of thiol–ene polymers [CH97]. The measurements with the rheometer and the FTIR spectrometer were not performed simultaneously as the two instruments were not coupled. The FTIR experiments were carried out by using a Nicolet Magna-IR System 750 spectrometer with a DTGS-KBR detector performed in transmission mode while the rheological measurements were performed by Rheometrics mechanical spectrometer (RMS 800) in conjunction with specially designed parallel fixtures. The authors combined the results obtained from those two measurements to better understand the fundamental processes occurring during UV curing. By keeping the same experimental conditions in both setups (*i.e*., on the FTIR spectrometer and rheometer), the authors directly correlated the changes in chemistry and monomer conversion obtained from real time FTIR spectroscopy to *in-situ* rheological measurements. Combining the macroscopic properties data such as loss and storage moduli from rheology with molecular properties such as monomer conversion from FTIR spectroscopy, will result in a better understanding of the fundamental processes occurring during UV curing. *In-situ* monitoring of polymerisation reaction had drawn interest of several scientists since it allowed for real time measurements of the

samples, giving the researcher the advantage of maximising and synchronising the data gathered from a single measurement. It also allowed for the characterisation of the sample bearing the same thermal, mechanical and structural history. Hence, the total experiment time is reduced compared to e*x-situ* monitoring [RE14]. The following reported studies dealt with real time monitoring carried out by the coupling of a rheometer with an FTIR spectrometer (Haake Mars III^{TM}, ThermoFisher coupled with Nicolet iS10^{TM}). The FTIR spectrometer used the attenuated total reflection (ATR) principle with a diamond surface area of 1 mm^2.

Liu *et al.* were the first ones to study this dynamic coupling, by describing the crosslinking of a vinyl ester resin (VER) *via in-situ* and *ex-situ* FTIR measurements [LI14]. The measurements were performed in both steady shear and oscillatory mode using 35 mm parallel plate geometry. The *ex-situ* measurements were accomplished by a Bomem Michelson MB100 FTIR spectrometer in transmission mode. Samplings from the rheometer were performed by manually pausing the rheometer and the partially polymerised samples were quenched in liquid nitrogen and mixed with dry KBr powder to form a pellet for *ex-situ* FTIR measurements. The authors pointed out the interest of the *in-situ* FTIR measurements, in comparison with the *ex-situ* method, for the monitoring of polymerisation processes. Moreover, rheological measurements were used to observe the build-up of the polymer-nanoparticle network – as it leads to changes in viscoelastic properties of the material (the storage modulus, the loss modulus and viscosity). The authors combined rheological measurements with FTIR data to achieve a better perspective of the structural changes taking place. A set of nanocomposites was prepared by the inclusion of organoclays into a VER matrix to obtain VER/clay nanocomposites. They found out that the *ex-situ* measurements tend to underestimate the fractional conversion. The authors attribute this to the *ex-situ* measurements shortcomings such as interrupting the rheological measurement for sampling purposes. Therefore, they drew the conclusion that performing *in-situ* FTIR measurements during the rheological experiments is more suitable and probably reflects the polymerisation process more realistically.

Studying the implementation of self-healing capabilities in existing polymeric networks, Bose *et al.* focused on the Diels–Alder (DA) reversible reactions [BO14]. DA reactions (The *Diels-Alder* reaction is one in which a conjugated diene bonds in with an alkene to produce a cyclohexene molecule) take place between a diene and a dienophile at a temperature range of 23 °C to 80 °C and can be altered back to its initial form through the retro-Diels-Alder (rDA) reaction occurring at temperatures above 120 °C. Due to the reversibility of the reaction between a diene and a dienophile, sufficient mobility to the network is created to flow locally and to repair surface cracks and scratches. Although that the reversibility of the chemical reaction has been illustrated previously *via* surface scratch

disappearance, the molecular reversibility was not associated with macroscale flow and healing – this is what the authors set out to do in this study by combining FTIR spectroscopy with oscillatory shear rheological measurements. A parallel plate geometry of 20 mm diameter was used during all oscillatory shear mode for all experiments. Four polymers (P1, P2, P3 and P4) were synthesised by a free radical polymerisation reaction as shown in Figure 1.21. P1 had both DA moieties (furan and maleimide) while P2 and P3 had only one of each (furan or maleimide). The last synthesised polymer P4 had only the lauryl group.

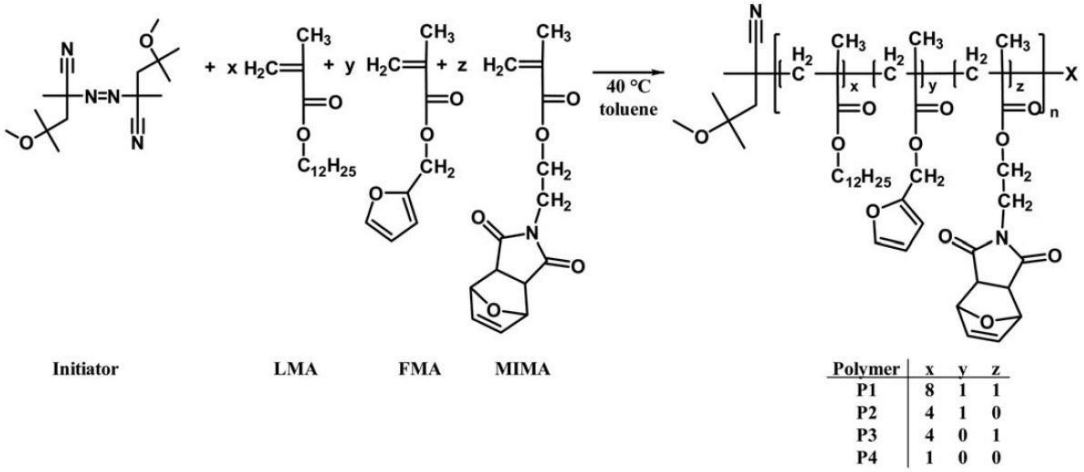

Polymer	x	y	z
P1	8	1	1
P2	4	1	0
P3	4	0	1
P4	1	0	0

Figure 1.21. Schematic representation of the polymer samples. Functional PLMA with furan and maleimide pendant groups (P1), functional PLMA with only furan pendant groups (P2), functional PLMA with only maleimide pendant groups (P3), and unfunctionalized PLMA (P4) [BO14].

By mixing the FTIR results with the observed rheological data, one can better understand the structural changes occurring during the crosslinking/decrosslinking of the polymer P1. Based on the rheology results, self-healing P1 (furan & maleimide) exhibited repeated reversibility of DA and rDA reactions as shown in Figure 1.22. Interchanging between DA and rDA temperature demonstrated crosslinked ($G' > G''$) and decrosslinked ($G'' < G'$) states of the polymer network. In all three experimental temperatures (100, 120 160 °C), rDA reaction took place. The six heating and cooling process put in evidence the viscoelastic reversibility of P1.

Furthermore, FTIR data allowed for the determination of peak intensities related to the reaction of the furan and maleimide units. At 160 °C the polymer experienced rDA reaction where the normalised maleimide peak intensity increased steadily until a maximum was reached.

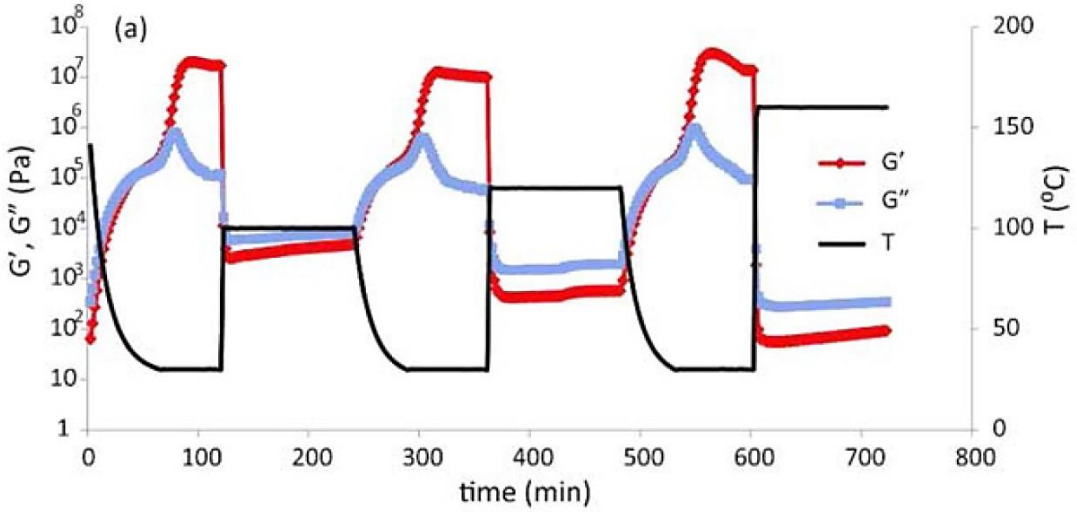

Figure 1.22. Reversible crosslinking and decrosslinking of the self-healing polymer network at DA and rDA temperatures in the copolymer (P1) [BOS14].

At 40 °C, DA reaction occurred and the maleimide peak intensity decreased back to its initial value. Hence, the same result in network reversibility was noted for both FTIR and rheological data in the case of polymer P1. Therefore, the integration of both furan and maleimide functionalities give way to a polymer self-healing abilities and high complex modulus.

While for P3, it was observed that it crosslinked at a temperature of 100 °C, however this crosslinking was irreversible in consequence of G' remaining higher than G'' during the cooling the heating processes. Moreover, P2 and P4 did not crosslink at temperature superior than 100 °C during the heating and cooling cycles. Thus, P2, P3 and P4 exhibited partial viscoelastic recovery with no proper self-healing properties. The authors demonstrated that synthesised self-healing polymer (P1) with a high modulus in the crosslinked state can be obtained. This study was another example of the advantages of coupling *in-situ* FTIR data with rheological ones to have a better insight in the chemical reactions (DA and rDA reaction).

In search for biodegradable plastics, Auriemma *et al.* compared poly(3-hydroxybutyrate) (PHB) which is a biodegradable polymer with another PHB doped with a natural polyphenolic additive (tannic acid TA) [AU15]. The goal of this study was to investigate the thermal stability of both neat and TA-doped PHB samples by means of a rheometer and FTIR spectrometer. The deterioration of the samples was observed by following the viscoelastic moduli as a function of time. The rheological results indicated that the neat PHB underwent degradation since the decrease in elastic modulus is due to the polymer molecular weight dropping below the critical value for entanglement formation. Moreover, neat PHB could not be processed at 180 °C since the polymer was not yet in a

molten state. Figure 1.23 illustrates the time dependent oscillatory rheology of PHB/TA15 (PHB with 15 % tannic acid) at 180 °C.

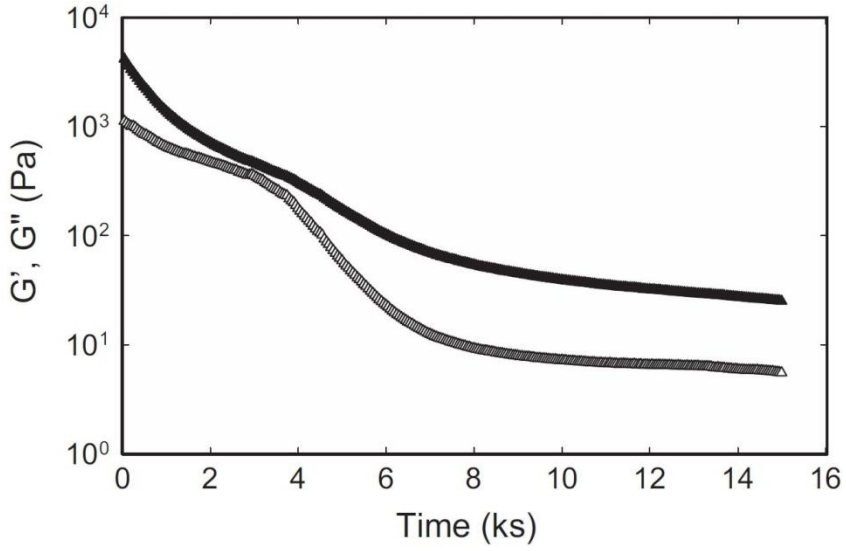

Figure 1.23. The time evolution of the elastic modulus (empty symbols) and the loss modulus (filled symbols) of PHB/TA15 at 180 °C. The angular frequency is 10 rad/s, the stress amplitude is 50 Pa [AU15].

By comparing the measurements of the neat PHB sample with the PHB/TA15 occurring at the same temperature, higher values of moduli were recorded (a difference of two orders of magnitude between) revealing that a complete melting is achieved. In the case of the TA-doped sample there was a much less pronounced decrease of the elastic modulus with respect to time. A stable, intermediary region was found where the degradation was delayed and reduced. FTIR spectroscopy was used to get an insight on the stability of the mechanism arising due to TA. FTIR spectra of the samples were collected during the rheological measurements at 180 °C. By comparing the PHB/TA15 spectra with the PHB spectra, an increase in TA absorption peaks was noticed together with a reduction of the absorption band at 1730 cm^{-1} (attributed to ester carbonyl stretching) and an occurrence of a signal at 1705 cm^{-1}. This result can be associated with the generation of intermolecular hydrogen bonds between carbonyl of PHB and hydroxyl of TA. The author's findings indicated that the TA-doped sample increased the processing window of the polymer as well as the thermal stability. Consequently, processing can be carried out at lower temperatures.

In the IRCER, Darsy *et al.* reported the monitoring under controlled atmosphere of a polycycloaddition *via* the coupling Rheo-FTIR. [DA15]. A click reaction was carried out in the presence of Cu (I) as catalyst between well-defined monomers namely tripropargylamine (TPA) and bis(azidomethyl)dimethysilane (BDAM) to synthesise a hyperbranched polycarbosilane as shown in Figure 1.24. The monitoring of both the structure of the growing macromolecules and their rheological behaviour during the polymerisation reaction was performed simultaneously under controlled temperature and atmosphere.

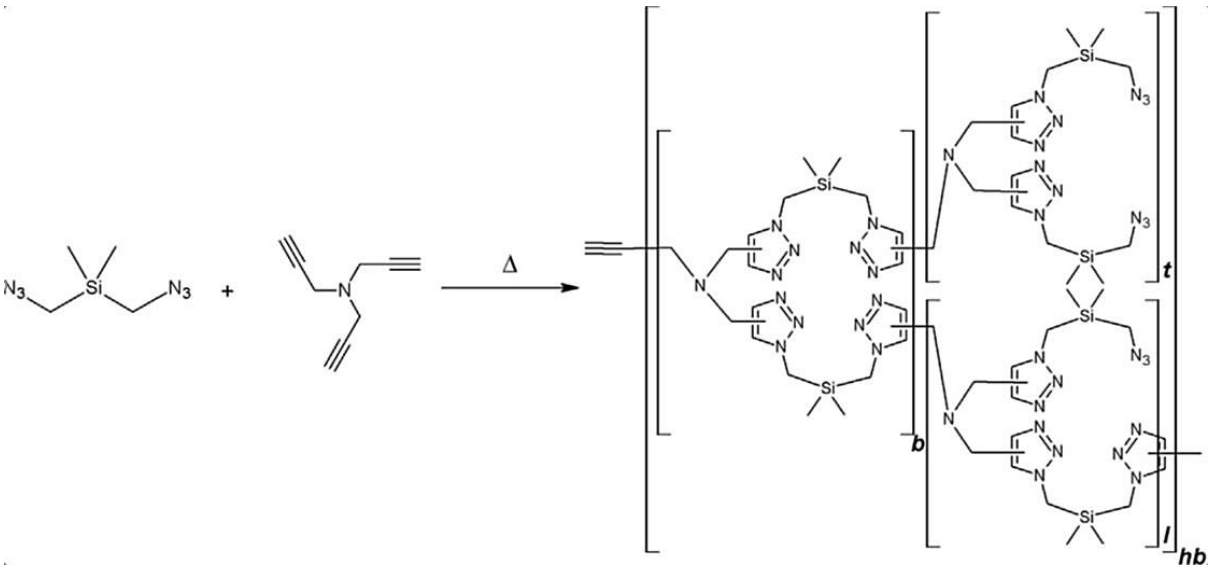

Figure 1.24. Scheme of the hyperbranched polycarbosilane by reaction between BDAM and TPA (b = branching, *t* = terminal, *l* = linear, and *hb* = hyperbranched) [DA15].

The experiment was carried out at three different temperatures namely 85, 90 and 95 °C. All measurements data were coupled. Thus, the changes in molecular properties (such as conversion obtained from FTIR spectroscopy) were linked to the changes in macroscopic properties (such as the dynamic moduli and complex viscosity form rheological measurements).

No apparent impact on the polymer structure was observed when subjected to different atmosphere (either air or argon); therefore, all rheological measurements were carried out in air. Even with varying temperature, the polymer remained viscous according to the rheological moduli values obtained. By following the evolution of the azide stretching band at 2087 cm^{-1}, it was feasible to calculate the azide conversion as a function of time (Figure 1.25a). The azide conversion increased rapidly in the incipient stages of the reaction with an increase in temperature. After 4000 s, the azide conversion was 0.7, 0.8 and 0.9 for the temperature of 85 °C, 90 °C and 95 °C, respectively. A critical azide conversion of 0.7 was noted and it was referred to as the quantity of consumed azide needed to have an impact on the rheological behaviour (it coincided with the beginning of the increase in complex viscosity Figure 1.25b of the developing polymer. Furthermore, this value corresponded to the conversion rate of 0.71 observed at gel point for a $A_2 + B_3$ polymerisation type based on the theory of gelation of Flory-Stockmayer.

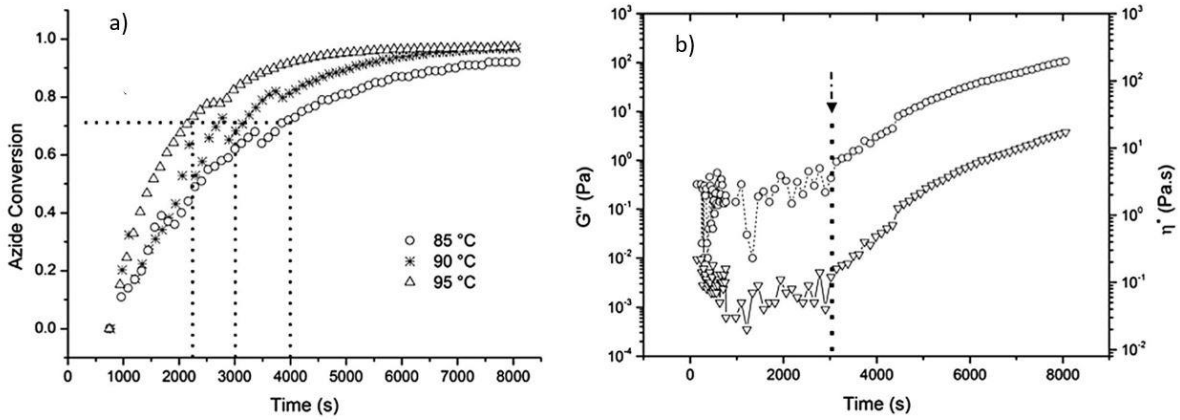

Figure 1.25. a) Azide conversion plotted as a function of time; b) Semi-log plot of the evolution of elastic (G'', circle) and complex viscosity (η*, down triangle) during the polycycloaddition at 90 °C [DA15].

In addition, an activation energy of *73.3* kJ·mol^{-1} for the 1,3-dipolar polycycloaddition was found. Even though promising results were obtained in terms of kinetics and rheological behaviour, the coupling set-up had some limitations as well. The authors noted a difference in the polymer growth between the lower surface of the geometry and inside the sample. This was likely because the FTIR spectrometer could retrieve information in ATR mode through the diamond window situated in the lower plate of the rheometer. Consequently, only the lower surface of the sample, which is in contact with the ATR diamond, is being monitored during the experiment. This limitation could be overcome by using a Raman lens (Raman spectroscopy), to retrieve information in volume since it analysed the samples with a greater penetration depth.

Studies about the combination of a rheometer with a Raman spectrometer have been scarcely reported in the literature. Among those studies, Chevrel *et al*. made use of a laboratory made rheo-Raman setup to monitor continuously a free radical reaction of acid acrylic in aqueous solution [CH12]. The interest of the authors was to find out whether the rheo-Raman setup would provide satisfactory primary results for the continuous *in-situ* monitoring of acrylic acid polymerisation under defined conditions. The setup composed of a rheometer in a Couette configuration and a Raman spectrometer with a non-contact fibre optic probe was located outside quartz vessel as shown in Figure 1.26.

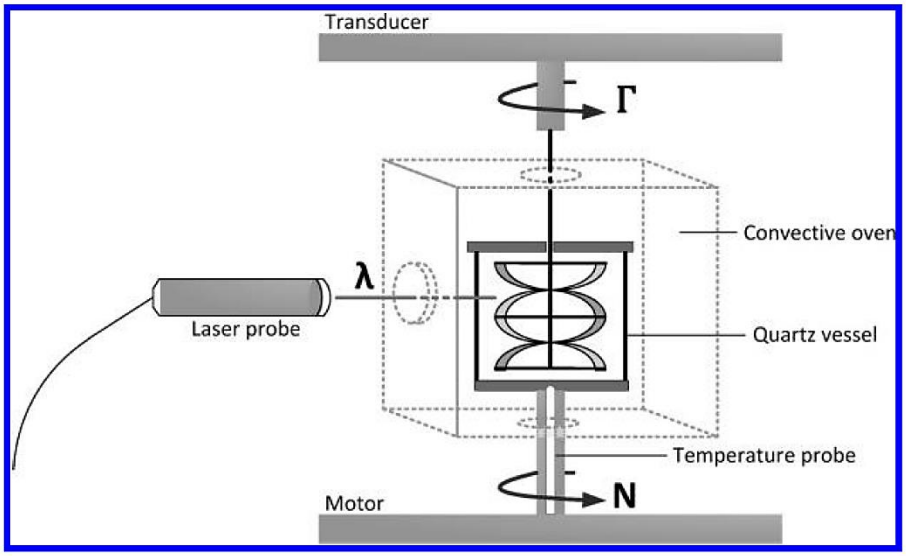

Figure 1.26. Scheme of the rheometer−Raman spectrometer coupled experiment [CH12].

From the obtained Raman spectra, the C-H bond which decreases with monomer consumption was used to monitor the reaction. In addition, the O-H band of water at 3400 cm^{-1} remained unchanged during the reaction. Thus, the latter normalised the Raman spectra. The impact of the different monomer concentrations as a function viscosity variation and polymer formation was studied as illustrated in Figure 1.27. It was noted that the polymer formation and viscosity increased rapidly for higher initial monomer concentration. For instance, it was reported that for a 15 wt. % of initial acrylic acid concentration, the viscosity increased for almost four orders of magnitudes while for a 5 wt. % of initial acrylic acid concentration, the viscosity increased for almost two orders of magnitude.

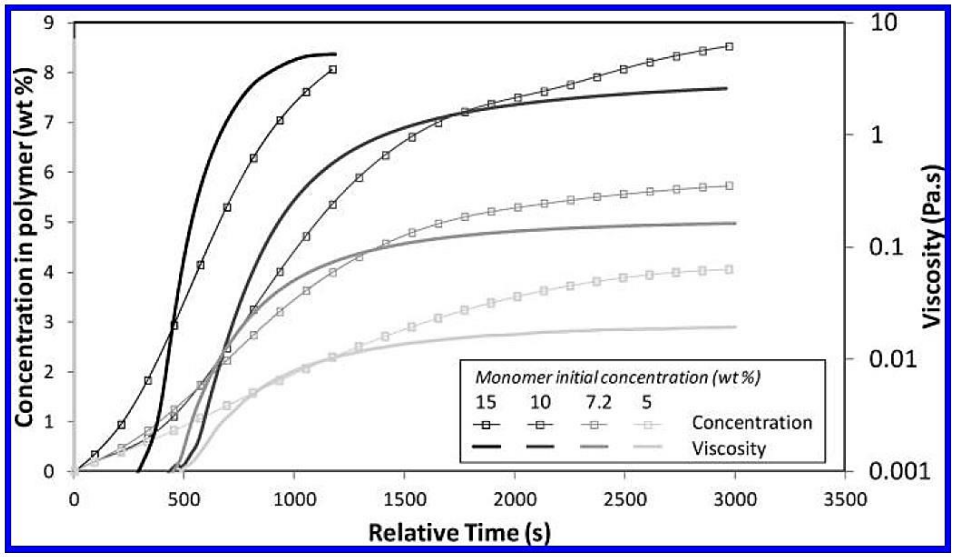

Figure 1.27. Evolution of viscosity (at 10 s^{-1}) and concentration of polymer during the polymerisation process. The initial concentration of monomer was varied between 5 wt % and 15 wt % while the initial concentration of the initiator was kept equal to 0.2 wt %. The abscissa corresponds to reaction time minus the duration of the induction period [CH12].

The different initiator concentrations were studied by keeping the monomer concentration constant. It was reported that the reaction rate decreased with a decrease in initiator concentration while the viscosity of the medium increased for specific monomer concentration. At higher initiator concentration, the polymerisation was accelerated leading to formation of smaller macromolecules. These findings demonstrated that the rheo-Raman platform managed to overcome three main difficulties encountered during monitoring of polymerisation reaction. Firstly, the viscosity of the medium together with the monomer conversion were perpetually followed with well-defined conditions such as temperature. Secondly, macroscopic viscosity could be directly linked to structural changes. Finally, the mixer type rheometer gave scalable results especially with regard to stirring conditions.

Remaining in the field of monitoring of polymerisation process, Brun *et al.* published a study where they utilised the Raman spectrometer to investigate the synthesis of high-impact polystyrene (HIPS) based on the free radical polymerisation of styrene in the presence of polybutadiene (PB) [BR14]. The interest of the study was on how to use Raman devices such as the immersion and non-contact (lens) probes, to enable monitoring of the HIPS synthesis at the molecular scale (chemical processes, variations in bond angles, etc.) along with micrometric scale (formation and evolution of PB nodules). A control experiment was conducted with absence of PB in the mixture reactor. The immerse probe and external probe were utilised simultaneously to monitor the bulk styrene thermal polymerisation. The authors observed that the normalised intensity of the double bond signal dropped linearly with monomer consumption. More importantly, the results showed that comparable results were obtained for both probes concerning the styrene conversion in a homogeneous reaction medium. On the other hand, when PB was present in the reaction mixture, the immerse probe signal qualitatively matched the result from the experiment without PB that is the normalised intensity of the double bond decreased regularly with time. In contrast with the external probe, the authors have distinguished three domains as shown in Figure 1.28. In the first domain, signals from both probes were in agreement with other; in the second domain, the intensity of the signal from the external probe displayed a sharp increase (due to contribution of diffusion). In the third domain, the signal from the external probe was stabilised.

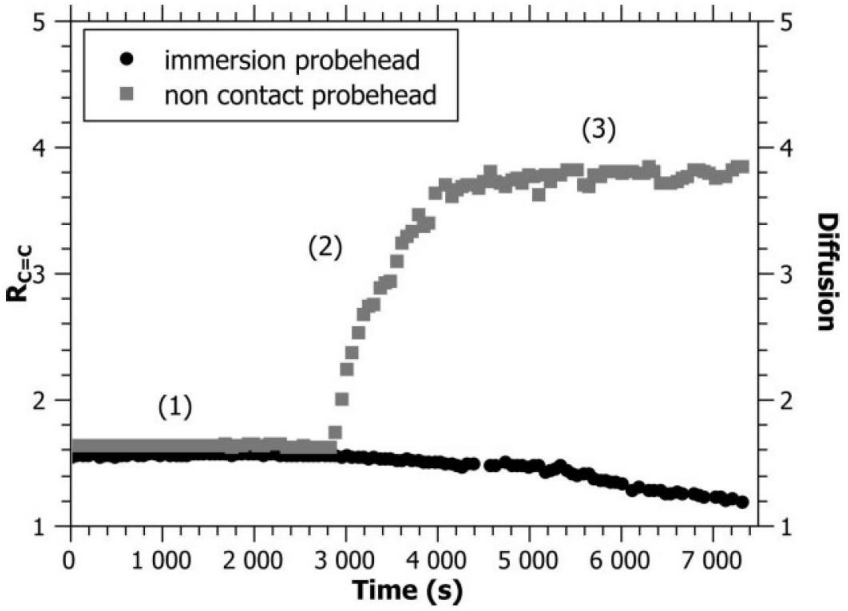

Figure 1.28. Comparison between Raman signals [BR14].

Therefore, the styrene conversion could be monitored during the whole HIPS process (either in heterogeneous or homogeneous medium) by an immerse probe while the external Raman probe provide information about the phase separation during the HIPS process. The immersed probe analysed a volume of approximately less than 1 μm^3 while for the external probe it is about 100 μm^3. Subsequently, the external probe analysed a greater conical volume of reaction medium than that of the immersed probe. Therefore, the non-contact probe could detect the light diffusion phenomena occurring during phase separation. Information about the styrene conversion or phase separation and phase inversion were acquired by using the immersed and external probe. Finally, the HIPS process was investigated continuously *in-situ* with a rheometer in a Couette analogy coupled with a Raman spectrometer (external probe). In this way, it was feasible to link Raman results to the viscosity of the reaction medium.

There was a certain amount of interest in producing model of polymerisation reactors aided by experimental data that can improve the design and optimised the industrial plants. The Rheo-Raman platform combined with mathematical model of the reaction medium seemed to be the appropriate way to access such knowledge. Hence, Chevrel *et al.* carried out a free radical polymerisation of acrylic acid in up to 60 wt. % aqueous solutions mix with potassium persulfate as the initiator in the rheo-Raman platform [CH14]. An overall rheo-kinetic modelling for different reactant concentrations were generated in order to find out the influence of the initiator and monomer feed concentration as well as the process conditions (temperature and shear rate). Experimental data were compared to kinetic model and rheological equations obtained from literature. For an acrylic acid feed concentration up to 15

wt. %, the authors found out that the calculated curves fitted the experimental data for both polymer concentration and viscosity of the medium. Moreover, polymerisation in conditions displaying gel effect was studied. In this way, three monomer concentrations between 40 wt. % to 60 wt. % acrylic acid were used to determine the influence of shear on the occurred gel effect. It was feasible to prevent gel effect by exerting a high enough shear rate on a concentration of 40 wt. % while for concentration ranging between 50 wt. % to 60 wt. % gel effect was only prolonged with increasing shear rate. Thus, the development of a rheo-kinetic model of the free radical polymerisation carried out on rheo-Raman device, have allowed in turn to develop pilot scale experiments.

1.9. Conclusion

The bibliography study evidenced the state of art of non-oxide ceramics in terms of shaping and monitoring of syntheses. As stated before, among the non-oxide ceramics, silicon carbide is of particular interest. SiC can be produced *via* the polymer ceramic routes also known as PDC route. Among the possible synthesis routes presented, the hydrosilylation is an appealing one since the reaction directly involves the reactivity of elements such as silicon, carbon and hydrogen from defined monomers in a one-step

reaction. In addition, it provides control of the elements and composition in comparison with a commercial polymer. In parallel, the study carried out on rheology of preceramic polymer allowed researchers to have a better understanding how to characterise our materials in order to shape the polymer in any desired form. However, there was a lack of information on the chemical changes occurring during polymerisation/crosslinking process. Consequently, studies have been reported that combined either a rheometer with an FTIR spectrometer or a rheometer coupled with Raman spectrometer. These studies demonstrated how to characterise the rheological properties and chemical changes occurring during a reaction. But no study has ever attempted to combine both vibrational techniques to a rheometer simultaneously.

To reach this goal and to recover information in volume in the Rheo-FTIR platform, it was undertaken to use a Raman fibre spectrometer, as it is possible to analyse the samples with a greater depth of penetration. In addition, the complementarity of Raman and IR spectroscopy could be interesting in terms of simultaneous monitoring. The Raman head of the spectrometer will be used with a collection lens. The depth that will be probed will be higher than 100 µm, which is 10 times more than by ATR mode during the FTIR. This new platform would be a powerful tool to carry out experiments on polymerisation with both a structural and shaping point of view of the growing preceramic materials, from functionalised carbosilanes, obviously presenting a suitable signature for the FTIR and Raman monitoring. Another key characterisation concerns the molar masses of the new generated macromolecules, to understand their growth, models linking their rheology to the evolution of macromolecular structures during syntheses is envisaged. Most of the time, to access such information the Gel Permeation Chromatography (GPC) is coupled with refractive index (RI) or UV detectors, but the retrieved data is only relative, and does not reflect the real mass, especially for complex structures. Fortunately, a family of detectors, named Multi-angle Light Scattering (MALS), is able to determine absolute molar masses, sizes (root mean square (RMS) radius), and conformation of macromolecules and particles in the solution. To complete the aforementioned instrumentation, and to create a unique, coherent, and polyvalent platform of analysis, the addition of Size Extrusion Chromatography (SEC) and MALS to the platform Rheo-Raman-FTIR, would allow us to access vital information during monitoring of the polymerisation of carbosilanes. The establishment of this unique platform as shown in Figure 1.29 therefore would constitute an instrumental key in the fundamental study of the rheology of preceramic polymers.

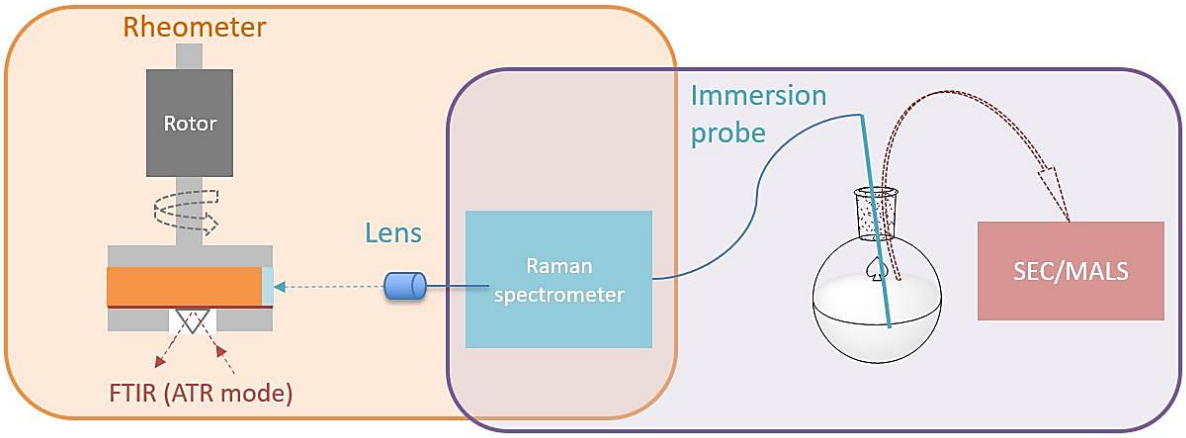

Figure 1.29. Schema of the Rheo-FTIR-Raman coupled with a SEC/MALS.

Several risks exist in this project, with different impacts or likelihoods (Figure 1.30). First, regarding the synthesis part, the choice of the starting monomers will be a crucial step. Indeed, because the final desired material is SiC, the ratio Si/C will need to be close to 1, to avoid free carbon in the ceramic, after pyrolysis. Moreover, the functionalities of monomers, leading to different degrees of branching, would be taken into account, as they impact the rheological behaviour of the polymer. In addition, a compromise will have to be found between a high ceramic yield and the rheological properties of the polymers for a suitable shaping. The composition and the structure of the growing polymers would probably bring answers to this problematic, particularly thanks to the MALS detector. The dilution factor in an appropriate organic solvent will also have to be optimised in order to use the same conditions on the rheometer as in the round bottom flask. Indeed, the concentration of organic precursors (monomers or polymers) should be sufficient to allow for the detection of a characteristic signal by the two spectrometers, during the monitoring. In addition, particular attention will be paid to the kinetic of the polymerisation, to bypass reactions that are carried out too fast, often leading to shaping issues. Another risk will be linked to the sensitive character of polycarbosilanes in air environment. This can cause crosslinking reactions independent to the polymerisation. To avoid this possibility, an inert atmosphere such as argon could be used both during the synthesis on the rheometer, during thanks to adapted hoods and inlets for Ar atmosphere, and in batch mode.

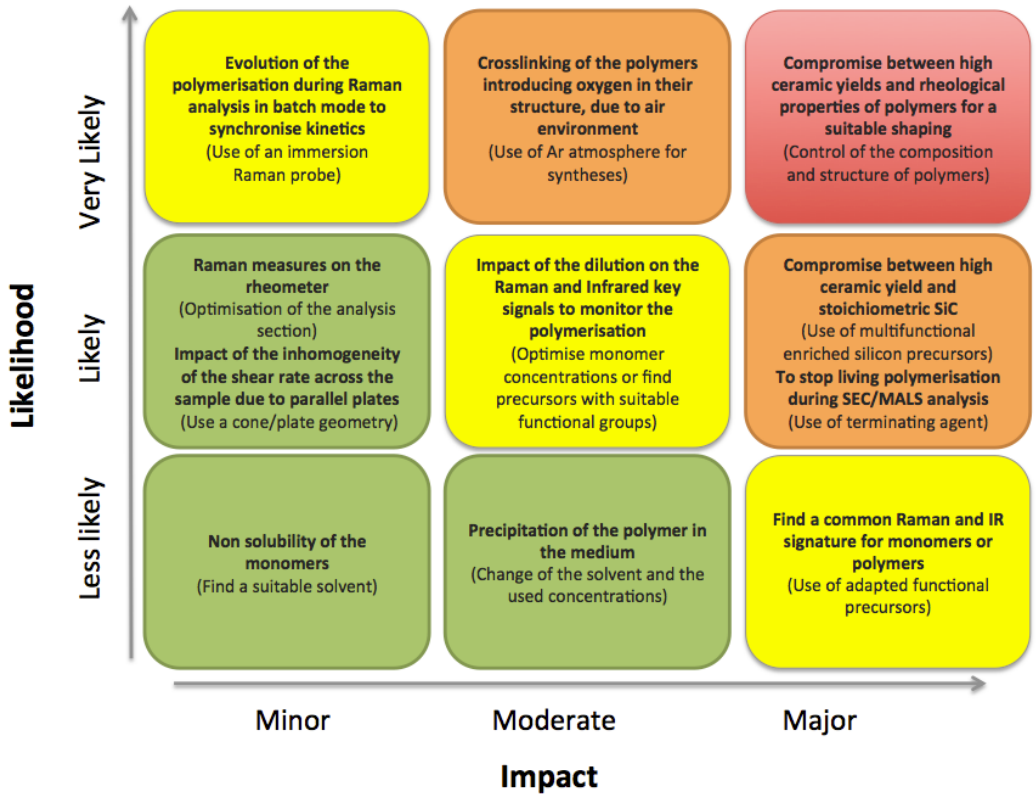

Figure 1.30. Risk diagram and proposed fall-back solutions in brackets.

Secondly, a risk will be present to retrieve suitable data with a Raman fibre spectrometer. A fall-back will be to adapt the section of analysis, by optimising the beam diameter according to the space between the two plates of the rheometer. Furthermore, the non-constant shear rate across the sample in the plate/plate geometry could have consequences on the polymerisation reaction. A solution to avoid this effect would be to use cone/plate geometries. Finally, to avoid the risk of not clearly linking the data from the Size Exclusion Chromatography (SEC)/MALS detector during the regular flask synthesis, to the kinetic of the reaction performed with the rheometer, samples will be taken for the batch synthesis in order to analyse them by Raman spectroscopy. Indeed, it will allow for the *in-situ* monitoring of polymerisation reactions during both the regular synthesis and the one carried out with the rheological platform. However, the solution samples from the batch synthesis will certainly evolve during the analysis, creating the risk of not properly linking the results of Raman spectrometry to the time of extraction. To overcome this drawback, an immersion Raman probe could be used as a means of control. The synchronisation of the kinetics followed on either batch mode or in the rheometer would be ensured.

Chapter 2.

Experimental techniques

2.1. Introduction

This chapter will describe the experimental protocols and the analytical techniques employed during the different stages of the PDC route. The choice of the raw materials used and the polymerisation protocol employed will be presented. The different experimental characterisation techniques to monitor the *in-situ* polymerisation reaction will be described along with the experimental techniques used to characterise the synthesised hyperbranched polymer.

2.2. Selection of reagents

A hyperbranched polycarbosilane is generated *via a* hydrosilylation reaction by reacting difunctional and tetrafunctional monomers together in the presence of a catalyst and a solvent as illustrated by Figure 2.1., 1,4-bis (dimethylsilyl)benzene (BDSB) is the difunctional monomer while the tetraallysilane (TAS) is the tetrafunctional monomer. The catalyst used during the reaction is platinum-based, named as Karstedt's catalyst, which is well known for its extensive use in hydrosilylation reactions due to its selectivity and high activity. Finally, toluene, which is a common solvent in organic chemistry, is employed in the polymerisation reaction.

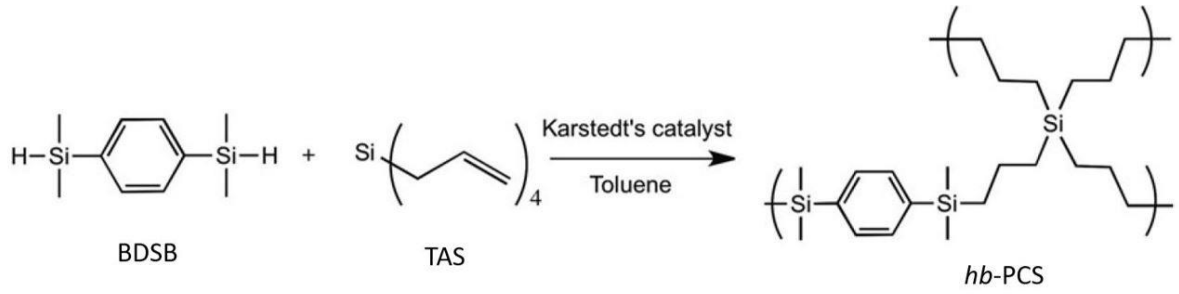

Figure 2.1. Synthesis of a hyperbranched polycarbosilane (*hb*-PCS) by hydrosilylation [PI18].

The origin of the reagents and solvents used in this work is presented in Table 2.1. All these compounds are commercially available and used as received. The indicated purity is the minimum purity guaranteed by the supplier.

Table 2.1. List of reagents used in this work.

Reagents and solvent	Purity	Supplier
1,4-bis(dimethysilyl) benzene (BDSB) $C_6H_4[SiH(CH_3)_2]_2$	97%	Merk
Tetraallysilane (TAS) ($C_{12}H_{20}Si$)	97%	Merk
Platinum(0)-1,3-divinyl-1,1,3,3-tetramethydisiloxane complexe ($C_8H_{18}OPtSi_2$)	98%	Merk

Toluene ($C_6H_5CH_3$)	99.8%	Merk

2.3. Polymerisation protocol

In this work, the polymerisation process took place on two rotational rheometers. The first one was a rotational rheometer (Model AresG2) with a Couette configuration equipped with a spectrometer Raman Kaiser optics (RXN2) from the Laboratoire Réactions et Génie des Procédés (LRGP-Nancy). The second rotational rheometer (Mars III, Thermo Scientific) with a plate-plate configuration equipped with a spectrometer Raman Kaiser optics (RXN1) from Institute of Research for CERamics in Limoges (IRCER). For sampling purposes, the polymerisation was carried out in round bottom flask (RBF) as well. The concentration of reagents (TAS, BDSB and the Pt catalyst) were kept identical even though their volume was varied according to the instruments being employed.

2.3.1. Polymerisation protocol on rotational rheometer (Model AresG2)

The polymerisation procedure carried out at LRGP-Nancy on rotational rheometer (Model AresG2) consisted of mixing 957 µL of TAS (319 mmol·L^{-1}), 1915 µL of BDSB (664 mmol·L^{-1}) in a quartz vessel with 10 mL of toluene. The addition of 100 µL Pt catalyst (0.415 mmol·L^{-1}) in the quartz vessel started the polymerisation reaction. Simultaneously, the rheological and Raman data acquisitions were launched as soon as the catalyst was added to the reaction mixture.

2.3.2. Polymerisation protocol on rotational rheometer (Mars III, Thermo Scientific)

The polymerisation procedure on the rotational rheometer (Mars III, Thermo Scientific) consisted of mixing 73.8 µL of TAS (319 mmol·L^{-1}) and 148 µL of BDSB (664 mmol·L^{-1}) in a test tube with 702 µL of toluene. At the same time, the rheometer was set in terms of inertia and gap. The addition of 77.1 µL catalyst solution (0.415 mmol·L^{-1}) in a test tube started the reaction. Within seconds, the mixture was loaded in between the plates of the rheometer. The rheological, Raman and FTIR data acquisitions were initiated once the mixture was placed in between the plates of the rheometer.

2.3.3. Polymerisation protocol in round bottom flask (RBF)

The polymerisation procedure in RBF consisted of mixing 369 µL of TAS (319 mmol·L^{-1}), 739 µL of BDSB (664 mmol·L^{-1}) and 3.5 mL of toluene in the RBF. The addition of 385 µL catalyst solution (0.415 mmol·L^{-1}) started the polymerisation reaction in the RBF. At the same time, the Raman acquisition was launched when the catalyst was added to the reaction mixture.

2.4. Rheological behaviour of polymer

Rheology is the science that deals with the deformation and flow of matter [RE58]. When a certain mechanical force is applied on a polymer, the stress generated and the polymer's response allow us to determine the rheological properties of the polymer, such as its viscosity. Viscosity can be defined as the internal friction or a measure of resistance to flow. For Newtonian fluids it is described by equation 2.1, where σ is the shear stress, $\dot{\gamma}$ is the strain rate and the constant of proportionality η is called the coefficient of viscosity [BA89]. It is worth adding that the viscosity is significantly affected by variables such as shear rate, temperature, pressure and time of shearing.

$$\sigma = \eta \dot{\gamma} \qquad \text{Eq. (2.1)}$$

Various rheological behaviours of polymers exist according to the different relationships between shear stress (σ) and shear strain rate ($\dot{\gamma}$) (Figure 2.2).

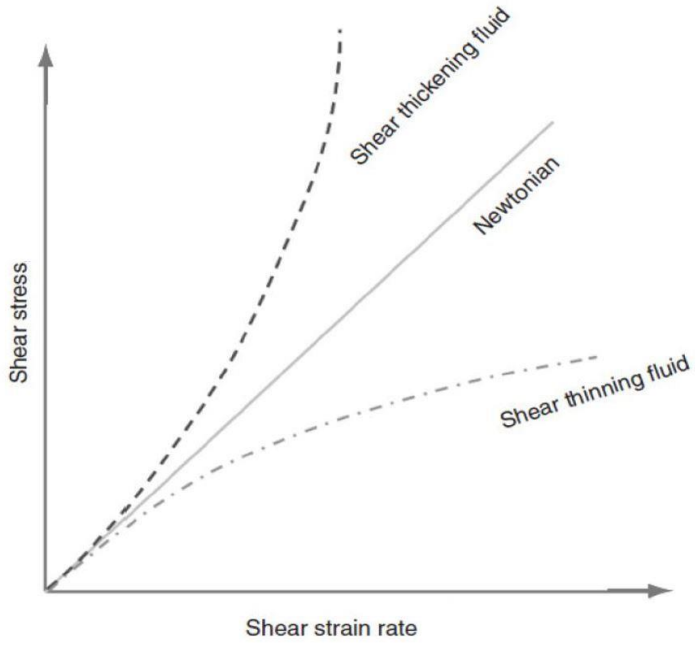

Figure 2.2. Shear stress vs. shear strain rate [CH18].

A Newtonian fluid demonstrates a linear relationship between the shear strain rate and shear stress. The other types of fluids are called non-Newtonian fluids. Normally, a fluid is characterised as a shear thinning fluid when its viscosity decreases with increasing shear rate while when its viscosity increases with increasing shear rate it will be referred to as shear thickening fluid [CH18]. The power law model is used to describe this behaviour according to the expression:

$$\sigma = K\,\dot{\gamma}^{n}\,, \qquad \text{Eq. (2.2)}$$

where n represents the flow behaviour index, K the flow consistency index and $\dot{\gamma}$ the shear rate.

Polymers are generally viscoelastic materials, which are in an intermediate state between the ideal liquid and solid states. Usually, the viscoelastic behaviour of materials is explained by the use of mechanical models, which consist of dashpot and springs (Figure 2.3). The spring obeys Hooke's law due to its elastic element. When a fixed spring is subjected to a stress, it will deform immediately and will maintain its deformation as long as the constraint is maintained. When the stress is removed, it returns to its initial state. On the other hand, the dashpot obeys Newton's law of viscosity due to its viscous element. Hence, when a stress is applied to the dashpot, the deformation keeps increasing as a function of time. Unlike the spring, the dashpot does not recover from the applied stress. The combination of the springs and the dashpot either in parallel or in series or a combination of both gives rise to new models such as Maxwell model or Kelvin model [PA18]. These models contribute to a better understanding of the rheological behaviour of polymeric materials.

Figure 2.3. Analogical representations and material relationships for the elastic element Hooke and the viscous element Newton [BA06].

Furthermore, dynamic oscillation tests play an important role in characterising rheologically complex fluids (viscoelastic), since they can simultaneously exhibit qualitative and quantitative rheological properties such as viscosity and elasticity. In dynamic oscillation tests, a sinusoidal signal (respectively an oscillatory signal represented by a periodical function) with known amplitude (γ_0, respectively σ_0) and known angular frequency ω is applied to a material,

$$\gamma_{IN} = \gamma_0 \sin \omega t \qquad \text{(strain controlled)} \qquad \text{Eq. (2.3)}$$

$$\sigma_{IN} = \sigma_0 \sin \omega t \qquad \text{(stress controlled)} \qquad \text{Eq. (2.4)}$$

and the material measured response (output) *σ(t)*, respectively *γ(t)*, are represented by a periodic function with the same angular frequency *ω* but with a phase difference of angle *δ*.

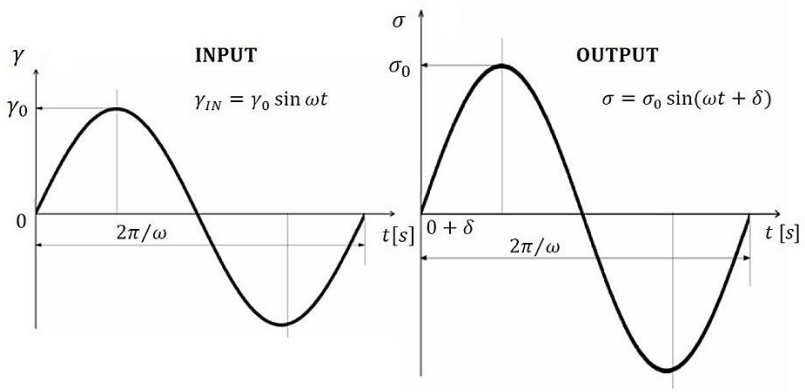

Figure 2.4. Input and output signals for a strain controlled oscillatory test (the graphs are similar for the stress controlled test) [BA06].

In Figure 2.4 the material response to an input signal with controlled amplitude is considered to be sinusoidal as well. In this case, it is said that the oscillatory regime is in the domain of the small inputs oscillation amplitude (SAOS –Small Amplitude Oscillatory Shear). In general, the periodically output signal can vary, being represented by a harmonic odd Fourier series. By considering the material response in a strain-controlled test with a constant frequency and an amplitude in the domain of SAOS: the output signal expression is:

$$\sigma = \sigma_0 sin\omega_0 t\, cos\delta_0 + \sigma_0 cos\omega_0 t\, sin\delta_0 . \quad \text{Eq. (2.5)}$$

Respectively,

$$\sigma = \frac{\sigma_0}{\gamma_0}\gamma cos\delta_0 + \frac{\sigma_0}{\gamma_0}\frac{\dot{\gamma}}{\omega_0} sin\delta_0 ,$$
$$\sigma = G'\gamma + \frac{G''}{\omega_0}\dot{\gamma} , \quad \text{Eq. (2.6)}$$

where:

$$G' = \frac{\sigma_0}{\gamma_0} cos\delta_0 \; and \; G'' = \frac{\sigma_0}{\gamma_0} sin\delta_0 . \quad \text{Eq. (2.7)}$$

G' is the elasticity modulus (storage modulus) and G'' the viscosity modulus (loss modulus) of the material, while

$$tan\,\delta = \frac{G''}{G'} \quad \text{Eq. (2.8)}$$

and

$$\eta^* = \frac{\sqrt{G'^2 + G''^2}}{\omega_0} \quad \text{Eq. (2.9)}$$

define the loss tangent (equation 2.8) and the complex viscosity (equation 2.9). If the input signal is considered under the complex form $\gamma = \gamma_0 e^{i\omega_0 t}$:

$$G^* = G' + iG'', \quad \text{Eq. (2.10)}$$

$$\eta^* = \eta' - i\eta'', with\ \eta' = \frac{G''}{\omega_0}\ ;\ \eta'' = \frac{G'}{\omega_0}, \quad \text{Eq. (2.11)}$$

where G^* is the dynamic complex modulus, η' is the real viscosity and η'' is the imaginary viscosity.

Dynamic moduli G' (storage modulus) and G'' (loss modulus), together with $\tan\delta$ and η^* are parameters that define the rheological behaviour of a material in a viscometric oscillating motion. For example, when $G' > G''$ the material has a more viscoelastic solid behaviour and when $G'' > G'$ it has a more viscoelastic liquid behaviour. Moreover, an ideally elastic behaviour occurs when $G'' = 0$ hence $\tan\delta = 0$. On the other hand, when $G' = 0$, $\tan\delta$ approaches infinity implying a material with ideally viscous behaviour is obtained. Oscillatory tests are classified into two types namely strain amplitude sweep oscillatory test and frequency sweep oscillatory test. However, to carry out these rheological tests, an adapted rheometer is needed. Hence, different types of rheometers with each having distinct features will be illustrated.

2.5. Which type of rheometer to opt for?

A fundamental instrument for the study of rheological properties is a rheometer. A rheometer is a tool designed to measure the viscosity and elasticity of Newtonian and non-Newtonian materials in a wide range of conditions. There are four types of rheometers as shown in Figure 2.5 [WA19].

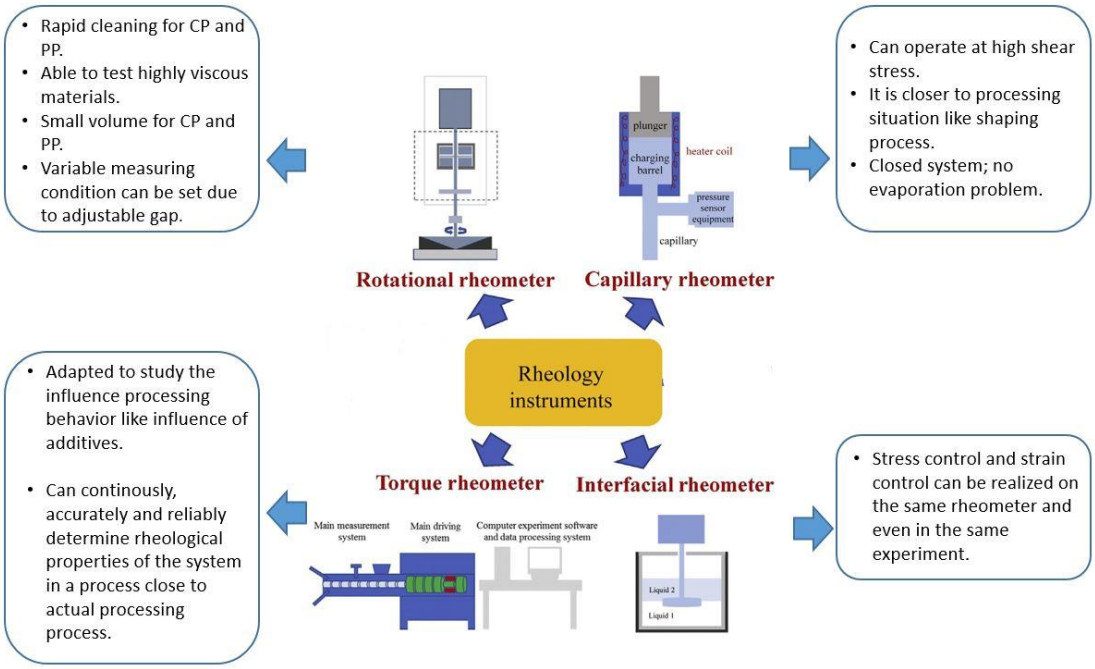

Figure 2.5. Types of rheometers [WA19].

2.5.1. Rotational rheometer

It is the most popular type of rheometer utilised in rheology research. The rheometer has one of the plates fixed while the other one is moving. The sample is placed between the two plates (several geometries are available: plate/plate (PP), cone/plate (CP) and coaxial cylinders). The shear rate is associated with the angular velocity and the stress with the torque. Measurements are carried out in either stress controlled or strain controlled modes. Normally for low to medium viscosity coaxial cylinders geometries are used while plate/plate or cone/plate geometries are employed for highly viscous liquids/paste. This allows the rotational rheometer to cover a large viscosity and shear rate range. The advantages of this instrument are: 1) small sample volumes for CP and PP; 2) variable measuring conditions can be set due to adjustable gap; 3) test highly viscous samples like polymer melts; 4) rapid cleaning for CP and PP. On the other hand, the disadvantages include the price of the instrument and the cleaning difficulties encountered with cylindrical geometry.

2.5.2. Capillary rheometer

The capillary rheometer is used for the measurement of shear viscosity and elasticity of viscous materials at high shear rates. In an electrically heated charging barrel, the sample is heated and the capillary die orifice is placed at the bottom of the barrel. The sample is squeezed out of the capillary die by a rod barrel driven by a motor either at constant or varying speeds – in this way the shear viscosity of the melt can be measured [WA19]. Capillary rheometers are adjustable, accurate and used extensively in the rheological measurement of viscous samples. The flow allows for an easy exchange of samples. Moreover, evaporation is not an issue since the instrument is a closed system. The melting and flowing of the material in the rheometer resemble the processes happening during the shaping step; hence, this rheometer has a high practical value. One of the limitations of the capillary rheometers is the difficulty in measuring fluid with low viscosity less than 1 Pa·s.

2.5.3. Torque rheometer

A torque rheometer has proven itself to be a valuable tool for studying thermal stability, shear stability, flow, and plasticising behaviour of materials. Typically, analyses by a torque rheometer include the influence of processing behaviour, influence of additives, thermal sensitivity of material, shear sensitivity, compounding behaviour, etc. [ME20]. Torque rheometers are primarily small extruders that utilise a motor to measure the torque on the rotors. It is linked to a software that follows the drive speed, pressure, temperature and process torque. It can determine the rheological properties of analysed samples reliably, accurately and continuously [WA19]. A computer automates the torque rheometer; consequently, it can replicate rheological behaviour of the material during the actual

processing conditions. The corresponding software accomplishes data acquisition, control, and processing of experimental data. Furthermore, the software has built-in functions to process data that traditional torque rheometers are not equipped with such as linear accelerated measurement of the shear sensitivity of material. [HE20] [WA19]. However, torque rheometers provide only a relative measure of viscosity through correlation with torque.

2.5.4. Interfacial rheometer

An interfacial rheometer is a test instrument for measuring the shear rheological properties of a liquid/liquid or liquid/gas interfacial film, which belongs to 2D space rheology. It can be used for the processing and treatment of emulsion, the deformation and combination of emulsion drops, the microstructure of food raw materials and other consumer products, the interface transfer function, and other research fields [NA98] [TA16]. The magnetised probe is moved at air-water or oil-water interface using a magnetic field created by a Helmholtz coil and the probe movement is recorded. Strain control and Stress control can be carried out on the same rheometer and even in the same experiment. Normally a bicone geometry is used for interfacial rheometers where the cone is located directly at the liquid/liquid or liquid/air interface. In addition, the interface flow is coupled to bulk phase flow. Furthermore, the advantages of using a bicone are: 1) low and high interfacial viscosities measurable; 2) robust well-defined measuring system; 3) use of large gap cylinder analogy. The disadvantage is that a large sample volume required [WA19].

Different types of rheometers have been presented with each having specific purposes along with their advantages and disadvantages. Both the torque and the capillary rheometers are suited for shaping processes as they provide data on melt flow and viscosity of material. The rotational rheometer investigates the polymer's viscoelastic properties. The last rheometer considered was the interfacial rheometer that measures the flow of matter at the interface between two fluids. However, since our goal was to follow in real time the rheological and structural changes occurring during polymerisation reaction. A rheometer that coupled two analytical techniques (FTIR spectroscopy and dynamic rheometry) in one instrument to form the Thermo Scientific™ Rheonaut Module with the Thermo Scientific™ HAAKE™ MARS™ Rheometer was more suited for this project.

2.5.5. Rotational rheometer coupled with FTIR spectrometer

The rotational rheometer (Mars III, Thermo Scientific™ HAAKE™ MARS™ Rheometer) has a Rheonaut module with a side port to equip a standard FTIR spectrometer (Figure 2.6). The Rheonaut module can accommodate numerous standard FTIR spectrometers such as the Thermo Scientific™ Nicolet IS10™. The Rheonaut was developed to investigate the

rheological and structural changes occurring at real time. The advantages of this setup are: 1) same sample history and composition; 2) time saving since tests carried out at the same time; 3) tests carried out by both methods have same conditions e.g. temperature, pressure, etc; 4) the FTIR data can be efficiently correlated to the rheological data. Furthermore, the rheonaut module possesses two different temperature control units *i.e*. a Peltier temperature unit (0-100 °C) and an electric unit with a range of temperatures varying from room temperature to 400 °C. This measuring unit is devised for using either a cone-plate or a plate-plate measuring geometry.

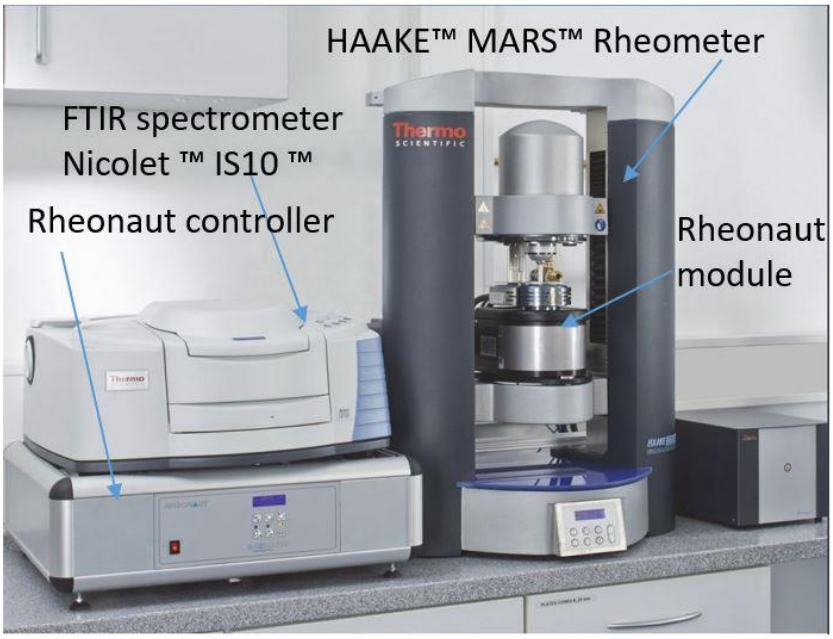

Figure 2.6. Setup with HAAKE MARS rheometer, Rheonaut module and FTIR spectrometer.

Cone-plate geometry (CP)

Normally, CP is appropriate for a variety of fluids but their applicability to dispersion is restricted to a particular maximum particle size. It is advised that a cone angle of $\alpha = 1°$ is used since cones with an angle greater than 4° are regarded to be sub-standard. Moreover, it is necessary to correctly load the CP system with the right amount of sample as shown in Figure 2.7.

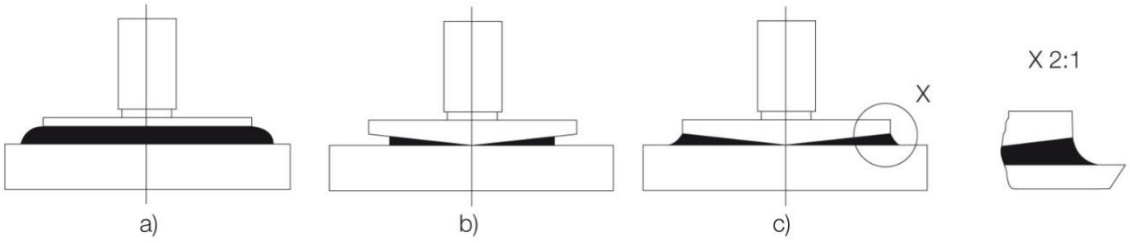

Figure 2.7. Filling of a cone/plate measuring system after gap setting: a) overfilled, b) underfilled, c) correct amount [PA15].

The advantages of the CP geometry are: 1) small quantity of sample is needed; 2) rapid temperature adjustment and easy to clean; 3) across the entire conical gap, there are uniform shear conditions. One limitation of the CP geometry is, that the sample migrates out at the edge the gap as well as drying of sample may happen [PA15].

Plate-plate geometry (PP)

PP system is recommended for testing gels, soft solids, highly viscous polymer melts or pastes. The gap widths should be from 0.5 to 1 mm. Solvent trap or special hood can be utilised to prevent evaporation of solvents. The advantages of the PP geometry are: 1) rather small amount of sample is needed; 2) easy and rapid cleaning; 3) possibility to test highly viscous materials. On the other hand, some limitations of the PP geometry are: 1) sample migrated out of at the edge of the gap as well as drying of sample may happen; 2) not a uniform sample temperature across the gap if the temperature equilibrium time is too short; 3) shear rate at the margin of the plate is higher than at the centre of the geometry [PA15].

2.6. Vibrational spectroscopies

Vibrational spectroscopies are widely used optical characterisation techniques and used in many scientific and industrial fields. For several years now, they have been enjoying great success, due to the numerous technological innovations, which make them more and more efficient and usable on a wide range of materials crystals and ceramics, polymers, glasses, molecules (organic and inorganic), in various forms (liquid, gas or solid). Vibrational spectroscopy measures the vibrational energy in a compound where every single chemical bond coincides to a specific vibrational energy that can be regarded as a unique fingerprint, useful to identify compound structures, by contrasting it with the fingerprints of known compounds.

2.6.1. Principle of infrared absorption spectroscopy

IR spectroscopies are based on the absorption of electromagnetic radiation by the polar modes of vibration of matter (gases, liquids or solids) due to the electric dipolar interaction. When subjected to infrared radiation, organic molecules may absorb infrared radiation and transform it into molecular vibrations. The molecular vibrations within a molecule are the consequence of the change in the dipole moment of the molecule implying the vibrational response is IR active [MO06]. The electromagnetic radiation comprises an oscillating magnetic field and an oscillating electrical field perpendicular to each other. When IR radiation passes through a molecule, the radiation will only be absorbed if the frequency of the radiation corresponds to the vibrational frequency of the molecule. In absorption spectroscopy, Beer-Lambert law is used to determine the

relationship between the intensities of the incident and transmitted IR radiation and the analyte concentration. The Beer-Lambert law is expressed as [MA20]:

$$A = \log\left(\frac{I_0}{I_t}\right) = \varepsilon . l . c \qquad \text{Eq. (2.12)}$$

I_0 and I_t are the incident and transmitted intensity respectively. The constant ε represents the molar absorptivity ($L \cdot mol^{-1} \cdot cm^{-1}$). c represents the concentration of the sample solution expressed in $mol \cdot L^{-1}$ and l the length of the light path. As abovementioned, in IR spectroscopy, a change in dipole moment is required for the vibration to be IR active. The dipole moment is calculated by equation 2.13, where μ is the dipole moment and Q is the vibrational amplitude.

$$\delta\mu = \left(\frac{\partial\mu}{\partial Q}\right)_0 \delta Q \neq 0 \qquad \text{Eq. (2.13)}$$

2.6.2. Attenuated Total Reflectance-IR spectroscopy

Based upon the total internal reflection phenomena, Harrik [HA60] and Fahrenfort [FA89] introduced Attenuated Total Reflectance (ATR) spectroscopy. IR spectra are acquired when the material sample is in contact with an internal reflection element (IRE). The incident beam directed onto the edge of the IRE, reflected through the IRE (all the lights are reflected off), and the reflected beam directed towards the detector. In most cases, the ATR crystal has a higher refractive index (n_1) as compared to the sample (n_2). Another important characteristic is the incidence angle θ that can be calculated from the refractive indexes of the sample (n_2) and the IRE (n_1) as shown in equation 2.14:

$$\theta_c = arcsin\left(\frac{n_2}{n_1}\right) \qquad \text{Eq. (2.14)}$$

In addition, the penetration depth (d_p) of the IR beam is another key parameter in ATR-FTIR spectroscopy. It determines how much of the sample is actually analysed. The depth of the infrared beam passing through the sample is established by the expression:

$$d_p = \frac{\lambda}{2\pi n_1 \sqrt{\sin^2\theta - (\frac{n_2}{n_1})^2}}, \qquad \text{Eq. (2.15)}$$

where θ is the angle of incidence and λ is wavelength [GR83]. The penetration depth is influenced by the angle of incidence, refractive indices, and the wavelength.

The dimensions of the crystals will determine the volume of the sample needed and guarantee that the sample is covering the whole IRE, enabling effective penetration of the incident beam on the sample [GL13] [CA20]. One drawback of this technique is that the IRE

has to stay clean to make sure that no cross-pollution occurs between samples. Moreover, damages such as scratches on the surface of the IRE, can impact the sample-IRE contact.

As mentioned previously, at the IRCER, the ATR accessory is coupled with a rotational rheometer (Mars III, Thermo Scientific™ HAAKE™ MARS™ Rheometer). The spectrometer (FTIR) is a “Nicolet ™ IS ™ 10” type, supplied by ThermoFisher Scientific and it is connected to the Rheonaut compartment of the rheometer as shown in Figure 2.8. Normally, the ATR is position at the centre of the lower surface of the plate-plate configuration during the experiments.

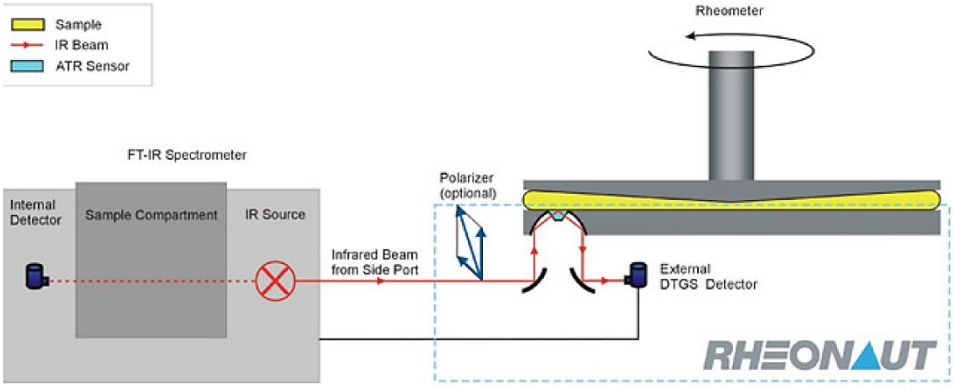

Figure 2.8. Coupling an ATR-FTIR spectrometer with a rheometer.

Moreover, it operates in the mid-infrared spectral range 400 to 4000 cm^{-1} where all the fundamental absorption bands of a sample are typically found. The laser beam passes through a diamond with 1 mm^2 area situated on the lower part of the geometry of the rheometer. Before launching any data acquisition on the sample, a background IR spectrum is required in order to remove any parasite absorption like O-H bond signature from H_2O vapour or C-O band signature from CO_2 vapour. The sample is deposited uniformly on the diamond crystal. From a practical point of view, the sample must match the entire contact surface of the crystal in order to be free from the contribution of air and thus obtain better results. Furthermore, the Thermo Scientific™ HAAKE™ Rheowin™ software enables launching the spectrometer software to ensure a simultaneous start of the rheological and spectroscopic data acquisition. In addition, the lower plate of the rheometer can be moved *via* the software control, thus allowing for the data acquisition along the radius of the geometry. For all experiments, IR spectra were recorded with the following conditions: number of scans 8 and a resolution of 4 cm^{-1}. Depending on the experiments, the FTIR has acquired data points for every 30 s or 17 s.

2.7. Raman scattering process

In 1928, C.V Raman together with K.S Krishnan published the first paper on Raman spectroscopy [RA28]. In 1930, Raman received the Noble Prize in Physics for his work on the scattering of light and the discovery of the effect was named after him. Raman spectroscopy is a scattering technique. Raman spectroscopy uses a monochromatic laser beam to irradiate the sample and it is the inelastic scattered radiation from the matter which is analysed. The light interacts with the molecule and distorts (polarizes) the electronic cloud round the nuclei to form a short-lived state called virtual state. Generally, the virtual state is not stable and the photon is re-emitted nearly instantaneously as scattered light. Most of the time, the energy of the molecule is unaltered after its interaction with the photon indicating that the wavelength and the energy of the scattered photon are equal to those of the incident photon. This is called Rayleigh scattering or elastic scattering where the energy of the scattered particle is conserved. However, a small amount of light (approximately 0.0000001%) is scattered at different wavelengths and this process is called inelastic scattering or Raman scattering. In quantum interpretation, the Raman effect is described as inelastic scattering of a photon off of a molecular bond [BU16]. Figure 2.9 illustrates the Jablonski diagram with three potential outcomes when the incident photon excites the molecule into a virtual energy state [CH20].

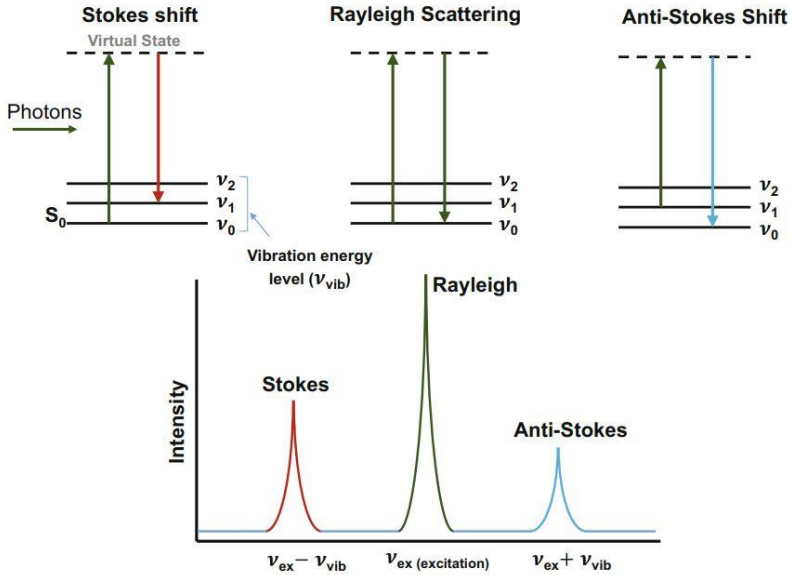

Figure 2.9. Rayleigh scattering, Stokes Raman and anti-Stokes Raman scattering [CH20].

Rayleigh scattering occurs when the molecule relaxes back to its initial ground state and releases a photon of equal energy to that of the incident photon. In the second case, Stokes shifted Raman scattering occurs when the molecule relaxes to a phonon state and emits a phonon with less energy than the incident photon. The third possible result is the

Anti-Stokes Raman where the molecule is already in an excited phonon state and is excited to higher virtual state. When it relaxes back down to the ground state, it emits a photon with higher energy than the incident photon. Most Raman measurements are achieved taking into account only the Stokes shifted light. This is because most molecules are found in the ground state at room temperature and there is a low probability that a phonon will be Anti-stokes scattered [LA17]. [MO06]. The intensity of the Raman scattered radiation I_R is given by:

$$I_R \propto \nu^4 I_0 N \left(\frac{\partial \alpha}{\partial Q}\right)^2, \quad \text{Eq. (2.16)}$$

where I_0 is the incident laser intensity, N is the number of scattering molecules in a given state, ν is the frequency of the exciting laser, α is the polarizability of the molecules, and Q is the vibrational amplitude. Only molecular vibrations which cause a change in polarizability are Raman active [LA17]. Hence, the change in polarizability with respect to a change in vibrational amplitude where, Q, is greater than zero is expressed as:

$$\left(\frac{\partial \alpha}{\partial Q}\right) \neq 0. \quad \text{Eq. (2.17)}$$

2.8. Contribution of Raman spectroscopy to the platform

Raman spectroscopy is an analytical technique where scattered light is used to measure the vibrational energy modes of a sample. Some advantages of Raman spectroscopy are: i) easy to implement as it does not require preparation of samples; ii) it is regarded as a non-destructive technique as the low power of the excitation laser does not damage the sample; iii) *In-situ* analysis of compounds that are in hostile or aqueous environments [SI20]. However, in our case by including a Raman spectrometer to the platform, we will combine two vibrational techniques that complement each other. It is known that infrared (IR) absorption and Raman scattering spectroscopy provide complementary information of molecular vibrations: the former is active for anti-symmetric vibrations that alter the dipole moment, while the latter for symmetric vibrations that alter the polarizability. IR absorption spectroscopy, which is active for polar bonds such as O–H or N–H, is often used for identification of functional groups of molecules, while Raman scattering spectroscopy, active for bonds such as C=C, S–S, or C–S4, is used for identification of skeletal structures. Moreover, by combining the Raman spectrometer equipped with a lens to the existing Rheo-FTIR setup complementary information in terms of spatial resolution will be obtained. The ATR provide a spatial resolution in micrometre while the spatial resolution for the Raman spectrometer is measured in millimetre. Furthermore, the information obtained from ATR provided only a surface information that is not representative of what is happening within the

volume of the sample. Hence, the Raman spectrometer associated to a lens will lead to a larger depth penetration to the existing Rheo-FTIR setup.

In this project, Raman spectrometer will be equipped either with a lens or with an immersion probe. Figure 2.10 represents a laser beam profile of a lens with a focal distance of 75 mm.

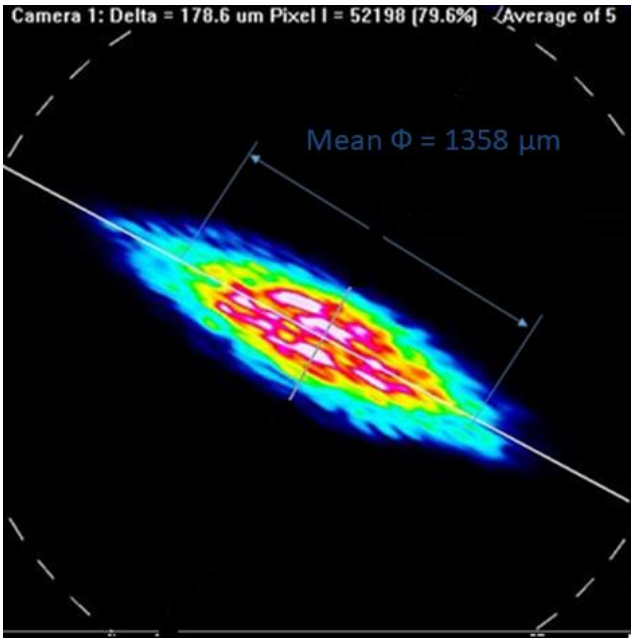

Figure 2.10. Laser beam profile of a lens with a 75 mm focal distance.

The dimension of the laser that is in an ellipsoid form can be calculated by using the following formulae:

$$d \approx \frac{4\lambda f}{\pi \phi} \qquad \text{Eq. (2.18)}$$

$$L \approx \frac{16\lambda n f^2}{\pi \phi^2}, \qquad \text{Eq. (2.19)}$$

where f is the focal distance (75 mm), λ the wavelength of laser (785 nm), d is the diameter of the laser beam at the outlet (spot diameter) and Φ is the input beam diameter (1358 µm). The diameter of the laser varies from a maximum to a minimum value depending on whether we consider the diameter to be in horizontal or vertical position. For the theoretical calculation of the dimension of the waist, the mean of the two diameters is used. Therefore, the laser dimension of the lens with a focal distance of 75 mm is $d \approx 0.055$ mm and $L \approx 12.2$ mm.

On the other hand, the dimension waist of a Raman microscope objective can be calculated by applying the following formulae:

$$d \approx \frac{1.22\lambda}{N.A} \qquad \text{Eq. (2.20)}$$

$$L \approx \frac{4n\lambda}{N.A^2}, \qquad \text{Eq. (2.21)}$$

where $N.A$ is the numerical aperture, λ is the wavelength of the laser. Given that the numerical aperture ($N.A$) = 0.9, the wavelength of the laser is 785 nm. Thus, the theoretical waist of the microscope objective is $d \approx$ 1.06 µm and $L \approx$ 3.87 µm.

The microscope objective has a penetration depth around 3.87 µm while the lens has a penetration depth in between $L \approx$ 12.2 mm. Therefore demonstrating that a greater volume will be probed by using the Raman spectrometer associated with a lens than a microscope objective (Figure 2.11). Therefore, the integration of the Raman spectrometer to the platform can only be beneficial as we exploit the complementary nature of the two vibrational techniques.

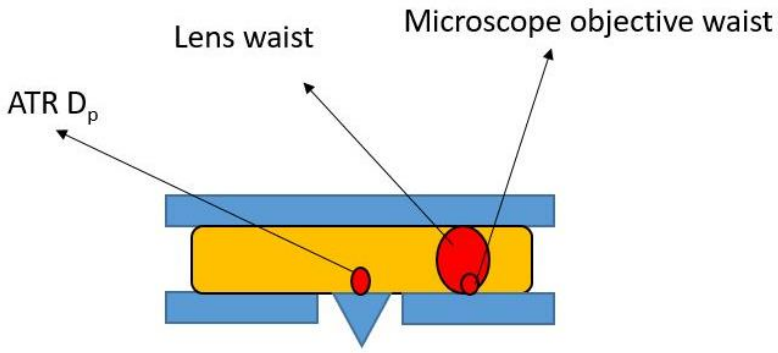

Figure 2.11. Schema of the Rheo-Raman FTIR set up with a representation of the microscope objective waist, lens waist and the penetration depth of the infrared beam.

2.9. Experimental conditions used during the in-situ analysis

As aforementioned, the Raman spectrometer is coupled with the Rheo-FTIR setup forming the newly devised setup known as the Rheo-Raman-FTIR setup as shown in the Figure 2.12.

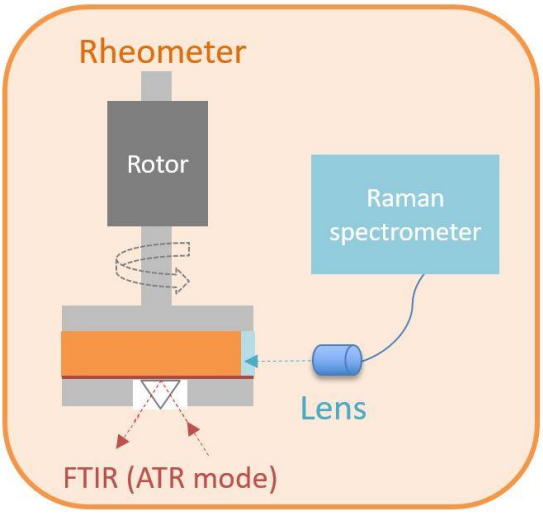

Figure 2.12. Rheo-Raman-FTIR setup.

The Raman measurements are carried out by using a RXN1 spectrometer (Kaiser optical System) with a laser excitation wavelength of 785 nm. The Rheo-Raman-IR setup uses a lens with a focal distance of 100 mm to perform measurements. The position of the lens can be adjusted accordingly with the help of a lab-made support on which the Raman head resides. The support allows the lens' position to be modified both horizontally and vertically. The rheometer is set with a gap of 0.6 mm through which the laser beam passes as demonstrated in Figure 2.12. Before each measurement, the signal is optimised on the stretching vibration of C=C from toluene at 1605 cm^{-1}. Signal optimization is carried out to obtain peaks with high intensity. Raman spectra acquisitions are carried out with an exposure time of 10 s and an interval time of 15 s. These experimental conditions are selected as they represent a good compromise between a good signal and collection of enough Raman spectra during the polymerisation reaction.

Concerning the rotational rheometer (Rheonaut section), a PP geometry of 35 mm is used during the experiment with a gap set at 0.6 mm. The rheometer is initialised in terms of gap and inertia before the start of the experiment. The optimisation of this setup will be presented in more detail in chapter 3. Two rheological tests (Table 2.2) are performed on the setup namely a time dependent oscillation test and a steady states test. As mentioned before, the IR spectra were recorded with a resolution of 4 cm^{-1} and a number of scans of 8.

Table 2.2. Parameters used during rheological tests.

Parameters	Gap (cm)	Frequency (Hz)	Strain (-)	Shear rate (s^{-1})	Temperature (°C)
Oscillation test	0.6	1 or 35	0.5	x	25
Steady states test	0.6	x	x	4.5 or 35	25

Moreover, the polymerisation reactions carried out in a RBF use the same Raman spectrometer RXN1 (Kaiser optical System) that is utilised on the Rheo-FTIR-Raman setup. The only difference is that an immersion probe replaced the lens with a focal distance of 100 mm. The immersion probe has an immersion length of 15.3 cm and a diameter of 0.64 cm. The tip of the immersion probe can withstand a temperature range of -30 to +450 °C and a pressure up to 20685 kPa. The Raman probe is immersed in a 25 mL solution in the RBF as presented in Figure 2.13. Since the Raman probe is in direct contact with the reagents, a better signal is obtained compared to the Raman lens with a focal distance of 100 mm. Raman spectra are acquired with an exposure time of 2 s and a current interval time of 10 s. The magnetic stirrer is set at 4.5 Hz during the polymerisation reaction. This frequency is selected in order to match approximately the shear rate on the rheometer. The magnetic stirrer is stirred continuously until it is trapped upon the formation of the gel. Table 2.3 shows the parameters used when using the Raman spectrometer.

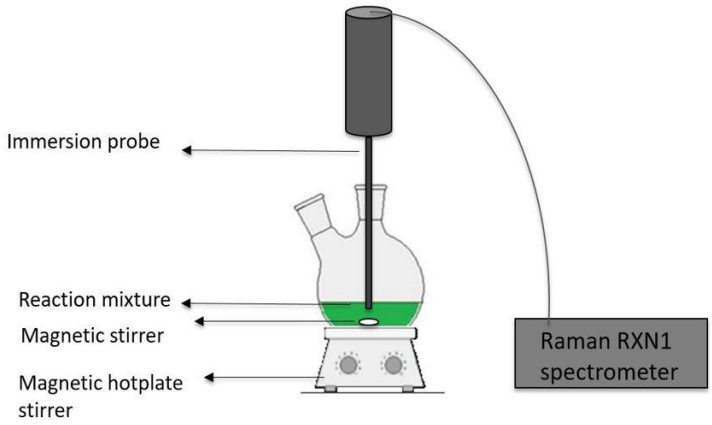

Figure 2.13. Experimental set up of immersion probe in RBF.

Table 2.3. Parameters used for acquisition of Raman spectra.

Reactions taking place:	Spectrometer	Wavelength	Optics	Exposure time	Interval time
Rheo-Raman FTIR setup	RXN1	785 nm	Lens 100 mm	10 s	15 s
Round bottom flask (RBF)			Immersion probe	2 s	10 s

2.10. Vibrational characterisation of reagents

The IR and Raman spectra of the two monomers (TA and BDSB), of the solvent toluene and of Karstedt's catalyst were determined and are presented in Figure 2.14 to Figure 2.17. Indeed, it is important to identify the characteristic bands that will allow for the monitoring of the kinetics of the polymerisation reaction. The IR spectra are recorded in ATR mode with the following conditions: number of scans 8 and a resolution of 2 cm^{-1}. The resolution was set at 2 cm^{-1} solely for the reagents to obtain sharper spectra. While for Raman acquisitions, each reagent was placed in an individual test tube and Raman spectra acquisitions were carried out with an exposure time of 10 s and an interval of 15 s.

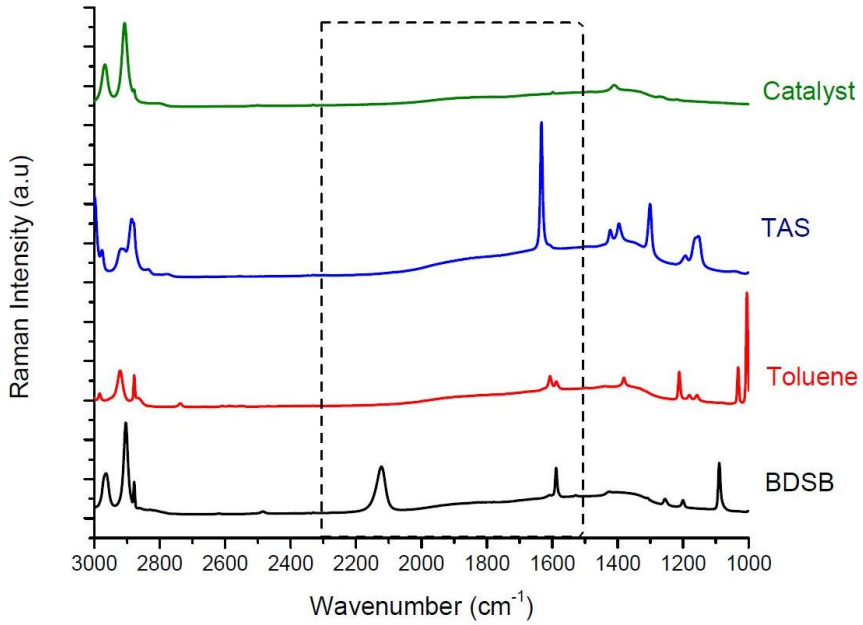

Figure 2.14. Raman spectra of Karstedt's catalyst, TAS, toluene and BDSB.

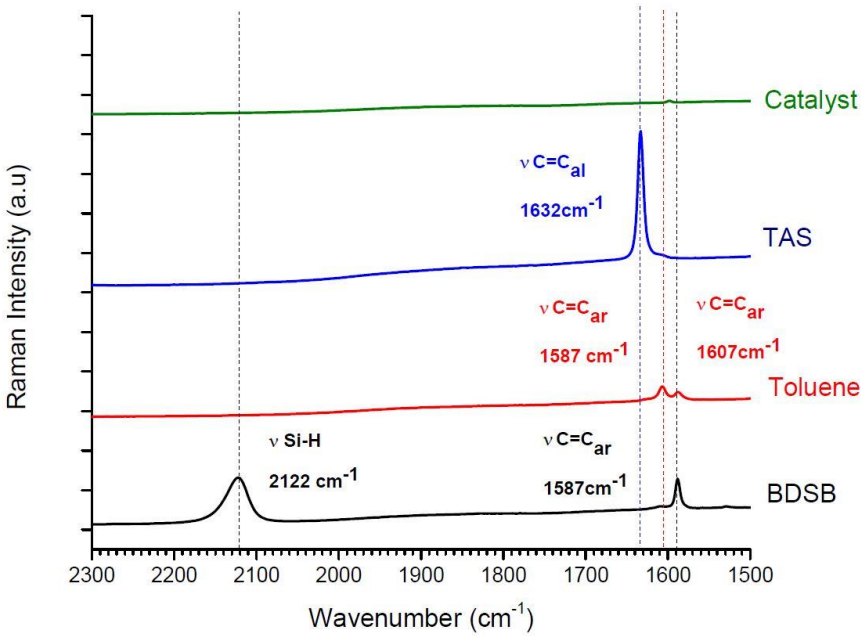

Figure 2.15. Raman spectra of Karstedt's catalyst, TAS, toluene and BDSB in a wavenumber range of 2300 to 1500 cm^{-1}.

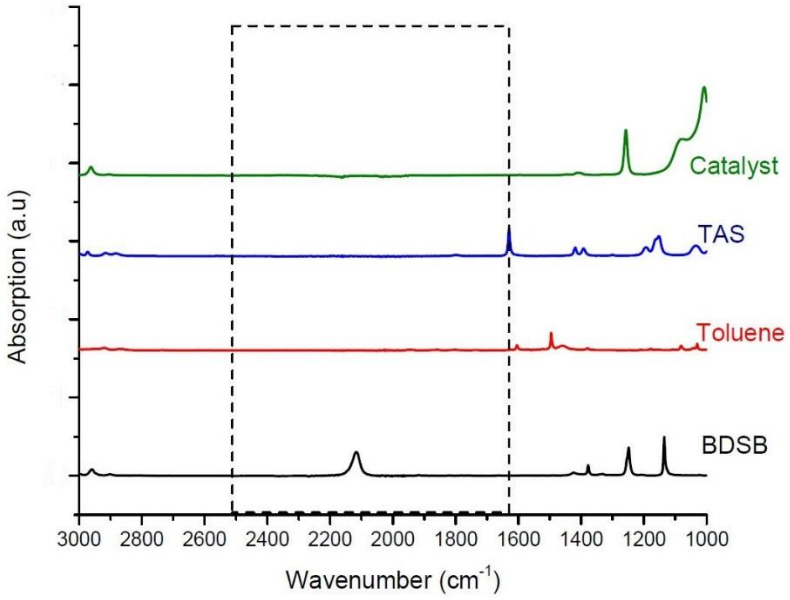

Figure 2.16. IR spectra of Karstedt's catalyst, TAS, toluene and BDSB.

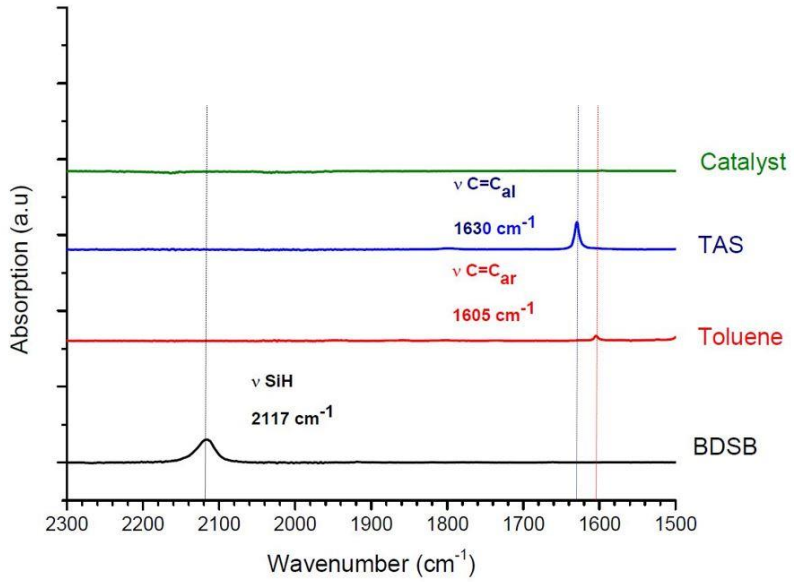

Figure 2.17. IR spectra of Karstedt's catalyst, TAS, toluene and BDSB in a wavenumber range of 2300 to 1500 cm^{-1}.

The wavenumber range from 1500 to 2300 cm^{-1} is of particular interest as characteristic bands of the monomers are found in this region and they did not overlap each other. It is noticed that the stretching vibration of C=C from TAS is present in both IR (1630 cm^{-1}) and Raman spectroscopy (1632 cm^{-1}). In parallel, it is observed that the stretching vibration of Si-H is present in both IR (2117 cm^{-1}) and Raman spectroscopy (2122 cm^{-1}) while the stretching vibration of aromatic C=C (1587 cm^{-1}) is present only in Raman spectroscopy for BDSB. This is linked to the symmetry of the molecule. Hence, a DFT investigation was considered since the stretching vibration of C=C$_{ar}$ (1587 cm^{-1}) was active in Raman and not in FTIR. The DFT results are discussed at section 2.12. For the Raman spectrum of toluene, a stretching vibration band is observed at 1607 cm^{-1}, while in FTIR it is observed at 1605 cm^{-1}. The Karstedt's catalyst shows a very weak band at around 1600 cm^{-1} in the Raman spectrum. The monitoring of the polymerisation reaction can either be carried out by following the evolution of the stretching vibration of Si-H in BDSB or the stretching vibration of C=C from TAS as both bands are consumed during the polymerization reaction. In order to better interpret the Raman and FTIR spectra of the reagents used during the experiments, the Tables 2.4 to 2.7 show the most common peaks of those reagents.

Table 2.4. Assignments of BDSB bands [BE13], [MC85], [SM60], [SM53].

IR (cm^{-1})	Raman (cm^{-1})	Assignments
3080	3031	C-H stretch
2960	2967	C-H stretch
2896	2904	C-H stretch
2117	2122	Si-H stretch
	1587	C=C stretch
1427	1431	C-H bending
1133		Si-C stretch

Table 2.5. Assignments of TAS bands [DA73].

IR (cm^{-1})	Raman (cm^{-1})	Assignments
3085	3083	Vinyl CH_2 stretch
3002	2998	Vinyl CH stretch
2980	2977	Vinyl CH_2 stretch
2907	2908	CH_2 stretch
2886	2886	CH_2 stretch
1630	1632	C=C stretch
1420	1421	Methylene scissors
1393	1395	Vinyl scissors
1300	1298	Vinyl CH rock
1192	1191	Methylene wag
1038	1040	Methylene twist

Table 2.6. Assignments of catalyst bands [BEL13], [SM60].

IR (cm^{-1})	Raman (cm^{-1})	Assignments
2964	2968	C-H stretch
2904	2906	C-H stretch
1409	1406	C-H deformation
1257	1265	Si-C stretch
1004		Si-O stretch

Table 2.7. Assignments of toluene bands [LA17].

IR (cm^{-1})	Raman (cm^{-1})	Assignments
3068,3028	3057	C-H stretch
2921		C-H stretch
1943,1858,1803,1735		Ring C-H wag
1605	1607	C=C stretch
1496		Ring semi stretch
1461		CH_3 bend
1379	1381	CH_3 bend

2.11. Post processing of data

After obtaining the Raman and FTIR spectra, the Renishaw's Windows®-based Raman Environment (WiRE™) is used for post processing and basic analyses. A common post processing technique is selected for Raman and FTIR data. Figure 2.18 shows a curve fitting applied to a Raman set of data. The data obtained are truncated from 1500 to 2300 cm^{-1} followed by a linear baseline subtraction.

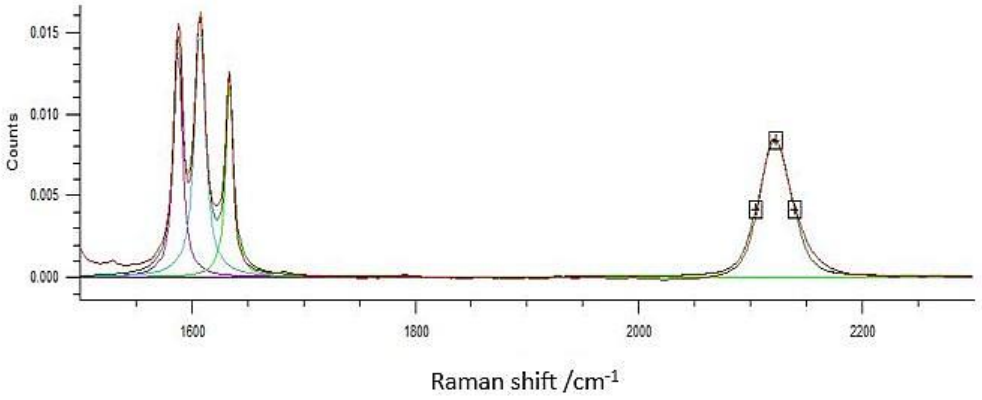

Figure 2.18. Curve fitting on Raman spectrum.

A triplet representing the stretching vibration of C=C of BDSB at 1587 cm^{-1}, C=C of toluene at 1607 cm^{-1} and the C=C of TAS at 1632 cm^{-1} is observed. At higher frequencies, we find the stretching vibration of Si-H at 2122 cm^{-1}. During the fit, frequencies of the function were fixed but limits were set on the amplitude of the curve. No constraint was applied on the Full Width at Half Maximum (FWHM). In literature, for FTIR, the amplitude of the peak is used for data processing. In this work, all the data was fitted by using a pseudo Voight function. Consequently, the intensity of the applied curve function was used for the analysis of the data. For both Raman and FTIR, the stretching vibration band of C=C in TAS was normalised by the stretching vibration of the band $C{=}C_{ar}$ of toluene since the toluene band remained unchanged during the reaction. Only the alkene conversion was calculated since in FTIR the amplitude of the Si-H band is influenced by the vibrations from the diamond crystal. Therefore, the alkene conversion versus time can be calculated given the normalised peak intensity function at t = 0, and at a time t, denoted N_0 and N_t, respectively. In this way, the conversion can be expressed as:

$$\tau\,(t) = \frac{N_0 - N_t}{N_0}. \qquad \text{Eq. (2.22)}$$

2.12. Density function theory

Density function theory is a computational quantum mechanics modelling method used in chemistry, physics and material science to investigate the electronic structure of solid, atoms and molecule [MO14]. A vibrational analysis (FTIR and Raman) of BDSB molecule has been performed. However, by analysing the obtained spectra, we observe that there is an active mode in Raman spectrum that seems to be absent in FTIR spectrum as shown in Figure 2.19. This difference between the two vibrational techniques is accounted by the symmetry of the BDSB molecules.

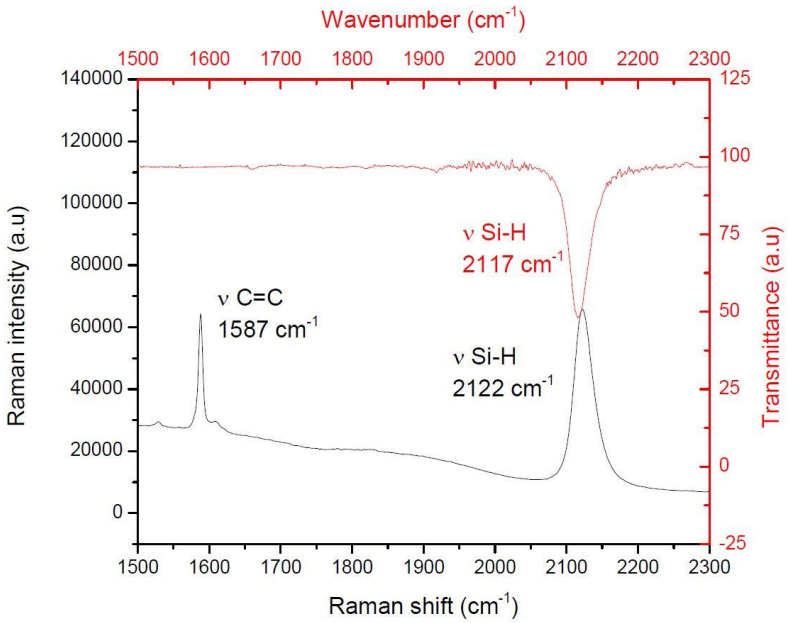

Figure 2.19. FTIR and Raman spectra of BDSB molecule.

The molecule BDSB has an axis of order 2 (C_2). Moreover, the BDSB molecule has a plane of symmetry (σ_h), that is orthogonal to the C_2 axis. Therefore, since BDSB molecule has a C_2 axis as well as a plane of symmetry (σ_h), subsequently it will have a centre of inversion as shown in Figure 2.20. The molecule BDSB has a character table of type C_{2h} (Table 2.8). Based on the character table, active modes in Raman are inactive in FTIR, hence verifying the principle of mutual exclusion.

Table 2.8. Character table C_{2h} [AT70].

C_{2h}	E	C_2	i	σ_h		
A_g	1	1	1	1	R_Z	X^2, Y^2, Z^2, XY
B_g	1	-1	1	-1	R_x, R_y	XZ, YZ
A_u	1	1	-1	-1	Z	
B_u	1	-1	-1	1	X, Y	

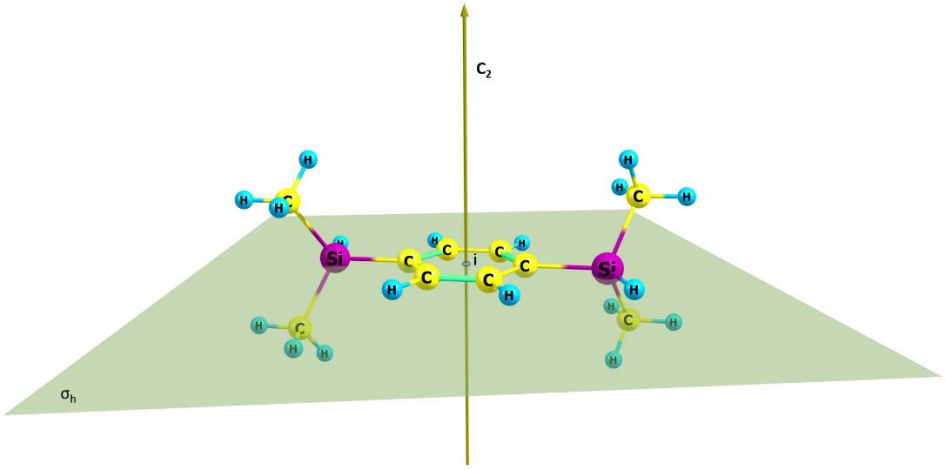

Figure 2.20. BDSB molecule constructed in Gaussview software.

DFT calculation has been carried out at IRCER to demonstrate the consequence of a centre of inversion on the vibrations modes of molecules. The GAUSSIAN version 03 and Gaussview software were used to carry out the DFT calculations. They were performed on optimised geometries to determine the vibrational frequencies and IR and Raman intensities. To follow the evolution of the stretching vibration of $C=C_{ar}$ function, we started from the basic molecule of benzene which is the skeleton of the BDSB molecule. The molecule is turned into an asymmetric molecule by adding a CH_3 function. By adding a second CH_3 function, we reinstituted the symmetry of the molecule. Finally the CH_3 functions are replaced by $[SiH(CH_3)_2]_2$ function. In this way, we put in evidence the evolution of the stretching vibration of $C=C_{ar}$ frequencies in both Raman and IR spectra. Figure 2.21 shows the construction of the benzene molecule up to BDSB molecule. Xylene is close from BDSB molecule in terms of symmetry, however due to its difference in weight ($[SiH(CH_3)_2]_2$), their frequencies will be different.

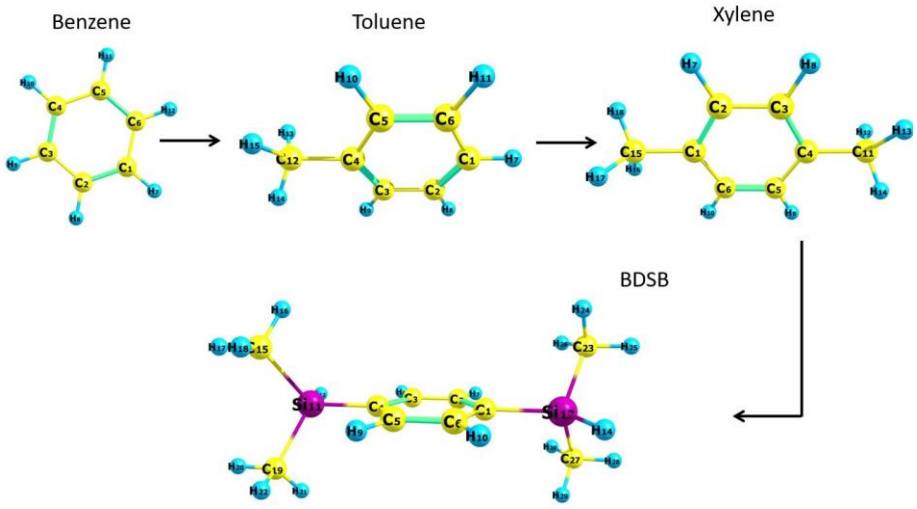

Figure 2.21. Different molecules computed by DFT.

Table 2.9 and Table 2.10 report the different frequencies of the vibrational modes obtained for Raman and FTIR by DFT calculation of benzene, toluene, xylene and BDSB in the region 1500 cm^{-1} to 2300 cm^{-1}. In FTIR DFT the stretching vibration of $C=C_{ar}$ in benzene was identified at around 1539 cm^{-1} while in Raman DFT it was reported at 1626 cm^{-1}. By knowing the initial frequency of $C=C_{ar}$, we could follow its evolution in the other molecules. Table 2.12 reports the frequency evolution of the $C=C_{ar}$ in each molecule and the stretching vibration of $C=C_{ar}$ could be distinguished from the rest as it was marked in green colour. However, for both Raman and FTIR, the initial frequency value of $C=C_{ar}$ reported in benzene, was different in toluene, xylene and BDSB molecules. Therefore, to successfully follow the evolution of the $C=C_{ar}$, we had to consider the vector displacements of the $C=C_{ar}$ to identify its frequency in each molecule. In FTIR DFT calculation of BDSB molecule showed a very weak intensity of the $C=C_{ar}$ frequency at 1564 cm^{-1} while in Raman DFT a strong intensity is reported for $C=C_{ar}$ at a frequency of 1626 cm^{-1}. The intensity of the frequency of $C=C_{ar}$ in FTIR DFT was of 4 order of magnitude lower in comparison to the Raman DFT, hence it was regarded as negligible. The strong intensity of Si-H band was reported in both FTIR and Raman DFT at around 2134 cm^{-1}. Consequently, the DFT results of the BDSB molecules is in accordance with the Raman and FTIR experimental results.

Table 2.9. FTIR DFT calculation of benzene, toluene, xylene and BDSB molecules.

FTIR calculations of vibrational modes from 1500 cm^{-1} to 2300 cm^{-1}				
Benzene calculated (cm^{-1})	Toluene calculated (cm^{-1})	Xylene calculated (cm^{-1})	BDSB calculated (cm^{-1})	BDSB experimental (cm^{-1})
	 1503	 1551	 1524	
	 1550	 1558	 1535	
 1539	 1551	 1564	 1543	Not observed
	 1554			1662 Very small
	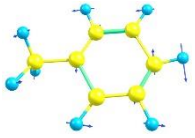 1620			1918 Very small
	 1636		 2133	2113 Very strong

Table 2.10. Raman DFT calculation of benzene, toluene, xylene and BDSB molecules.

Raman calculations of vibrational modes from 1500 cm^{-1} to 2300 cm^{-1}				
Benzene calculated (cm^{-1})	Toluene calculated (cm^{-1})	Xylene calculated (cm^{-1})	BDSB calculated (cm^{-1})	BDSB experimental (cm^{-1})
	 1503	 1543	 1523	
	 1551	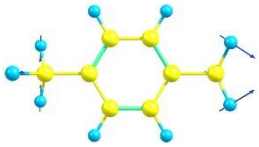 1550	 1530	1530 Very small
	 1554	-	 1535	
	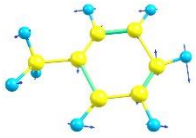 1620	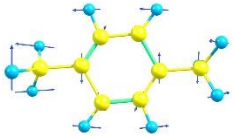 1612	 1559	1608 Very small
 1626	 1636	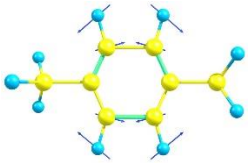 1644	 1611	1587 Very strong
			 2134	2123 Very strong

Table 2.11. FTIR and Raman evolution of the C=C_{ar} *via* the different molecules.

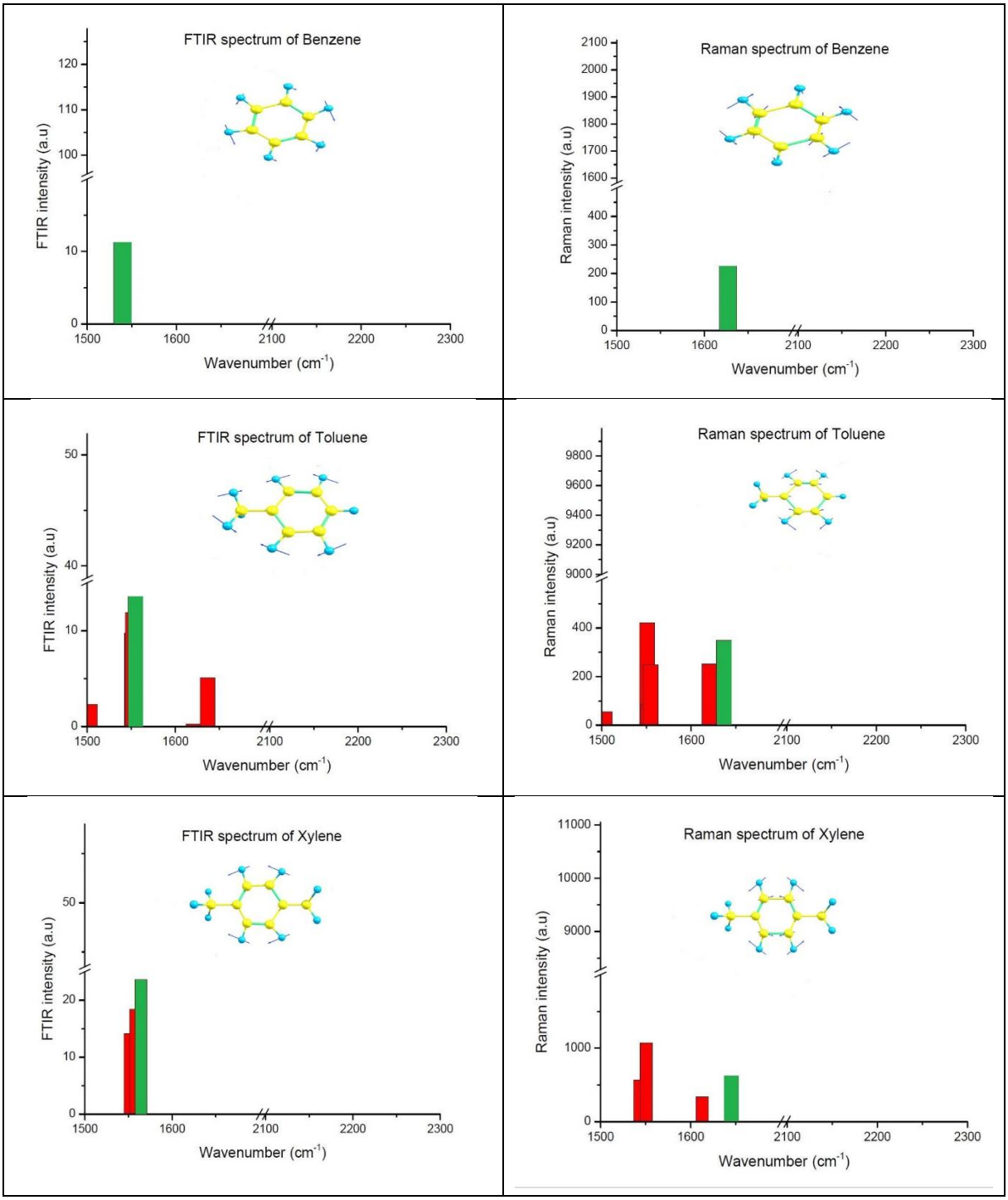

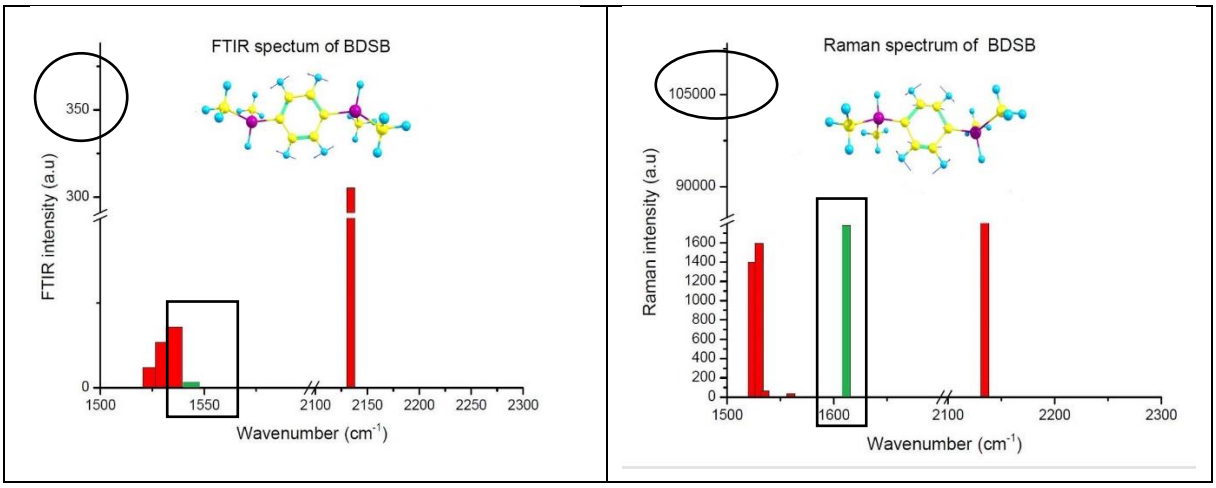

2.13. Characterisation of the macromolecules *via* the SEC/MALS couplings

Since the mid-sixties, polymer chemists have used size exclusion chromatography (SEC) in polymer research. Nowadays, SEC instruments are rather easy to manipulate and greatly reliable. Nevertheless, concerns about reproducibility of results are raised, notably in the sense of long-term reproducibility inside a laboratory. The reason of the unsatisfactory reproducibility is the effect of high sensitivity of the results to various operational parameters, which is commonly disregarded by inexperienced users. One of the major shortcomings of SEC is that the method does not determine any physical quantity directly associated with molar mass. Since this method only separates polymer molecules based on their hydrodynamic volume, the SEC columns need to be calibrated in order to set up a relationship between the molar mass and elution volume. However, the calibration step presents a manifold of limitations and determining the true calibration for many natural and synthetic polymers is near to impossible. Usually, a reference calibration curve is used for processing the data of other polymers of different chemical molecular architecture or composition. Consequently, the resulting molar masses may diverge from the true ones quite considerably.

To overcome the SEC limitations, the SEC was coupled with a light scattering technique namely the multi angle light scattering (MALS). The MALS uses two important principles of basic light scattering *i.e.*: i) the amount of light scattered is directly proportional to the product of the polymer molar mass and concentration; ii) the angular variation of the scattered light is directly related to the size of the molecule [PO11]. Moreover, the two light scattering principles are embodied in the Rayleigh-Gans-Debye equation:

$$R(\Theta) = K^* McP(\Theta)[1 - 2A_2 McP(\Theta)], \qquad \text{Eq. (2.23)}$$

where $R(\Theta)$ is the excess (i.e., from the solute alone) Rayleigh ratio. The ratio of the scattered and incident light intensity, corrected for size of scattering volume and distance from scattering volume.

$$K^* = \frac{4\pi^2 n_0^2}{N_A \lambda_0^4} \left(\frac{dn}{dc}\right)^2 , \qquad \text{Eq. (2.24)}$$

where: n_0 – solvent refractive index; N_A – Avogadro's number; λ_0 – vacuum wavelength of incident light; dn/dc – specific refractive index increment. dn/dc represents the change of the refractive index of a polymer solution with respect to the concentration of the solute. Measuring the specific refractive index increment is of upmost important as it helps in the absolute characterization of the molar mass, as it is a term used in the molar mass calculation; M – molar mass; C – solute concentration (g·mL^{-1}); $P(\Theta)$: form factor or "scattering function". $P(\Theta)$ relates the angular variation in scattering intensity to the mean square radius r_g of the particle. The larger r_g, the larger the angular variation; A_2 – second virial coefficient, a measure of solute-solute in solvent interaction.

Therefore, coupling a MALS to a SEC has various advantages: for instance, the calibration problems would be successfully fixed by the MALS detectors. In addition, it would hugely enhance the reproducibility and repeatability of the measurements. Therefore, SEC/MALS is a powerful technique for absolute characterisation of macromolecules in terms of molar mass, size, conformation and conjugation ratio. The size exclusion chromatography coupled with a multi-angle light scattering set up is shown in Figure 2.22.

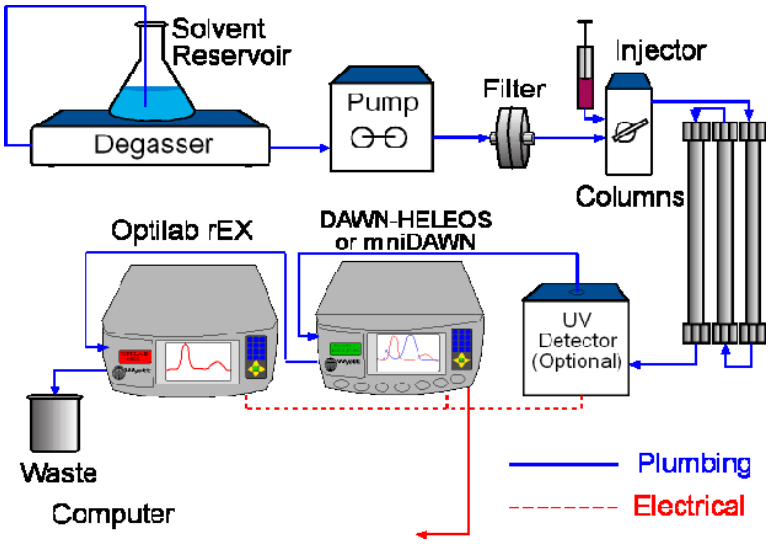

Figure 2.22. Typical SEC/MALS set-up.

The SEC-MALS system consists of a Shimadzu High Performance Liquid Chromatography (HPLC) system (degasser, quaternary pump, column holder/temperature

controller, and UV-vis diode array detector) coupled with a Wyatt Technology DAWN HELEOS II multi-angle laser light scattering detector and a Wyatt Technology Optilab T-rEX refractive index (RI) detector. A Shodex GPC KF-803L column of size 8.0 mm ID x 300 mmL is used for the HPLC separation of the samples. Wyatt Technology Astra VII software is used for data collection and analysis. The SEC-MALS would help in determining the average molar mass, the molar mass dispersity and the conformation of the polymer of sampled polymer solution from RBF.

2.14. Nuclear Magnetic Resonance (NMR) Spectroscopy

Nuclear magnetic resonance analysis was carried out to investigate the structure of the obtained hyperbranched polycarbosilane. Through this analysis technique, it was possible to obtain information on the environment of the proton (^{1}H) and carbon (^{13}C). Liquid-state ^{1}H NMR, ^{13}C NMR and 2D COSY NMR were carried out by the Faculty of Pharmacy at the University of Limoges. The spectra were recorded with a Bruker Avance III 500 MHz spectrometer (B_0 = 11.4 T). Chemical shifts (δ) are expressed in parts per million with tetramethylsilane as an internal standard (δ = 0 ppm). Data were reported as follows: chemical shift, multiplicity (s – singlet; se – septet; m – multiplet; br – broad), and assignment.

Moreover, Solid-state ^{29}Si NMR analyses were carried out at the Laboratory of Chemistry of Matter Paris Digest (LCMCP). The spectra were recorded with a Bruker Avance 300 MHz spectrometer at B_0 = 7.05 T (ν_0 (^{29}Si) = 59.66 MHz), using a CP-MAS Bruker probe with 4 mm ZrO_2 rotors spinning at 5 kHz. Chemical shifts are referenced to tetramethylsilane (δ = 0 ppm). {^{1}H}–^{29}Si cross-polarization (CP) magic angle spinning (MAS) experiments were recorded with a contact time of 1 ms and 4000 scans. Solid-state ^{13}C NMR experiments were performed with a Bruker Avance III 700 MHz spectrometer at B_0 = 16.4 T (ν_0 (^{13}C) = 176.07 MHz) with a 2.5 mm double resonance Bruker MAS probe spinning at 10 kHz. ^{13}C NMR chemical shifts are referenced to tetramethylsilane. ^{13}C CP-MAS experiment were conducted with a recycle delay of 3 s, a contact time of 2 ms and 1640 scans.

2.15. Thermogravimetric analysis (TGA) coupled with mass spectrometry (MS)

The thermal behaviour of the obtained hyperbranched polymer was studied by thermogravimetric analysis (TGA) using a thermobalance (STA 449 F3, Netzsch) in a SiC oven. It was used to measure the weight loss as a function of time and temperature, this has enabled us to calculate the yield of the ceramic obtained. The thermal analysis cycle has been configured such that the temperature rise rate is 10 °C.min^{-1}, up to a temperature of 1400 °C. Before each analysis, a blank was carried out with an empty alumina crucible in

order to subtract its contribution from the results obtained. All analyses were carried out under a neutral atmosphere (Argon) in order to avoid any contamination by oxygen. This argon sweep also served as a vector for conveying the gaseous species resulting from the thermal degradation of the polymer to a mass spectrometer (Omnistar, Balzers Instruments) coupled to the apparatus described above. At the inlet of the device, a gas flow of between 1 to 2 sccm (Standard Cubic Centimetre per Minute) was injected and the ionized fragments produced were analysed by a quadrupole allowing the separation of the ions according to the ratio (m/z). This ratio corresponds to the mass (m) of the ionized species divided by its charge (z). The acquisition was carried out as a function of time in parallel with the thermogravimetric analysis, and the values obtained (m/z) are expressed in Unit of Atomic Mass (AMU) over an interval of 1 to 200 AMU.

2.16. X-ray diffraction (XRD)

X-ray diffraction (XRD) analysis was performed on pyrolysed powders (pyrolysis took place at different temperatures: 800 °C, 1000 °C, 1200 °C and 1400 °C). It is a sensitive technique to the organisation at the atomic scale of crystallised phases. It also enables identifying reference phases in samples. The sample is irradiated with an X-ray beam and the intensity scattered by this sample is measured as a function of the diffraction angle 2θ. The X-ray diffraction analyses of the samples were carried out on an apparatus D8 advance type (Brüker, Karlsruhe, Germany) in θ-2θ configuration of the Bragg-Brentano type with a copper anticathode. The X-ray source used the Kα radiation from copper whose wavelength was $\lambda_{CuK\alpha1}$ = 1.540598 Å. Diffraction data was analysed with EVA software.

2.17. Scanning electron microscopy (SEM)

Scanning electron microscopy was carried out on paralysed material after heat treatment at 1400 °C to investigate the surface aspect of the material. Scanning electron microscopy is based on the principle of electron-matter interaction, capable of producing high-resolution images of the sample surface. The morphology of powders is characterised using a scanning electron microscope (JEOL, JSM-IT300). The acquisitions were made in SED (Secondary Electrons Detector) mode under high vacuum, with an acceleration voltage ranging from 10 to 15 kV and a working distance of 10 mm. This setup was coupled with an energy dispersion X-analyser (EDS) to estimate the composition and distribution of chemical elements in a defined area of the sample, or to perform elementary mapping of a surface. The samples analysed were metallised with platinum to facilitate the flow of charges on their surface.

Chapter 3.

Relationship between kinetics of polymerisation and rheological behaviour of a preceramic polymer

3.1. Introduction

The first part of this chapter deals with the synthesis and the characterisation of the hyperbranched polycarbosilanes *via* ^{1}H, ^{13}C, ^{29}Si NMR spectroscopies, TGA, SEM and XRD. Since one of the aims of the PDCs route was to control and understand the chemical and physical changes occurring during the polymerisation, several coupling devices have been reported for the monitoring of the hydrosilylation reaction. Table 3.1 illustrates the different coupling devices used in this chapter. The second part of this chapter would demonstrate the reasons of combining a Raman spectrometry with a Rheo-FTIR setup. In addition, preliminary monitoring of the polymerisation reaction was carried out on the Rheo-Raman setup as the results obtained was used as a reference in optimising the Rheo-Raman-FTIR setup. The Rheo-Raman-FTIR setup was optimised in terms of gap, and intensity of the Raman signal. Moreover, the homogeneity of the reaction across the plate-plate geometry was investigated as well as the effect of varying the catalyst concentration on the polymerisation reaction. Ultimately, after optimising the Rheo-Raman-FTIR setup, the correlation between the monomer conversion and the viscosity of the medium was illustrated.

Table 3.1. Summary of different coupling devices used.

Rheo-FTIR setup.	**Rheo-Raman setup**.	**Rheo-Raman-FTIR setup.**
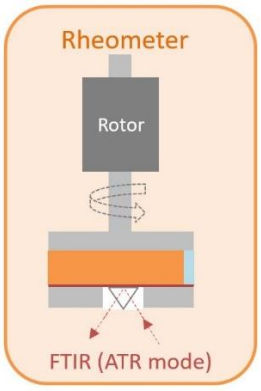	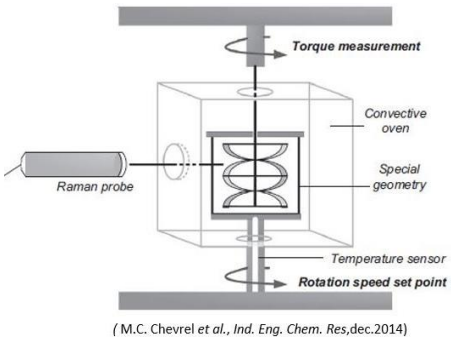 (M.C. Chevrel *et al., Ind. Eng. Chem. Res*,dec.2014)	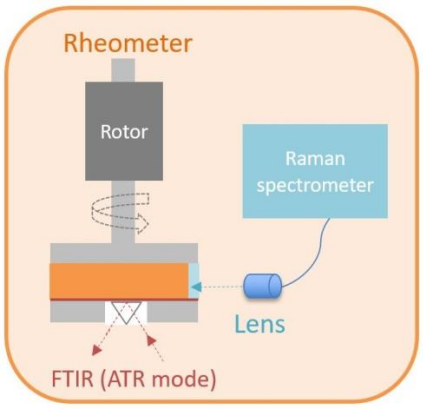

3.2. Synthesis and characterisation of a hyperbranched polycarbosilane

The literature review reported different routes to synthesis polycarbosilanes *via* PDCs route (PDC) [BO16] [LA97] [JI17]. Among them, the hydrosilylation reaction was of particular interest, because, as previously mentioned, this route has the faculty to generate polymers with only Si, C, and H elements in their structure. This is a major benefit as we seek to generate SiC ceramics materials. Thus, a hyperbranched polycarbosilane was generated *via* a hydrosilylation reaction by using 1,4-bis-(dimethylsilyl)benzene (BDSB) with tetraallylsilane (TAS) in the presence of a platinum-based catalyst called Karstedt catalyst. The reaction was conducted in toluene as shown in Figure 3.1.

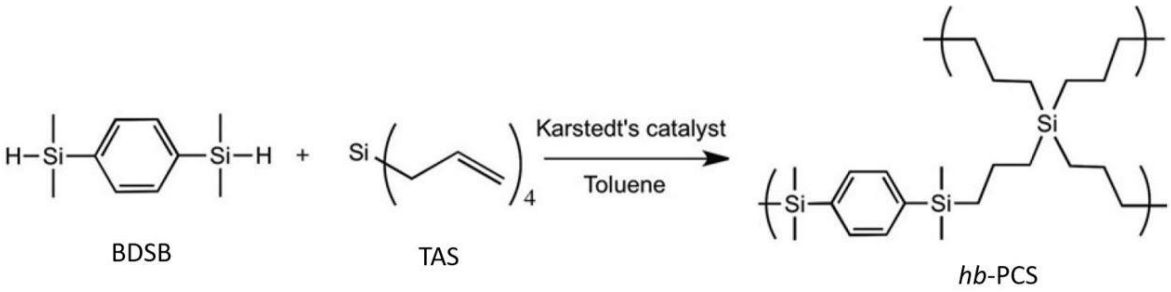

Figure 3.1. Synthesis of a hyperbranched polycarbosilane (*hb*-PCS) by hydrosilylation.

This reaction led to a hyperbranched polycarbosilane with a 94 % yield [PI18]. These reagents were selected since they were commercially available, and they led to a gel-like polymer which could be easily shaped into desired form to generate for example porous ceramics [LA17] [VA16].

3.2.1. Characterisation of the polymer *via* ^{1}H, ^{13}C and ^{29}Si NMR spectroscopies

Liquid-state ^{1}H NMR and ^{13}C NMR spectroscopies were utilised to determine the structure of the hyperbranched polymer, despite its low solubility in toluene-d_8. Following the ^{1}H NMR spectrum of the hyperbranched polymer, different peaks were determined such as the methyl or methylene groups that could be associated to silicon at 0.17-1.78 ppm, and the protons of BDSB phenyl groups (6.78-7.59 ppm) as shown in Figure 3.2.

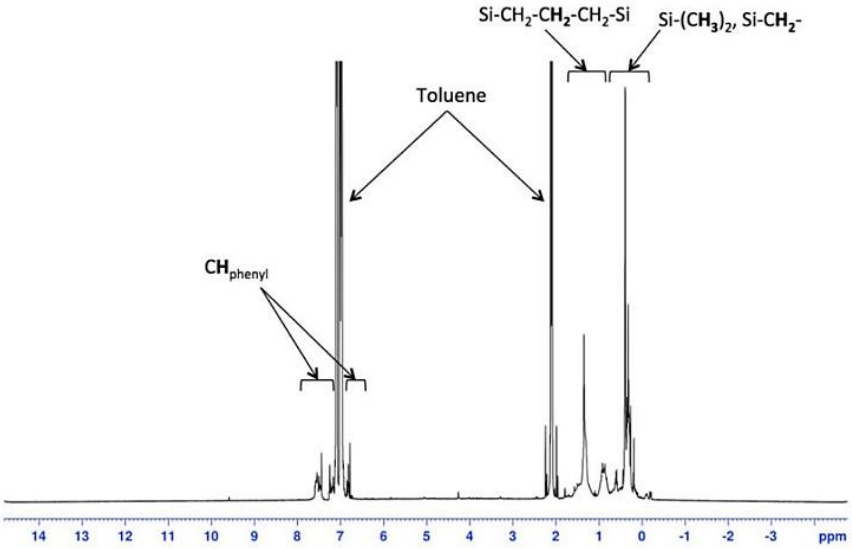

Figure 3.2. ^{1}H NMR spectrum of *hb*-PCS in toluene-d_8.

Moreover, 2D COSY NMR was carried out to point out the $R(CH_3)_2Si\text{-}CH_2\text{-}CH_2\text{-}CH_2\text{-}SiR'(CH_3)_2$ sequences establishing the fact that the hydrosilylation reaction happened. Indeed, a relation between the signals of $Si\text{-}CH_2\text{-}$ and $\text{–}CH_2\text{-}CH_2\text{-}CH_2\text{-}$ was noticed as shown by the dashed circles in Figure 3.3.

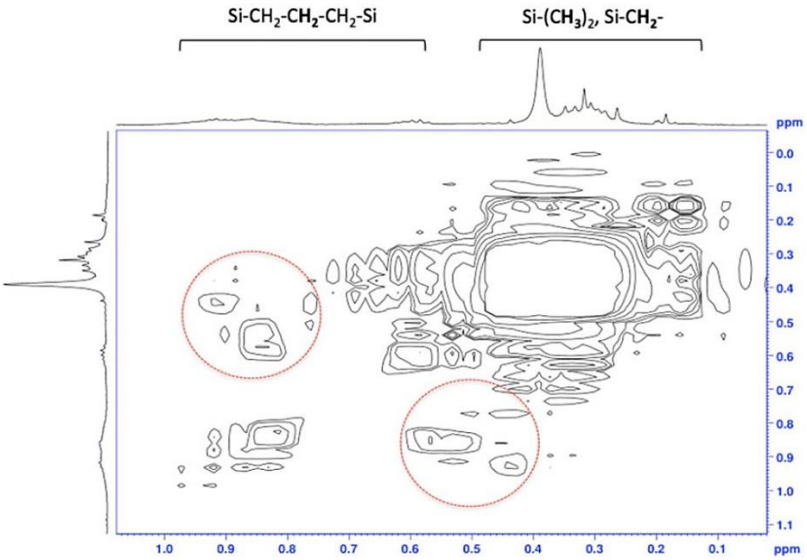

Figure 3.3. 2D COSY ^{1}H NMR analysis of *hb*-PCS.

Furthermore, solid-state ^{29}Si as well as ^{13}C NMR spectroscopies were carried out on the polymer structure. The ^{29}Si NMR spectrum revealed two Si environments at 1.1 ppm and at -3.5 ppm (Figure 3.4a) corresponding to $Si(CH_2)_4$ and $SiAr(CH_2)_3$ respectively. These findings were in accordance with previous work pointing out an upfield shift for such environments of Si with an aryl group. Moreover, ^{13}C solid state NMR results (Figure 3.4b), indicated upfield peaks for CH_2-CH_2-Si, Si-CH_2- and Si-CH_3 environments at 21, 19 and -2 ppm respectively while at the downfield signal, carbon in the phenyl ring was observed at 134 ppm. The NMR analyses managed to predict the structure of the polycarbosilane.

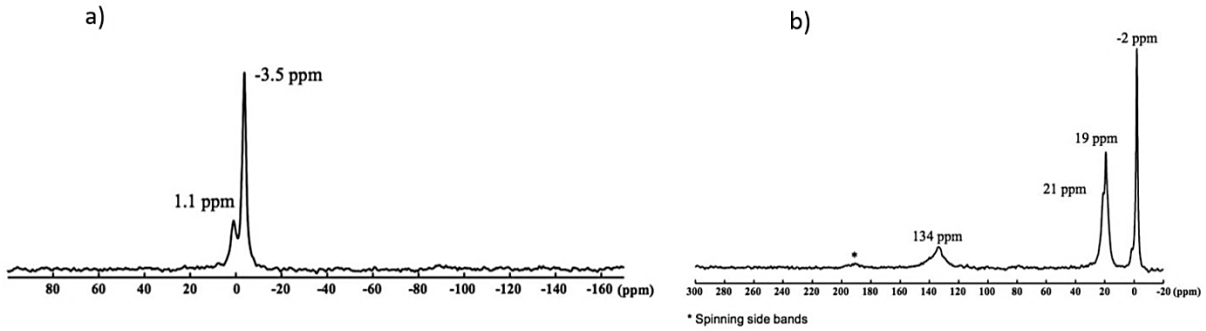

Figure 3.4. a) ^{13}C and b) ^{29}Si CP-MAS NMR spectrum of *hb*-PCS.

3.2.2. Characterisation of the ceramic *via* TGA, SEM and XRD

TGA was used to monitor the conversion process from the polymer precursor to the ceramic. A four-step weight loss was exhibited by the TGA curve as shown in Figure 3.5.

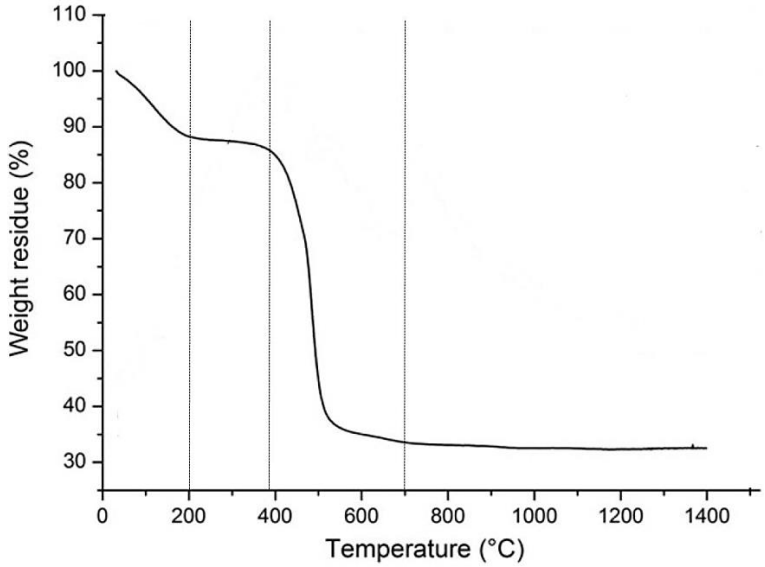

Figure 3.5. TGA curve of *hb*-PCS under a flowing argon atmosphere with a heating rate of 10 °C min^{-1}.

For the first 200 °C, quite a considerable weight loss happened (*ca* 12 %). This event could be related to the loss of residual toluene from the preceramic polymer. From 200 to 380 °C, no mass loss was noticed. The highest weight loss was observed between 380 to 700 °C (*ca* 54 %), which was due to the decomposition of organic groups during the ceramisation of the polymeric precursor. At last, above 700 °C a very low weight loss was detected, which demonstrated a good thermal stability of the resulting pyrolysis product. Without considering the solvent release below 200 °C, a 40 wt % ceramic yield was reported with presumably the presence of porosity in the end product. These findings were further confirmed by analysing the microstructure of the ceramic (Figure 3.6), which showed a large range of pore diameters that could correspond to the presence of porosity. This microstructure could be useful for further applications in the domain of catalysis [PA13] [VA18].

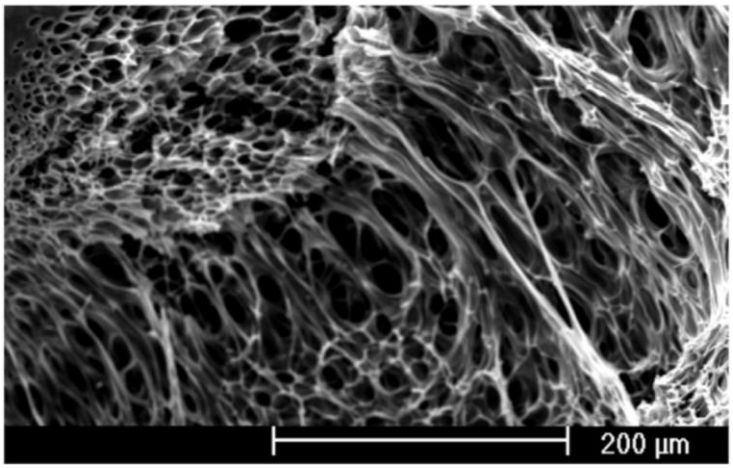

Figure 3.6. SEM image of residual porosity in the pyrolysis PCS after heat treatment at 1400 °C.

At last, the X-ray diffraction (XRD) analysis was carried out on the pyrolysis products for various pyrolysis temperatures as described in Figure 3.7. When the pyrolysis temperature increased from 800 to 1400 °C, β-SiC phase (JCPDS no. 00-029-1129) was present above 1200 °C, which pointed out the success of the synthesis to produce SiC polymer precursor. Below 1200 °C, only poorly crystallised carbon was revealed. As the temperature increased, (above 1200 °C), the SiC diffraction peaks transformed into sharper peaks indicating an increase of the crystal size, while the carbon peaks stayed unchanged.

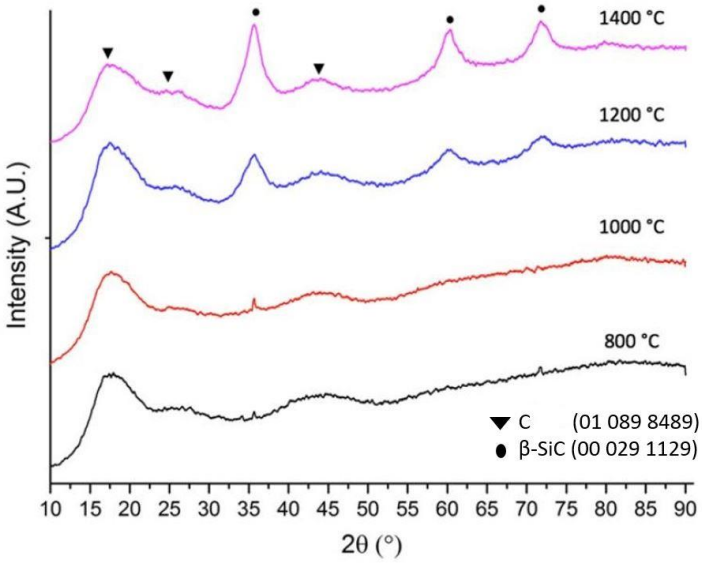

Figure 3.7. XRD patterns of the pyrolysis product of *hb*-PCS at 800, 1000, 1200 and 1400 °C.

Hence, a hyperbranched polycarbosilane was synthesised, which under heat treatment can be transformed into porous ceramics. As one of the main objectives was to develop a better understanding of synthesised polycarbosilane materials notably in terms of shaping, before the pyrolysis step. Hence, it was pivotal to establish a link between polymer architectures and the consequence on the future ceramics. This was accomplished by performing the monitoring of the polymerisation reaction that required a real time control of the construction of macromolecular structures under defined atmosphere and temperature. In addition, the rheological data of the polymer were of great importance, because they would condition the future shaping process. To answer this need to retrieve multiple parameters at the same time, which would improve the quality of production of polycarbosilanes, an adapted instrumentation was necessary. Since one of the challenges of the PDCs route was to control physical and chemical transformations that occurred during the polymerisation, a device that dynamically combined a rheometer and an infrared spectrometer was useful to monitor both the structure of the growing macromolecules and their rheological behaviour.

3.3. Monitoring of the reaction kinetics *via* a rheometer coupled with an FTIR spectrometer

As detailed previously in the bibliography, several studies described the use of the coupling Rheo-FTIR to monitor various polymerisation reactions. The Rheo-FTIR coupling would allow the monitoring of the hydrosilylation reaction under controlled temperature and atmosphere starting with defined monomers with the aim of better understanding the relationship between the kinetics of the hydrosilylation reaction and the rheological behaviour of the preceramic polymer. However, before starting the coupling study, it was necessary to know the spectral signatures of the reagents involved. Hence, a preliminary study of the individual spectra was carried out and characteristics bands of the reagents were highlighted in chapter 2. The signature of functional groups of each monomer *i.e.* the stretching vibration of the Si-H (2117 cm^{-1}) in BDSB and the C=C (1630 cm^{-1}) in TAS were involved in the hydrosilylation reaction. To monitor the polymerisation reaction, either one of the monomers modes could be used to carry out the kinetic study as they both bands decreased during monomer conversion. Figure 3.8 illustrates the spectra at the beginning of the reaction and one when no more evolutions within the spectra were noticed.

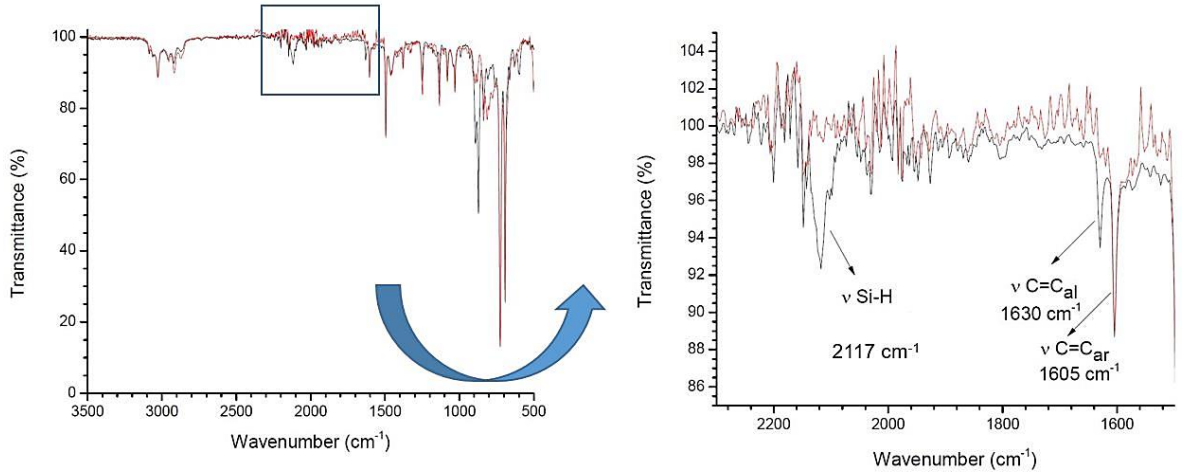

Figure 3.8. FTIR spectra of the reaction mixture (black curve t = 0 s) and of the resulting polymer (red curve t = 10000 s).

The advantage of combining a rheometer to an FTIR spectrometer was that we could directly correlate the monomer conversion obtained from real time FTIR spectroscopy to the *in-situ* rheological measurements. Combining the macroscopic properties data such as loss and storage moduli from rheology with molecular properties such as monomer conversion from FTIR spectroscopy, would result in a better understanding of the fundamental processes occurring during the polymerisation reaction. As stated in chapter 2, the alkene band (C=C 1630 cm^{-1}) from TAS was chosen to follow the conversion of the monomers. The

results were obtained after a time dependent oscillatory test was performed at a frequency set at 1 Hz and a strain at 0.5. The conversion of alkene was calculated as a function of time, at 25 °C (Figure 3.9). During the initial moments of the reaction, the conversion of alkene increased rapidly by approximately 0.5 for a time of 2000 s. Between 2000 s to 6000 s, a slower increase was observed indicating a lower kinetic rate due to a decrease in the concentration of the reactants as well as steric hindrance. Ultimately, the conversion of the alkene became stable after 6000 s and a maximum conversion of 0.71 was recorded.

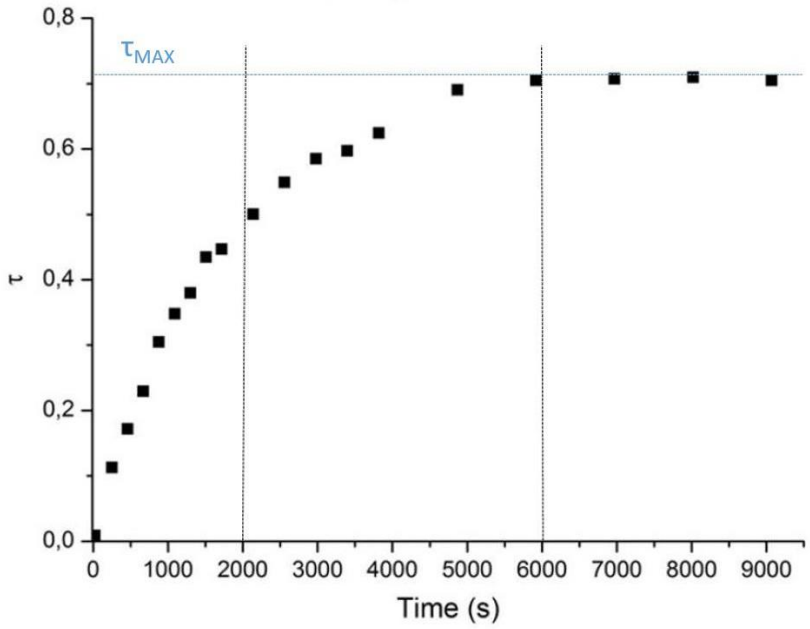

Figure 3.9. Alkene conversion (obtained from FTIR data) plotted as a function of time at 25 °C.

In parallel, to visualise the impact of the kinetics of the polymerisation reaction on the rheology of the ceramic precursor, the rheological moduli were plotted against the alkene conversion. During the initial phase of the reaction, the storage (G') and loss (G'') moduli were constant as displayed in Figure 3.10. However, after a critical conversion rate close to 0.5, a sudden increase was noticed for the storage modulus that was up to two orders of magnitude compared to that of the loss modulus. Consequently, for a change of conversion of 25 %, the storage modulus increased by five orders of magnitude. The storage modulus was more responsive to the macromolecular growth for conversions greater than 0.5. Under this value, the conversion progressed more rapidly with no real impact on the rheological properties, as the macromolecular networks were not built enough during the step-growth polymerisation to properly influence the storage modulus.

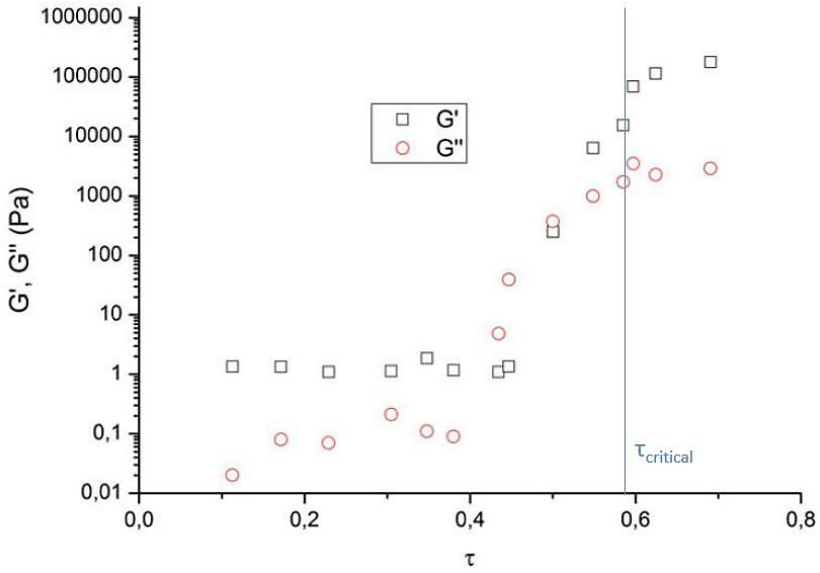

Figure 3.10. Evolution of storage (G') and the loss (G'') moduli as a function of alkene conversion.

Moreover, it was interesting to observe that the theory of gelation from Flory-Stockmayer could correspond to the critical conversion of the alkene. Indeed, the conversion at gel point can be expressed as:

$$\tau_c = \sqrt{\frac{1}{f_0(f_{c=c^{-1}})(f_{SiH^{-1}})}}, \qquad \text{Eq. (3.1)}$$

where f_0 is the stoichiometric ratio (= 1 in this case), $f_{C=C} = 4$ is the functionality of TAS and $f_{SiH} = 2$ is the functionality of BDSB. In agreement with these values, a critical conversion of 0.58 was calculated. This was in conformity with the gel time acquired from the Rheo-FTIR coupling.

This study demonstrated that the Rheo-FTIR coupling enabled real time monitoring of the hydrosilylation reaction by starting with defined monomers under controlled atmosphere and temperature. The *in-situ* experiment successfully correlated monomer conversion to the corresponding macroscopic rheological properties. However, the maximum alkene conversion was reached after 6000 s, indicating a slow rate of reaction. To optimise the studies further, the catalyst concentration will be adjusted. Indeed, this modification was essential, as the same polymerisation reaction will be performed in RBF. By taking in consideration, the reaction time was too long and counterproductive for sampling purposes in RBF. The rate of reaction was increased by increasing the catalyst concentration from 0.004 to 0.415 mmol·L^{-1}. Moreover, the Rheo-FTIR appeared to have some limitations since during the real time monitoring information were being acquired only at a single point across the whole sample; hence, the acquired data were not representative of the whole medium. As a

result, the addition of a Raman spectrometer was proposed to the existing coupling Rheo-FTIR notably to retrieve information in volume to better understand the kinetics of the reaction.

3.4. Contribution of Raman spectroscopy to the Rheo-FTIR setup

The combination of the Raman spectrometer to the existing Rheo-FTIR setup represented a major advantage since the combination of the two vibrational spectroscopy techniques complement each other. It is known that infrared (IR) absorption and Raman scattering spectroscopy provide complementary information of molecular vibrations: the former is active for anti-symmetric vibrations that alter the dipole moment, while the latter for symmetric vibrations that alter the polarizability. IR absorption spectroscopy, which is active for polar bonds such as O–H or N–H, is often used for identification of functional groups of molecules, while Raman scattering spectroscopy, active for bonds such as C=C, S–S, or C–S4, is used for identification of skeletal structures. Moreover, by combining the Raman spectrometer equipped with a lens to the existing Rheo-FTIR setup complementary information in terms of spatial resolution will be obtained. The ATR provides a spatial resolution in micrometre while the spatial resolution for the Raman spectrometer is measured in millimetre. Furthermore, the ATR provided only a surface information that is not representative of what is happening within the volume of the sample, while the Raman spectrometer associated with a lens will retrieve information with a larger depth penetration. Therefore, the combination of the Raman spectrometer to the existing Rheo-FTIR setup (Rheo-FTIR-Raman) enabled a better understanding of the relationship between the kinetics of the polymerisation by exploiting the complementary nature of the two vibrational techniques and the rheology of the preceramic polymer.

Nevertheless, this was not the first time that a Raman spectrometer was coupled with a Rheometer. As stated in the bibliography chapter, Chevrel *et al.* used a laboratory-made Rheo-Raman device to monitor a free radical polymerisation of acrylic acid in an aqueous medium [CH12] [CH14]. This coupling succeeded to overcome some challenges associated to the monitoring of the polymerisation reaction like by using a couette configuration, different parameters were accessible at the same time, such as monomer conversion or viscosity of the medium. Since interesting results were obtained, the authors used the Rheo-Raman coupling to monitor other polymerisation reactions such as styrene polymerisation or to develop a high impact polystyrene process [BR13] [BR14].

By considering that this device could correlate the macroscopic viscosity with the medium composition, a preliminary study on the *in-situ* monitoring of the hydrosilylation reaction was undertaken. The reason why a preliminary study was undertaken on the Rheo-

Raman setup was that the results obtained could be used as a reference in optimising the Rheo-Raman-FTIR at IRCER especially in terms of Raman signal acquisition.

3.5. Preliminary monitoring of the reaction kinetics *via* a Rheo-Raman setup (Rheo-C-R)

This experiment was carried out at Laboratoire Réactions et Génie des Procédés (LRGP-UMR 7274-Nancy). The Rheo-Raman setup was composed of a small-scale reactor (14 mL) wherein the polymerisation reaction took place as shown in Figure 3.11. The mixer-type rheometer (model AresG2) was equipped with a quartz outer cylinder and was combined to a Raman spectrometer for *in-situ* measurements. A laboratory-made geometry, identical to industrial reactors, consisted of a mobile cylindrical chamber in quartz and a stationary helical ribbon that was utilised as a mixing tool. Moreover, the non-contact Raman spectroscopy measurements were carried out *via* the convective oven window and quartz outer cylinder due to the focalising system of the probe adapted to the rheometer size. The Raman spectrometer (Model RXN2, Kaiser Optical Systems) had a non-contact fibre-optic probe (objective) that provided a spectral resolution of 1.5 cm^{-1}. The laser excitation wavelength was 785 nm. The temperature was kept at 25°C throughout the experiment so that the reaction was not activated thermally. The optic probe was placed 10 mm from the mobile cylinder. Raman spectra acquisition were performed with an exposure time of 2 s and an interval time of 5 s.

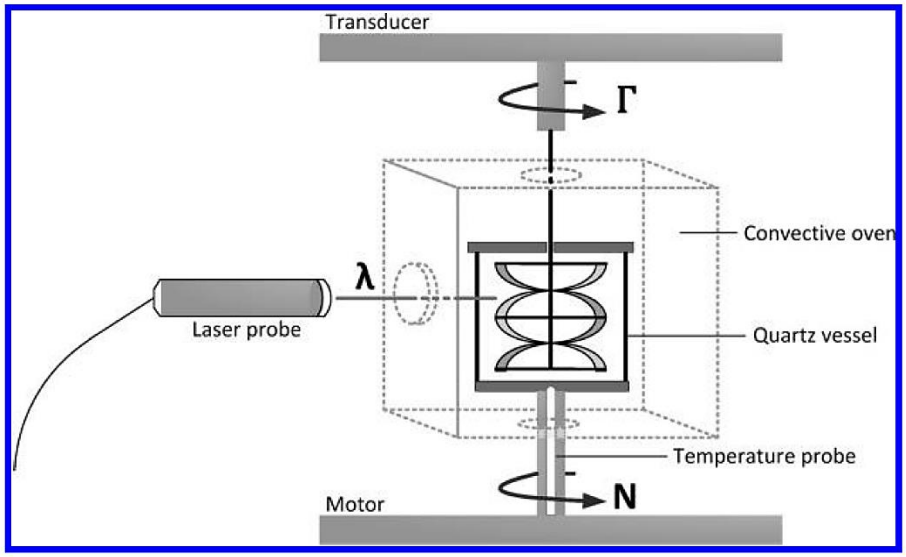

Figure 3.11. Schema of the rheometer-Raman spectrometer coupled experiment [CHE12].

The rheometer was set at a shear rate of 35 s^{-1} to ensure a homogeneous mixture of the solution during the polymerisation and rheological data were acquired every 1 s. The experiment lasted until the intensity of the Raman signal was lost due to the sudden

contraction that occurred during polymerisation. The fitted Raman intensity of bands such as stretching vibration of C=C BDSB, TAS, Toluene and Si-H were plotted against time as shown in Figure 3.12.

The graph was divided into 4 regions. In the first region, the intensity of the stretching vibration of C=C toluene and BDSB were almost constant while the stretching vibrations of C=C of TAS and Si-H started to decrease. The catalyst was added at t = 0 (in region 1), a decrease of 3.17 % and 3.1% was registered for C=C of TAS Si-H respectively at the start of the reaction. In region 2, a sharp decrease of 14.1 % and 11.4 % was observed for the stretching vibrations of C=C of TAS and Si-H respectively indicating that the functional groups of the reagents were being consumed rapidly. On the other hand, the decrease registered for the stretching vibration of C=C toluene (5.6 %) was associated to the evaporation of the solvent due to the exothermic reaction. The stretching vibration of C=C BDSB reported a slight decrease of 2.6 % in this region.

In region 3 and 4, both the stretching vibration of C=C of toluene and BDSB remained constant. No more evaporation of toluene occurred in region 3 because the solvent was being trapped as the gel was being formed. A slower decrease of 2.40 % and 3.60 % was reported for the stretching vibration of Si-H and C=C of TAS in region 3 in comparison to region 2 since the functional groups were less accessible. In region 4, the stretching vibration of Si-H and C=C of TAS tended towards zero as the bands were almost completely consumed. By using the intensities of the stretching vibrations of the functional groups, the alkene and Si-H conversion were calculated.

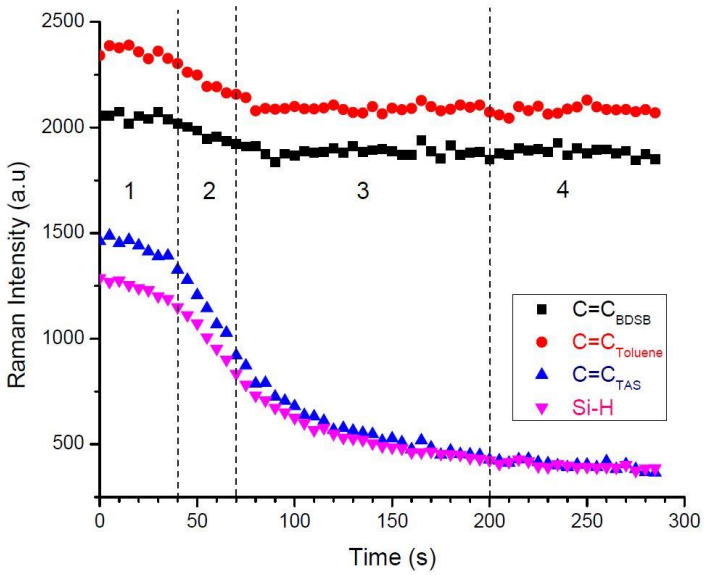

Figure 3.12. Evolution of fitted peak intensities of monomers during polymerisation as a function of time in a Couette configuration.

The coupling experiment carried out in real time allowed us to correlate monomers conversion with the rheological measurements as shown in Figure 3.13. During the initial stages of the reaction, the viscosity remained constant even though the monomers conversion increased rapidly from 0 to nearly 0.5 in the first 100 s. After 100 s, the monomers conversion registered a slower increase as the functional groups were being less accessible. Based on the calculation from equation 3.1, a critical conversion rate of 0.58 was calculated. It was noticed that after this threshold the viscosity increased rapidly from 0.015 to 1.1 Pa·s. Below this critical conversion value, there was no concrete influence on the rheology of the polymer as the macromolecular networks were not developed enough to really affect the viscosity of the medium.

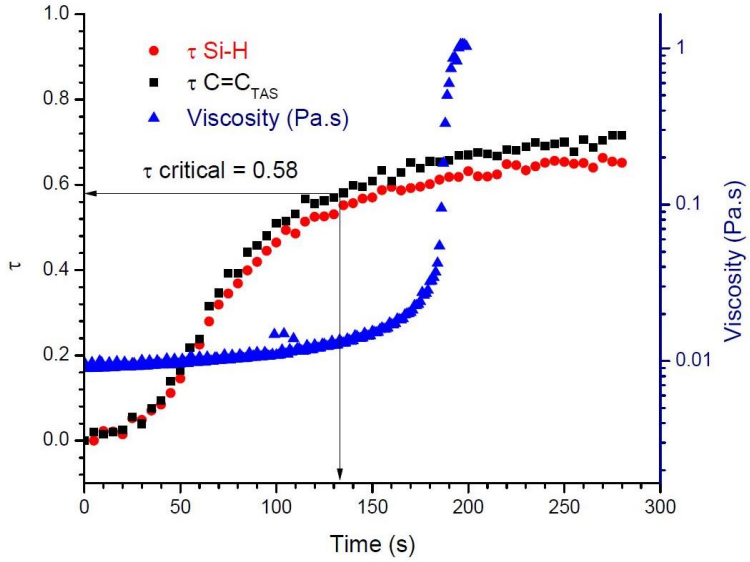

Figure 3.13. Evolution of structural conversion and viscosity against time in a couette configuration.

The graph of viscosity was not plotted after 200 s as the gel formed was attached to the helical ribbon; therefore, the material was no longer sheared properly. Hence, viscosity data obtained after 200 s was disregarded. Nevertheless, the hydrosilylation reaction was successfully monitored in real time under well-defined parameters such as a constant temperature of 25 °C. Thus, the obtained result from the Rheo-Raman experiment was used as a reference to help in designing the Rheo-Raman-FTIR setup. Therefore, the hydrosilylation reaction was repeated on the Rheo-Raman-FTIR setup by keeping the same reagents concentration.

3.6. Optimisation and monitoring of the reaction kinetics by the Rheo-FTIR-Raman setup

The optimisation of the Rheo-Raman-FTIR setup was carried out since it was important to predefine the parameters and conditions that was most suited to perform the monitoring of

the hydrosilylation reaction. The schema in Figure 3.14a represents the Rheo- Raman-FTIR setup. As mentioned in Chapter 2, the rotational rheometer (Mars III, Thermo Scientific™ HAAKE™ MARS™ Rheometer) has a Rheonaut module with a side port to equip a standard FTIR spectrometer. A plate-plate geometry was used with a gap of 0.6 mm. This gap was chosen since the reagents were viscous and the 0.6 mm gap provided the wettability required to hold the reaction mixture reagents between the plate-plate geometry. In addition, the 0.6 mm gap was of economic interest since only a small quantity of reagents would be loaded between the plates. Concerning the Raman spectrometer, a Raman probe with a lens of 100 mm of focal distance was used. The lens' position could be adjusted accordingly with the help of a lab-made support on which the Raman head resided.

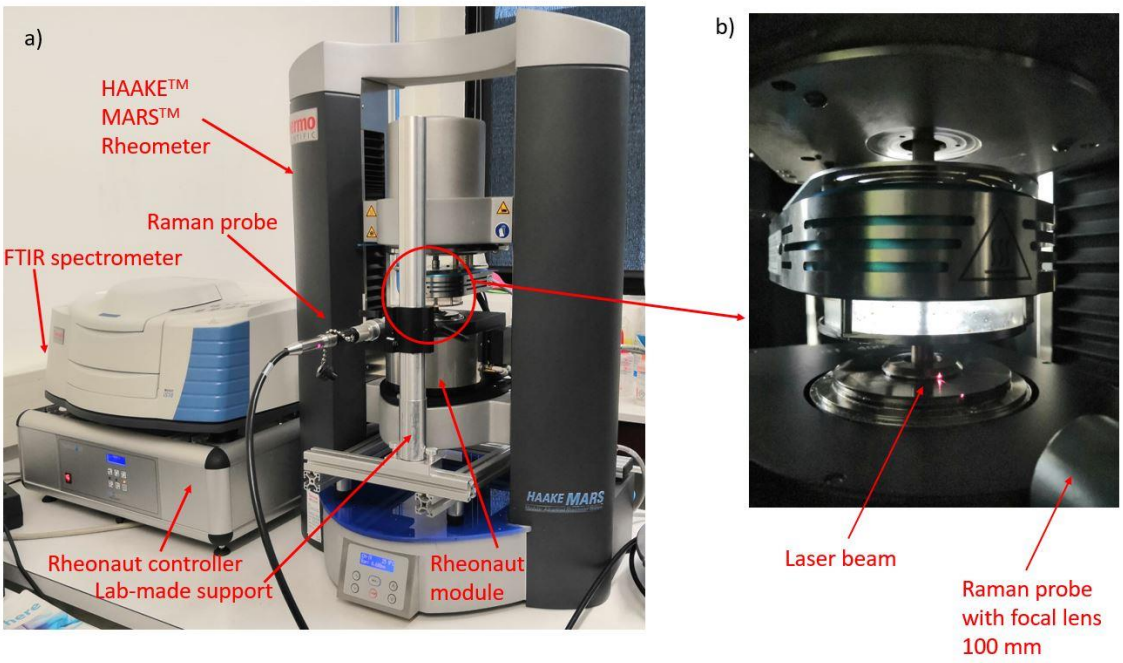

Figure 3.14. a) Schema of the rheo-FTIR-Raman in a plate-plate (PP) configuration; b) Laser beam probing the sample through the 0.6 mm gap.

The challenge to use the Raman spectrometer with a lens of focal distance of 100 mm lies in successfully probing the sample completely with the selected 0.6 mm gap distance. Indeed, it was a strenuous task to probe the sample given the restriction imposed in terms of gap. The solvent toluene was used to optimise the signal since it was a cheaper option in comparison to the other reagents (TAS or BDSB). In addition, the toluene band remained unchanged during the reaction, and was present at 1607 cm^{-1} in the area of interest. For these reasons, and before each experiment, the signal optimisation was carried out on the stretching vibration of C=C (1607 cm^{-1}) of toluene. Before carrying out the optimisation, the rheometer was initiated in terms of gap and inertia. Once the solvent toluene was placed in between the plate-plate configuration, the experiment was launched. The upper plate of the

geometry was in motion while the lower plate was fixed during the experiment. The optimisation of the Raman signal was conducted with the help of the lab-made support. After some trial tests, the laser beam correctly probed the sample between the plate-plate configuration. Unfortunately, part of the laser beam was in contact with the metal part of the plate-plate geometry due to the 0.6 mm gap selected (Figure 3.14b). However, even with the gap constraint, a sharp amplitude of the stretching vibration of C=C of toluene was achieved as illustrated in Figure 3.15.

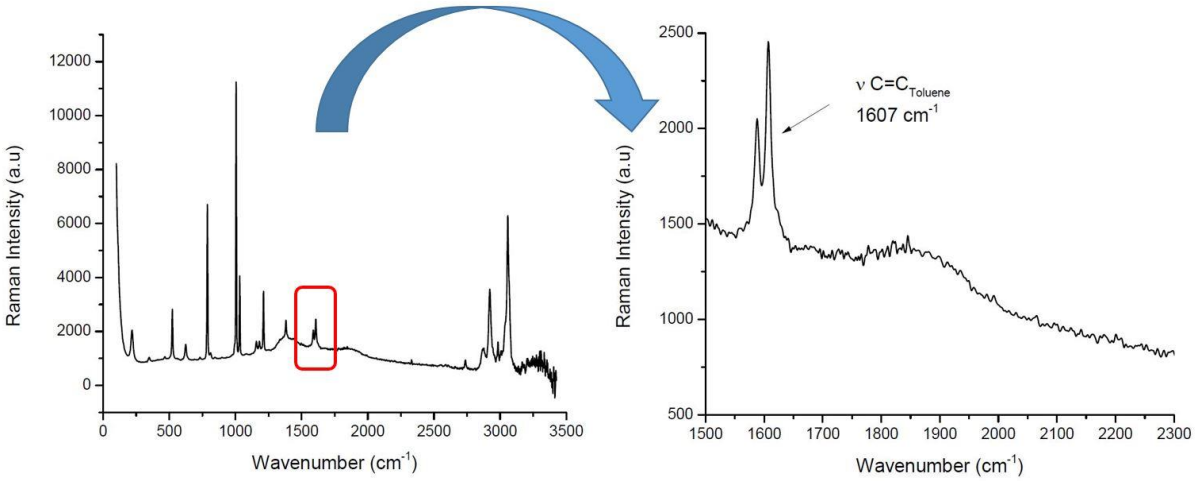

Figure 3.15. Signal optimisation on the stretching vibration of C=C of toluene in the Rheo-Raman-FTIR setup.

After optimising the signal on the stretching vibration of C=C of toluene, the solvent was replaced by the reaction mixture (TAS, BDSB, Toluene and Pt catalyst) and the experiment was launched again. However, it is common that the acquired Raman signals displayed a low signal to noise ratio as shown in Figure 3.16. The signal to noise ratio was so low that it was difficult to differentiate the triplet bands from the background noise. Consequently, the process of optimisation had to be repeated over again.

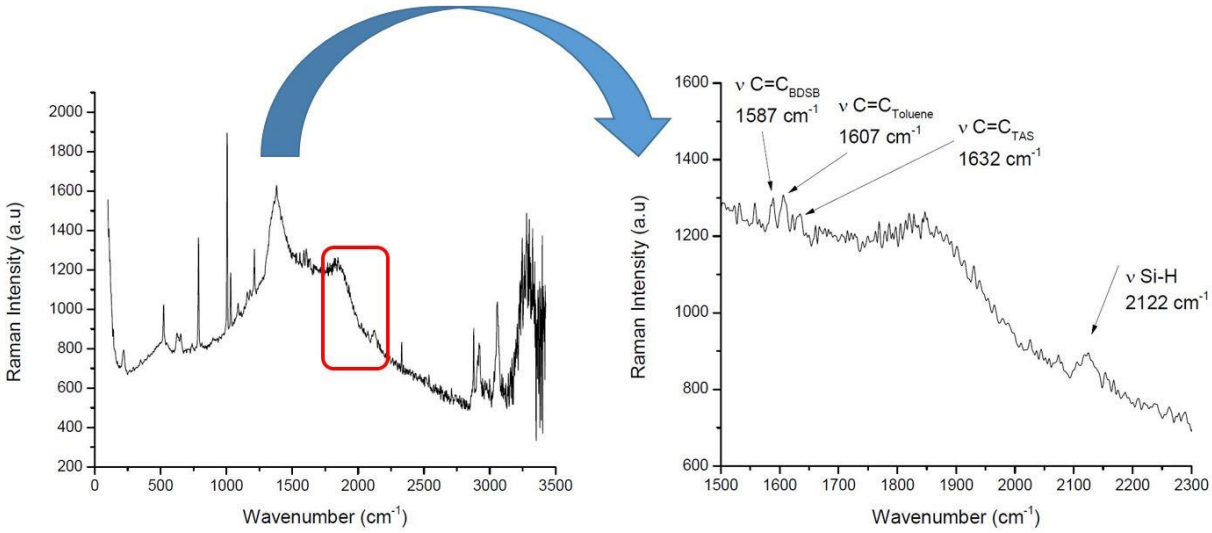

Figure 3.16. Raman spectra displaying low signal to noise ratio in the Rheo-Raman-FTIR setup.

After some attempts and by modifying the position of the lab-made Raman support, it appeared that signal to noise ratio was kept to a minimum when the 100 mm focal distance lens was position in an inclined angle with respect to the plate-plate geometry. From the region of interest (from 2300 to 1500 cm^{-1}), the triplet bands representing the stretching vibration of C=C of BDSB at 1587 cm^{-1}, C=C of toluene at 1607 cm^{-1} and the C=C of TAS at 1632 cm^{-1} together with the stretching vibration of Si-H at a higher wavenumber (2122 cm^{-1}) were distinctly illustrated in Figure 3.17. Consequently, the Raman data obtained from the coupling was exploitable and could be used to calculate the monomer conversion. Moreover, Figure 3.17 compared the Raman spectrum obtained at the start of the reaction with one, which showed no more evolutions. As expected, the stretching vibration of C=C of TAS at 1632 cm^{-1} as well as the stretching vibration of Si-H at 2122 cm^{-1} were consumed during the polymerisation reaction.

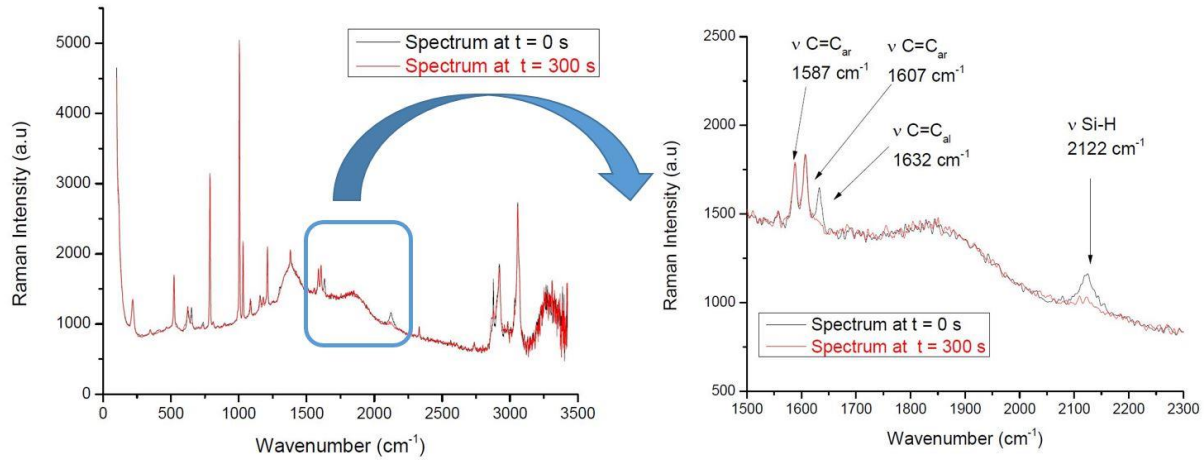

Figure 3.17. Raman spectra obtained after signal optimisation in the Rheo-Raman-FTIR setup.

Figure 3.18 represents the Raman spectra obtained from the Rheo-Raman setup (LRGP-Nancy). By qualitatively distinguishing the Raman spectra acquired from Rheo-Raman-FTIR setup (Figure 3.17) with the Rheo-Raman setup (Figure 3.18), it was noticed that the signal to noise ratio for the Rheo-Raman setup was lower than in the Rheo-Raman-FTIR setup. This was attributed to fact that the Rheo-Raman setup was not restricted in term of a gap distance since the laser beam could have probed any point on a 14 mL volume to obtain Raman information.

Moreover, in the case of the Rheo-Raman-FTIR setup the low signal to noise ratio was attributed to the gap distance (0.6 mm), and the interference caused from the metal material of the plate-plate geometry. However, the bands acquired in the area of interest (2300 to 1500 cm^{-1}) were satisfactory when compared to the ones obtained from the Rheo-Raman setup.

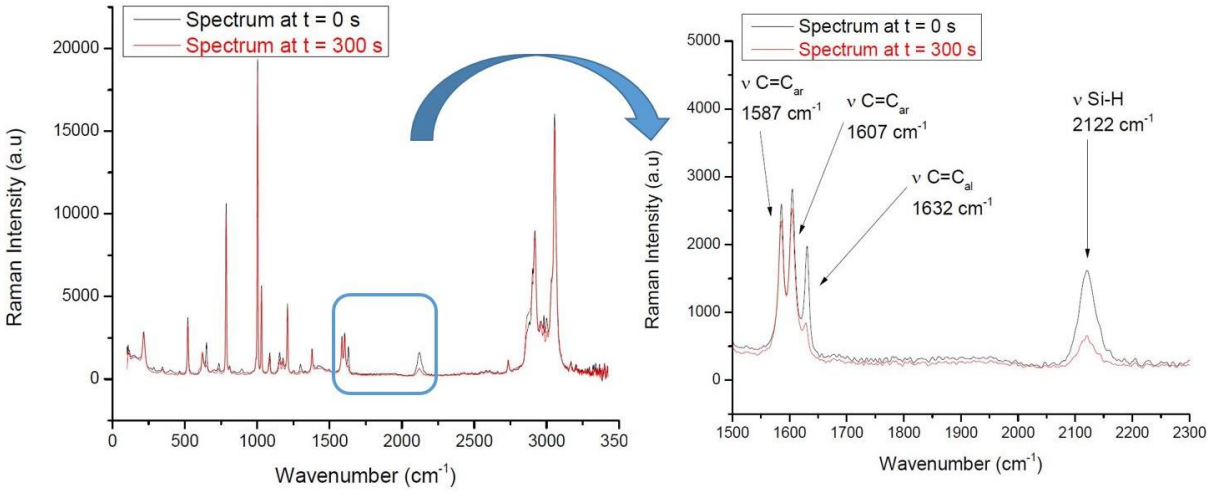

Figure 3.18. Raman spectra of the starting mixture (black line) and of the resulting polymer solution (red line) obtained from the Rheo-Raman setup.

Nevertheless, for the Rheo-Raman-FTIR setup to acquire bands with high intensity like in the Rheo-Raman setup, a compromise was needed between the exposure time and the amount of data collected. Hence, for the same reaction time, Rheo-Raman-FTIR gathered Raman data every 15 s (exposure time 10 s) while in the Rheo-Raman setup it was at every 5 s (exposure time 2 s). Furthermore, in the Rheo-Raman-FTIR setup, the rheometer and FTIR spectrometer collected data simultaneously, thus for every 30 s a rheological and FTIR data was being acquired. Therefore, after optimising the Rheo-FTIR-Raman setup in terms of gap, intensity of the Raman signal and data acquisitions, it was possible to monitor in real time the hydrosilylation reaction with predefined experimental parameters and conditions.

3.6.1. Uniformity of the reaction across the radius of the geometry

The study carried out by Darsy *et al.* reported the monitoring of a polycycloaddition by coupling the Rheo-FTIR setup [DA15]. A weak gel was obtained *i.e* G' remained less than G'' throughout the reaction. However, the authors carried out the experiment only at a single point at the lower surface of the sample. However, in our case, a weak gel was not reported and by taking advantage of the displacement of the rheonaut, an investigation about the homogeneity of the reaction across different positions of the geometry was performed. The Rheonaut system could be position at varying distances between the centre and a maximum of 45 mm due to the motor driven horizontal movement of the lower plate. Moreover, since the Rheonaut could move only to the left direction, only the left radius of the geometry was investigated. A set of points was attributed at different positions across the radius of the geometry. Four points were considered across the radius of the geometry namely P0 (= 0 mm), P1 (= 5 mm), P2 (= 10 mm) and P3 (= 15 mm) with each having a 5 mm distance from each other. The distance between the points was set at 5 mm since for values less than 5 mm the experiment had to be repeated several times which might prove to be counterproductive. While for a value greater than 5 mm, not enough data points would be collected to investigate properly the homogeneity of the reaction kinetics. P0 represented the moment where the ATR module and the centre of the geometry coincided (P0 = 0 mm) while P3 represented the ATR position at the edge of the plate-plate geometry (P =15 mm) as shown in Figure 3.19. A time dependent oscillatory test was performed with a frequency set at 35 Hz and a strain at 0.5.

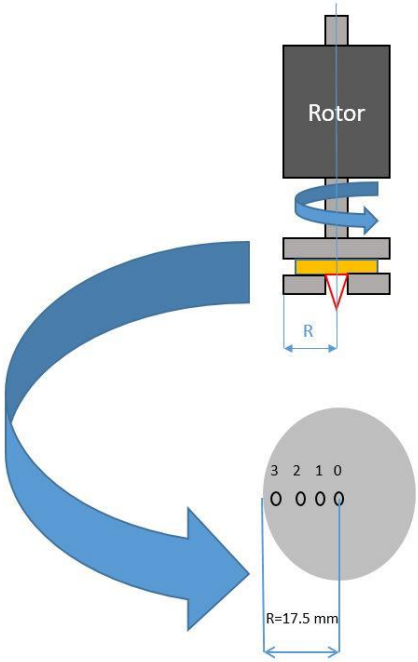

Figure 3.19. Representation of the different studied positions P0, P1, P2 and P3.

However, results obtained from P3 were disregarded due to the position of the diamond window which was at the limit of the geometry of the plate-plate configuration. Indeed, some of the sample was not in contact with the geometry. Thus, only position P0, P1 and P2 were considered for this study. Figure 3.20 represented the different alkene conversion at position P0, P1 and P2 calculated from the FTIR data. The data acquisition of the FTIR for P1 and P2 was carried out at every 30 s while at P0 it was collected at every 25 s.

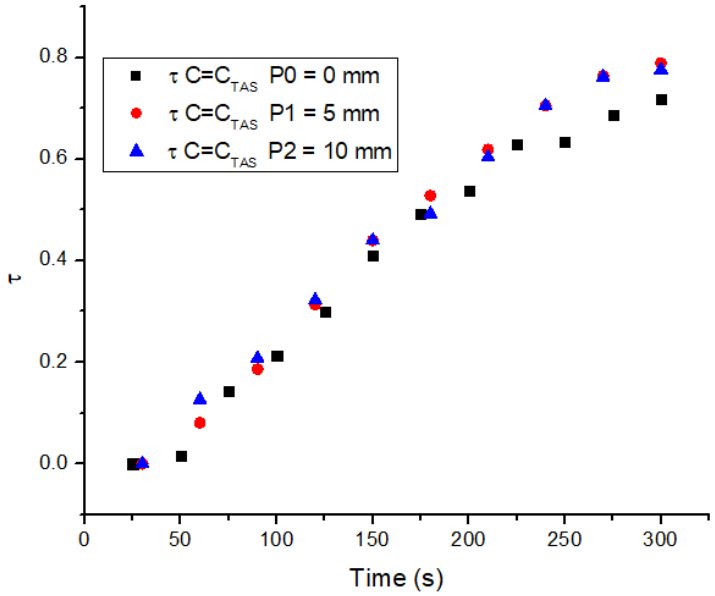

Figure 3.20. Alkene conversion obtained for P0, P1, and P2 from FTIR data.

It was observed that P1 and P2 data points superposed perfectly with each other. While P0 curve had a slight difference in comparison with P1 and P2 curves. However, the alkene conversion curves for all 3 positions had the same trend indicating that the reaction was homogeneous across the radius of the geometry. This finding was in accordance with a study carried out by Plog *et al.* who reported insignificant differences in crystallinity of polyethylene at different points from rim of the plate to the centre determined by the Rheo-Raman microscope setup [PL16]. Henceforth, the monitoring of the hydrosilylation reaction carried out at different position indicated the same kinetics reaction occurred across the radius of the geometry. In order to match the mixing of the reaction mixture by the magnetic stirrer in RBF, as from now on the rheological tests are carried out in steady state.

3.6.2. Impact of different catalyst concentrations on the polymerisation reaction

During the initial coupling studies carried out, it was observed that the gel turned into a solid state within 230 s for a catalyst concentration of 0.415 mmol·L^{-1}. This was further demonstrated by the sudden rise of the viscosity indicating a state change occurred during

the polymerisation reaction. By considering that the same outcomes would occur in RBF, it implied that sampling process could take place until around 230 s (the moment when the gel turned into a solid state). With the goal of increasing the reaction time of the polymerisation reaction as well as decreasing the effect of the sudden rise of viscosity, an investigation on the impact of different catalyst concentrations (C1 = 0.415 mmol·L^{-1}, C2 = 0.021 mmol·L^{-1}, C3 = 0.017 mmol·L^{-1}, and C4 = 0.014 mmol·L^{-1}) on the polymerisation reaction was carried out in a steady state test with a shear rate set at 35 s^{-1}. In this way, the idea would be to increase the sampling window for analysing the macromolecules formed during the hydrosilylation reaction of the reaction as well as slowing down the sudden rise of viscosity. Hence, four sets of polymerisation reactions were carried out where the only variable was the catalyst concentration. Figure 3.21 displays the viscosity plotted as a function of time at different catalyst concentrations. For each catalyst concentration, the derivative of the viscosity as a function of time was calculated to find out the maximum viscosity reached. For C1, C2, C3 and C4, a maximum viscosity of 5.54 Pa·s, 12.47 Pa·s, 9.88 Pa·s and 8.31 Pa·s were reported after a time of 300 s, 814 s, 1443 s and 2046 s respectively (indicated by the dotted line). Thus, it was noted that a decrease in catalyst concentration resulted in an increase of the reaction time of the polymerisation while the maximum viscosity reached was within the same range each time for C1-C4.

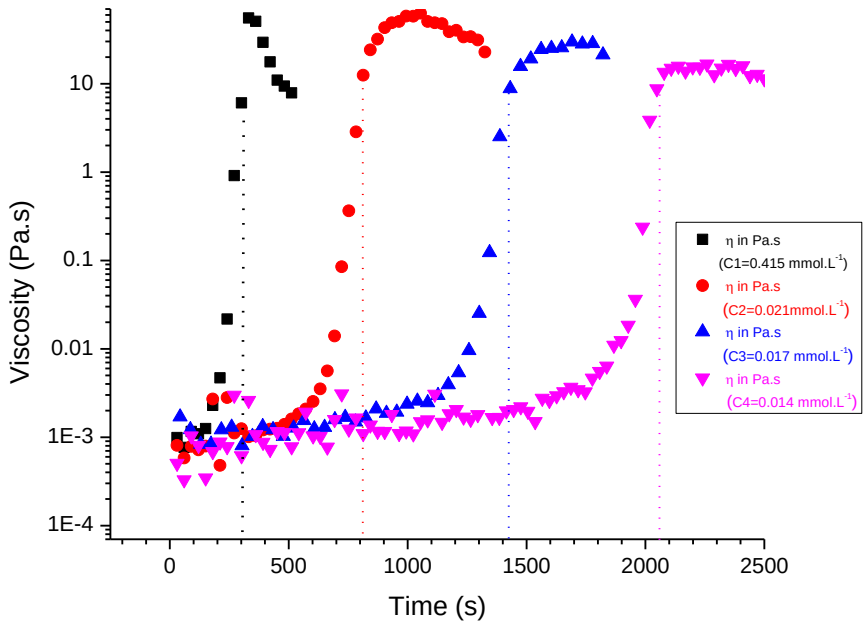

Figure 3.21. Effect of concentration of catalyst on polymerisation reaction.

Moreover, it was observed for all the different catalyst concentrations, the viscosity remained constant during the initial stages of the polymerisation reaction before the sudden

rise in viscosity was noticed. Therefore, although the decrease in catalyst concentration did increase the reaction time of the polymerisation, the liquid-solid gel transition time was the same in all cases - independent of the catalyst concentration. Consequently, lowering the catalyst concentration would not result in increasing the sampling process window in RBF since the catalyst concentration did not influence the sudden increase of viscosity. Thus, there was no use to change the catalyst concentration that have been used until now. Henceforth, the monitoring of the hydrosilylation reaction was carried out with a catalyst concentration of 0.415 mmol·L^{-1}.

3.6.3. Monitoring the reaction kinetics *via* the optimised Rheo-FTIR-Raman setup

After optimising the Rheo-Raman-FTIR setup in terms of gap, intensity of the Raman signal, impact of catalyst concentration and the homogeneity of the reaction across the geometry, an experiment was launched to monitor in real time the hydrosilylation reaction. However, the polymerisation reaction that will be carried out in RBF will be stirred at 4.5 s^{-1} to ensure homogenous mixture of the reagents mixture. Since the Raman spectrometer had to link the monomer conversion occurring in RBF to that of on the rheometer, the shear rate was changed from 35 s^{-1} to 4.5 s^{-1} to match approximately the frequency of rotation of the magnetic stirrer. Hence, the *in-situ* monitoring of the hydrosilylation reaction was performed in steady state with a shear rate of 4.5 s^{-1}. Moreover, the experimental parameters were set to acquire more FTIR and rheological data, thus for each 17 s a data point was acquired for both FTIR and rheology while for Raman spectroscopy for each 15 s a Raman information was being gathered. The coupling results of the polymerisation reaction was shown in Figure 3.22. The alkene conversion calculated from Raman and FTIR data showed an identical trend suggesting that the same reaction kinetics occurred at the lower surface of the ATR and at the centre of the sample. Thus, further validating the fact that the reaction occurring across the plate-plate configuration was homogeneous.

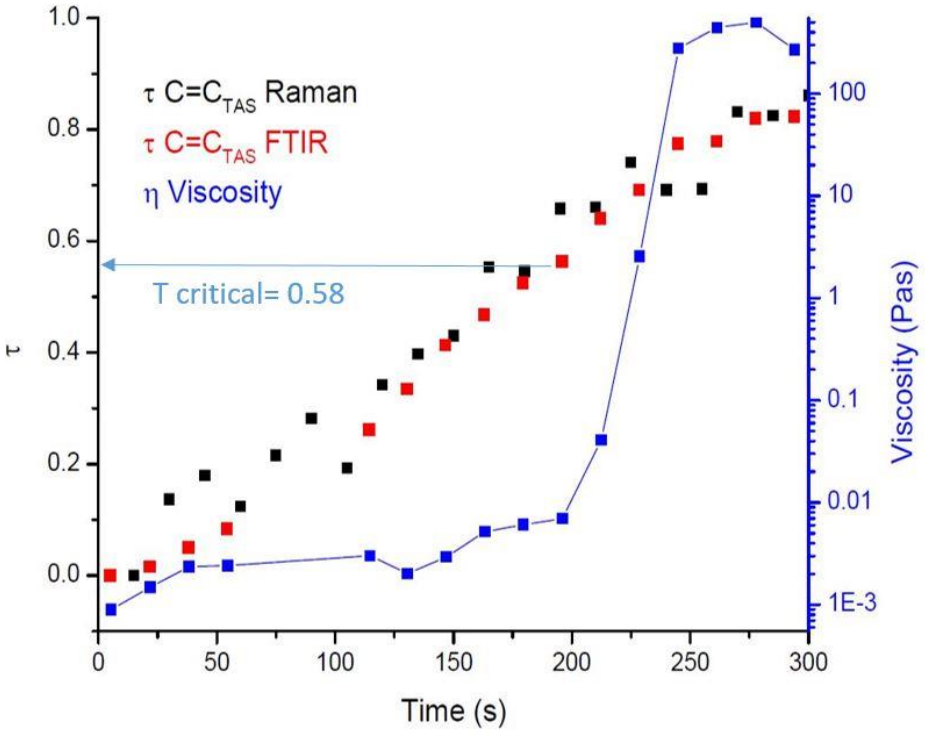

Figure 3.22. Coupling results of the Rheo-Raman-FTIR in the Plate-Plate configuration.

It was observed that around 80 s, both the rheology and the FTIR data were missing a point data. This was attributed to the slight delay of the Rheonaut module to adapt to the sudden increase of the temperature due to the exothermic reaction. The experiment was repeated by increasing the ΔT to $\pm\ 30\ °C$. However, the rheology and FTIR point data around 80 s were still missing while Raman data were acquired continuously around this region. As expected, the viscosity remained constant during the initial moments, before increasing rapidly to reach a maximum viscosity, this rapid change of viscosity was associated to a state change from liquid to a solid gel. It was observed that only after the calculated critical conversion of 0.58 that the macromolecules network had an influence on the rheology of the polymer. Monitoring macromolecular structures (average molar mass, conformation etc.) as a function of time would provide important additional information for understanding the impact of the polymer structure on their rheology.

However, even if promising results were obtained, combining the Raman spectrometer to the existing Rheo-FTIR setup was not a straightforward task. The Raman spectrometer had to work jointly with the Rheo-FTIR setup by taking into consideration the possible experimental restrictions that might arise. In our case, the main restrictions that the Rheo-FTIR Raman posed was in terms of the selected gap distance and intensity of the Raman signal as discussed in section 3.5. Despite all the experimental restrictions, the Rheo-Raman-FTIR setup worked in perfect synchronisation with each other as it has been

demonstrated. Therefore, the Rheo-Raman-FTIR setup helped in achieving an *in-situ* monitoring of a hydrosilylation reaction and enabled the correlation between the kinetics of polymerisation and rheological behaviour of preceramic polymer.

3.7. Conclusion

The monitoring of the hydrosilylation reaction in real time was initially performed by the Rheo-FTIR setup by starting with defined monomers. A *hb*-PCS was synthesised with a 94 % yield, from di and tetrafunctional monomers, using a hydrosilylation reaction, with Karstedt's catalyst. The thermal behaviour of this polymer featured classic characteristic for SiC preceramic macromolecules with a series of four stages during the pyrolysis process under argon atmosphere. The resulting pyrolysed product at 1400 °C announced a highly porous microstructure, which could have interesting properties in terms of catalysis. Interesting results were obtained as the rheological moduli could be correlated to the alkene conversion from FTIR spectrometer. However, the possibility of a difference in the polymer growth was suspected between the diamond window of the ATR and inside the sample. Thus, the existing Rheo-FTIR setup was equipped with a Raman spectrometer to overcome the shortcomings of the Rheo-FTIR setup. The Raman spectrometer allowed the sample to be probed with a better penetration depth. Moreover, we took the advantage of the complementarity of the two vibrational techniques to perform a structural analysis of the sample. It was the first time that a Raman spectrometer was attached to a Rheo-FTIR devise.

However, based on literature, the Rheo-Raman setup was used to monitor free radical polymerisation and succeeded in correlating the structural changes with the rheological changes. Hence, a preliminarily experiment was carried out on an existing Rheo-Raman setup. The results obtained were used as a reference as it was not obvious to optimise the

intensity of the Raman signal given the restriction of the selected gap distance on the Rheo-FTIR-Raman setup. Eventually, a good spectrum was obtained from the Raman spectrometer after the optimisation the experimental conditions and parameters on the Rheo-FTIR-Raman setup.

By correlating the rheological data with the FTIR and Raman data, it was found that the viscosity was not affected during the beginning of the hydrosilylation reaction although the alkene conversion increased rapidly. It was only after a critical alkene conversion of 0.58 that the viscosity increased rapidly. Under the critical alkene conversion, the macromolecules were not developed enough to have an impact on the viscosity of the medium.

This finding was a first step in understanding the relationship between the kinetics of the polymerisation and the rheological behaviour. The development of the Rheo-FTIR-Raman setup is an innovation for monitoring real time polymerisation reaction as it provides an analysis of the molecular structure of the analysed sample and constitutes an important aspect in understanding the fundamental study of the rheology of preceramic polymers. However, the monitoring macromolecular structures in terms of molar mass, root mean square radius (RMS radius) would provide addition information for understanding the impact of the polymer architecture on their rheology. Therefore, the polymer solution had to be characterised by the SEC-MALS to obtain addition information about the structures of the macromolecules formed during the hydrosilylation reaction.

Chapter 4.

Monitoring of the macromolecular structures and their impact on the rheological behaviour of the preceramic polymer

4.1. Introduction

The third chapter has illustrated the relationship between the kinetics of the polymerisation reaction and the rheological behaviour of the preceramic polymer. However, to fully understand the impact of the structure of the macromolecules on the viscosity, an analysis of the macromolecules in terms of average molar mass, size (Root Mean Square radius) and conformation (molecular structures - rod, random coil or spheres) was necessary. This was possible *via* a Size Exclusion Chromatography (SEC) coupled with a Multi-angle Light Scattering (MALS). The SEC-MALS coupling made up the second part of the platform (Figure 4.1) together with an immersion probe used to monitor in real time the polymerisation reaction in a round bottom flask (RBF). The goal of this chapter was to synchronise the reaction kinetics obtained from RBF to that carried on the rheometers, *via* the alkene conversion to facilitate the correlation of the viscosity of the medium to the average molar mass of the preceramic polymer. This would enable a better understanding and control of the macromolecular growth and future shaping processes. First, chapter 4 would deal with the optimisation of the sampling process during the polymerisation reaction in RBF. Secondly, the collected samples would be characterised *via* the SEC-MALS coupling and the results in terms of molar mass, cumulative molar mass distribution and conformation of the structure of the polymer will be reported. Finally, the results of the correlation of the average molar mass with the viscosity of the medium *via* the alkene conversion would be presented.

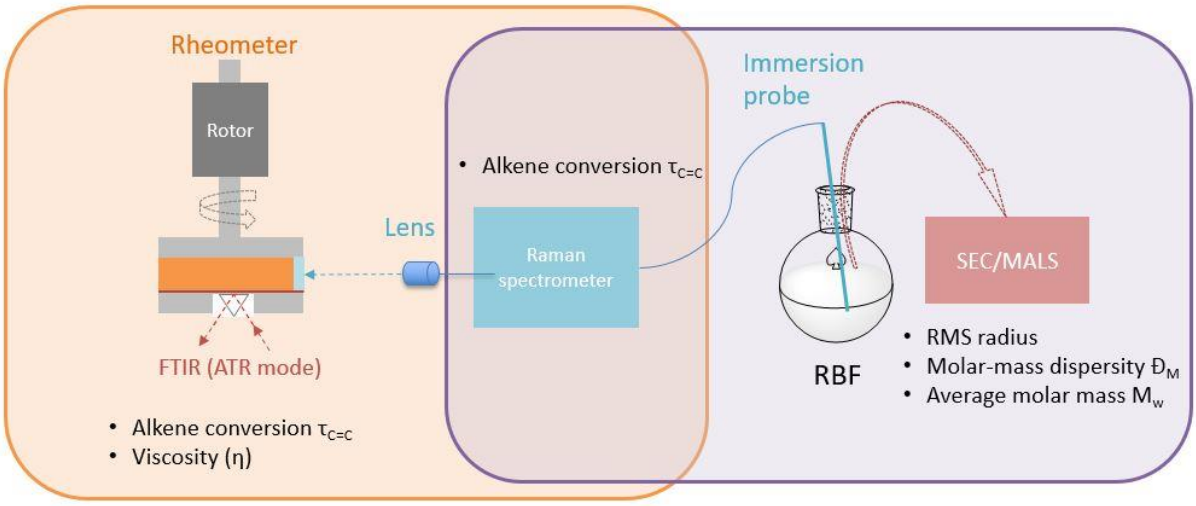

Figure 4.1. Platform with particular emphasis on the second part of the setup.

4.2. Optimisation of the sampling process during the polymerisation reaction

Before optimising the sampling process of the kinetics reaction, it was important to define the experimental conditions of the polymerisation process carried out in RBF. Figure 4.2 represents the experimental setup used to carry out the hydrosilylation reaction.

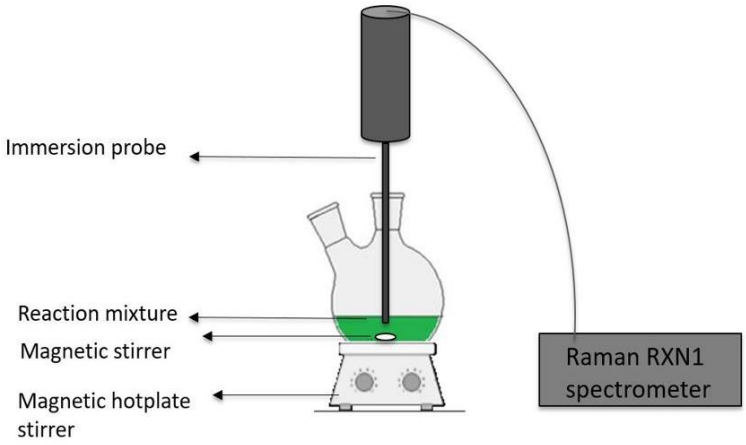

Figure 4.2. Experimental setup of polymerisation reaction in round bottom flask (RBF).

The polymerisation reaction that occurred in between the plate-plate geometry of the rheometer was repeated in RBF by keeping the same concentration of reagents. The reaction mixture could not be sampled from the rheometer during the polymerisation reaction while in RBF sampling could be performed *via* one of the necks of the round bottom flask. The polymerisation reaction was carried out at room temperature.

As mentioned in chapter 2, the same Raman spectrometer RXN1 (Kaiser optical System) that was used on the Rheo-FTIR-Raman setup was employed on the RBF. The only difference was that an immersion probe (length of 15.3 cm and a diameter of 0.64 cm) was used instead of a lens with a focal distance of 100 mm. The tip of the immersion probe was completely plunged inside a 5 mL reaction mixture. The data acquisitions were carried out with an exposure time of 2 s and a current interval of 10 s. The magnetic stirrer was set at 4.5 Hz during the polymerisation to ensure a homogeneous mixture of the reaction reagents and to match the shear rate applied on the rheometer.

The sampling process was accomplished during the *in-situ* polymerisation reaction. The sampled polymer solution was immediately quenched by inserting 100 µL polymer solution sampled in a 10 mL graduated flask containing about 9 mL of toluene. This was followed by adding more toluene until a total volume of 10 mL was reached. Sampling could be performed solely until 230 s as beyond that point a solid gel was formed. In addition, it

was verified that sampling process did not have any impact on the Raman signal during the real-time monitoring of the polymerisation reaction.

The hydrosilylation reaction was performed three times and each time a new sampling window was defined to optimise the sampling process. The different sampling windows have been established by letters A (first experiment), B (second experiment) and C (third experiment). Figure 4.3 showed the alkene conversion obtained from the Raman spectroscopy as a function of time from the third experiment.

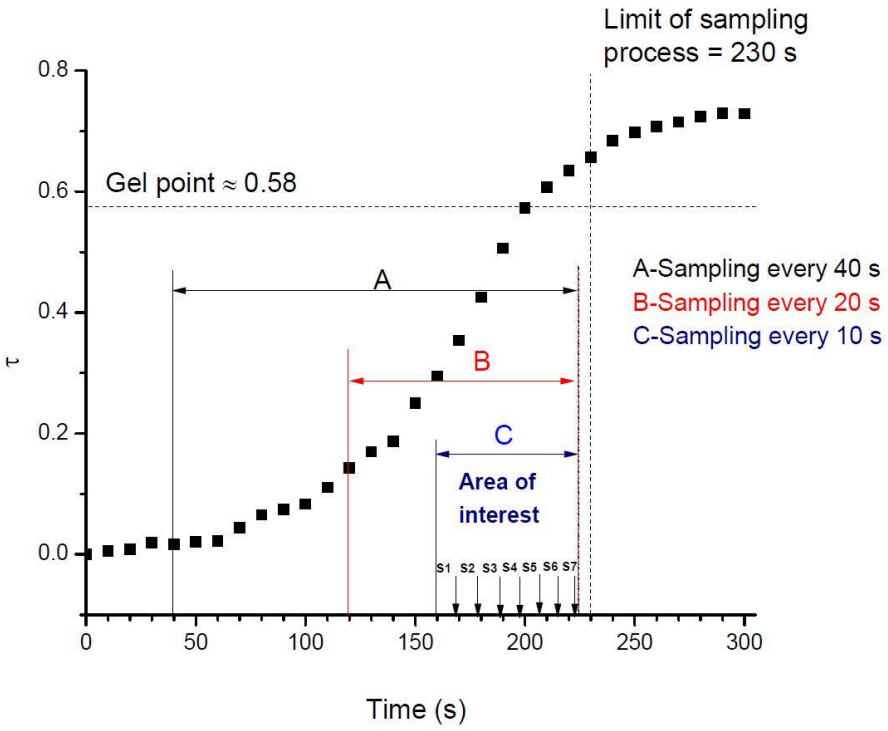

Figure 4.3. Determining sampling window from the alkene conversion versus time graph.

One of the difficulties encountered during the sampling process in window A was that the samples collected registered a weak MALS signal, as the mass of the molecules were not significant enough. Thus, to overcome this issue, it was decided to increase the amount of polymer solution collected from 100 µl to 300 µl and to define a sampling window near the limit of sampling process. However, even with those changes, a weak MALS signal was registered for the initial samples collected from sampling window B. Consequently, the sampling window was further reduced from 120-223 s (sampling window B) to 160-226 s (sampling window C). A sufficient MALS signal was registered for all the samples collected in sampling window C as the macromolecules were already in advanced stages of the polymerisation reaction.

Table 4.1 summarises the optimal conditions for the sampling process of the polymerisation reaction. Since the sampling window was reduced from A to C, the sampling

rate within the sampling window C was increased with the aim of obtaining a maximum number of points. As reported in Table 4.1, a total number of seven points have been collected for C with the last point collected at 226 s. By the time the 8th sampling was performed, the gel was already in solid form. Thus, the seven sampling points collected from sampling window C were named Si (i from 1 to 7).

Subsequently, the samples collected from C would be characterised by the SEC-MALS coupling. This would allow for a better understanding of the evolution of the structure of the macromolecules during the polymerisation reaction especially in terms of molar mass, size, and molar-mass dispersity.

Table 4.1. Summary of conditions in optimising the sampling process during the reaction.

Sampling window	Volume sampled	Sampling window time	Sampling occurred every	No of points collected
A	100 µL	40-226 s	40 s	6
B	300 µL	120-223 s	20 s	6
C	300 µL	160-226 s	10 s	7

4.3. Characterising the hyperbranched polycarbosilanes in terms of molar mass, RMS radius and molar-mass dispersity *via* the coupling SEC-MALS

The seven sampling points were analysed individually *via* the SEC-MALS coupling. However, before starting the analysis it was primordial to determine the specific refractive index increment also known as dn/dc that illustrated the change of the refractive index of a polymer with respect to the concentration of the solute [CO07]. The dn/dc occurs in the optical constant K^* (equation 4.2) and is required to determine the absolute concentration of polymer molecules in the MALS detectors. Hence, in our case, a dn/dc value of 0.0592 mL·g^{-1} was determined from the polymer solution and was used to access the average molar mass, molar mass dispersity and the conformation of the sampled polymer solutions [PO11]. As mentioned in chapter 2, the light scattering principles are embodied in the Rayleigh-Gans-Debye equation:

$$R(\Theta) = K^* McP(\Theta)[1 - 2A_2 McP(\Theta)], \qquad \text{Eq. (4.1)}$$

where $R(\Theta)$ is the excess (i.e., from the solute alone) Rayleigh ratio. The ratio of the scattered and incident light intensity, corrected for size of scattering volume and distance from scattering volume.

$$K^* = \frac{4\pi^2 n_0^2}{N_A \lambda_0^4}\left(\frac{dn}{dc}\right)^2 \qquad \text{Eq. (4.2)}$$

n_0 – solvent refractive index, λ_0 – vacuum wavelength of incident light, c is the solute concentration in g·mL^{-1}, θ is the scattering angle.

The data acquired from the MALS detectors were investigated with the ASTRA software (version 7.3.2) using either the Zimm fit method or the Berry fit method [KI09]. The Zimm fit was the most favoured method for the analysis of light scattering data and was normally applied for mid-sized molecules while Berry fit was employed for large molecules [BE01] [YU05]. Hence, the Zimm fit method was applied for samples 1 to 6 and the Berry fit method was applied for sample 7. The results obtained for the seven sampling samples would be demonstrated in Figures 4.4, 4.5 and 4.6.

Figure 4.4 displayed the elution time and the molar mass of the seven sampling solutions. The separation of the molecules was carried out by the SEC based on size (hydrodynamic radius) [SU04]. It could be observed from Figure 4.4 that S1 had the lowest molar mass ranging from 10^2 to 10^4 g·mol^{-1} with a retention time around 8 min while the highest molar mass was noticed in S7 ranging from 10^5 to 10^8 g·mol^{-1} with a retention time of 5.5 min.

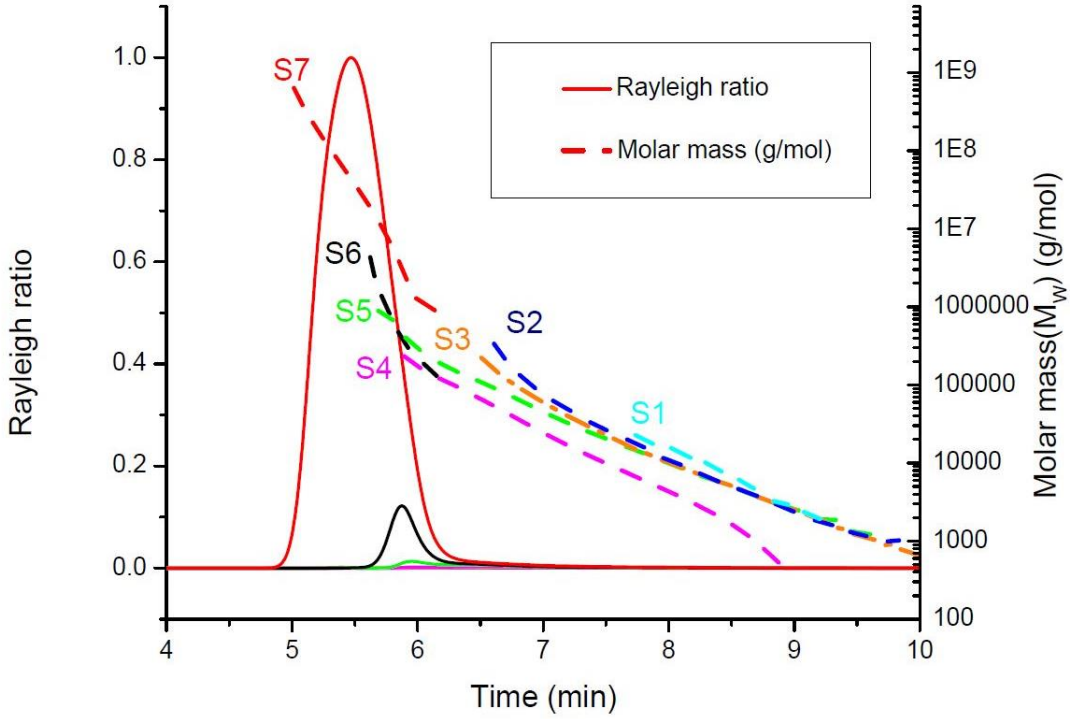

Figure 4.4. SEC elution patterns plots of the samples (S1-7) versus time. The x-axis represents the elution time of the polymer solution. The left-y axis illustrates the Rayleigh ratio which is an indication of the passage of the macromolecules while the right-y axis displays the calculated molar mass of the samples (S1-7).

Moreover, S1 possessed mostly oligomers as S1 was sampled during a stage of the step-growth polymerisation reaction where the structure of the macromolecules were not

developed enough. As the polymerisation reaction progressed, the molar mass registered for S2-4 did not differ too much from each other as they were all in the range of 10^2 to 10^5 g·mol^{-1}. The sampling solutions S2-4 were mostly macromolecules that were still under construction. Furthermore, S5 possessed molar mass ranging from 10^3 to 10^6 g·mol^{-1} with the first visible peak on the chromatogram having a retention time of 5.9 min. In addition, S5 revealed the intensification of the crosslinking of the macromolecules, thus representing the progression of the polymerisation reaction towards a fully formed hyperbranched polymer.

Moreover, S6 had mostly large macromolecules with molar mass varying from 10^4 to 10^7 g·mol^{-1} with a retention time of 5.8 min. Finally, S7 registered the highest molar mass with a sharp and intense chromatogram signal with a retention time around 5.5 min. S7 was sampled just moments before the gel turned into a solid, thus it was expected that S7 would have a molecular structure that was hyperbranched at this stage of the polymerisation reaction. In addition, it is worth mentioning that the quenching of the polymer solution was efficient as the same dispersion observed in Figure 4.4 was reported one hour after upon a second analysis of the seven samples.

Figure 4.5 represented the cumulative molar mass distribution of the collected samples. The cumulative molar mass distribution enables an easy determination of weight fraction polymer in a specific molar mass domain. It was used to determine the molar mass maximum and minimum as well as the molar mass most abundant fractions [PO11]. In addition, it was an interesting way of following the kinetics evolution of the hydrosilylation reaction as the cumulative molar mass distribution intensifies the effect of molar mass of the samples in comparison to Figure 4.4.

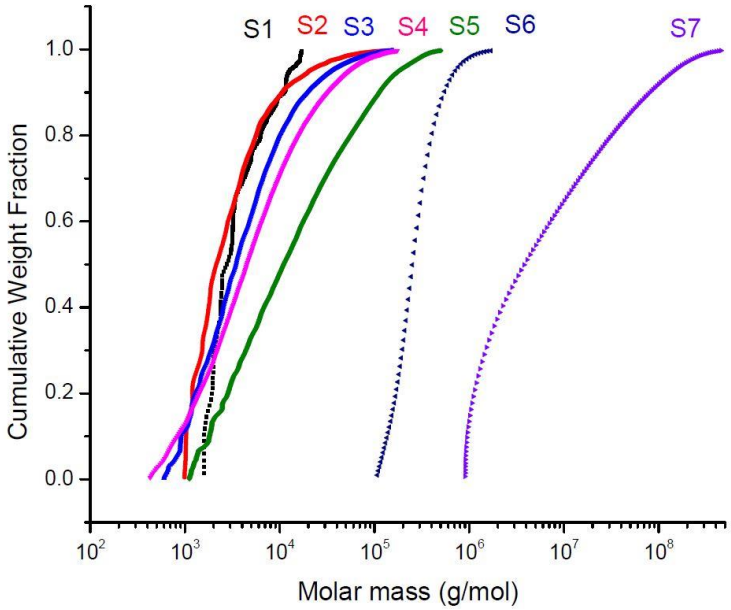

Figure 4.5. Cumulative molar mass distribution curve.

The cumulative molar mass distribution of S1 had most of its weight fraction polymer within the domain of 10^3 to 10^4 g·mol^{-1} with the maximum being 17574 g·mol^{-1} and the minimum being 1614 g·mol^{-1}. The cumulative molar mass distribution of S1 indicated a moderate molar–mass dispersity ($Đ_{M1}$ = 1.56), thus showing that around 163 s, oligomers were being formed. S2-S4 had most of its cumulative molar mass distribution ranging from 10^3 to 10^5 g·mol^{-1}. Furthermore, S2-S4 had a broader molar-mass dispersity ($Đ_{M2}$ = 2.87, $Đ_{M3}$ = 3.86, $Đ_{M4}$ = 5.37) than S1 as at that moment of the polymerisation reaction, the distribution of the molar mass of the macromolecules started to be more dispersed. However, even if the macromolecules were in continuous development, they were interconnecting moderately with each other.

Meanwhile S5 represented the transition cumulative molar mass that started above a molar mass of 10^3 g·mol^{-1} and stretched until 10^5 g·mol^{-1}. S5 was sampled at 206 s and according to its molar-mass dispersity ($Đ_{M5}$ = 7.81), macromolecules present at that moment possessed a wide range of molar mass. Moreover, S6 recorded the smallest molar-mass dispersity ($Đ_{M6}$ = 1.35) with the smallest domain of molar mass of 10^5 to 10^6 g·mol^{-1}. This sudden decrease in molar-mass dispersity could be accounted by the fact that all macromolecules at this moment had approximately the same range of molar mass before starting to interlink with each other.

Finally, the last sample point S7 had the broadest domain of cumulative molar mass distribution varying from 10^6 to 10^8 g·mol^{-1}. In addition, it had also the largest molar-mass dispersity ($Đ_{M7}$ = 11.48) implying that the macromolecules were being connected to their neighbours forming newer larger macromolecules. Therefore, the seven samples have been analysed in terms of their molar mass and molar-mass dispersity.

Table 4.2 summarised the SEC-MALS analysis of the seven sampling points (S1-S7) with their sampling time, average molar mass ($\overline{M}_w$), molar-mass dispersity ($Đ_M$) and fit method.

Table 4.2. SEC-MALS analysis results of the sampling samples.

Sample number	Sampling time (s)	Fitting method	$\overline{Mw}$ (g·mol^{-1})	$Đ_M$ (-)
S1	163	Zimm	4386	1.56
S2	173	Zimm	5885	2.87
S3	183	Zimm	8984	3.86
S4	193	Zimm	31080	5.37
S5	206	Zimm	40230	7.81
S6	216	Zimm	320200	1.35
S7	226	Berry	28200000	11.48

The sampling time corresponded to the points sampled within the sampling window C. For S1-6 the average molar mass increased steadily from 4386 g·mol^{-1} to 320200 g·mol^{-1} before registering a rapid increase of nearly 2 orders of magnitude for the last sample (S7) as the crosslinking was more consequent around 216 s. In parallel, the molar-mass dispersity increased from 1.56 to 11.48 as the polymerisation reaction progressed. However, S6 reported a sudden decrease in molar-mass dispersity that could be attributed to the crosslinking of macromolecules leading to polymer networks having the same molar mass. Since the SEC-MALS coupling has characterised the samples in terms of average molar mass and molar mass dispersity, it would be interesting to obtain information about the conformation of the polymer as well.

During the SEC-MALS analysis, simultaneous measurements of RMS radius and molar mass give information about the polymer chain conformation by plotting the log of RMS radius versus log of molar mass as shown in Figure 4.6. S1-4 were not represented in Figure 4.6 since their RMS radius were less than 10 nm. Normally, when the RMS radius are less than 10 nm, it is difficult to access suitable data from their conformation plot. The slope of the conformation plot of the polydisperse samples could be classified into three categories namely: i) rod with a slope = 1, ii) random coil with slope in between 0.5 - 0.6, iii) sphere (characteristics of hyperbranched polymer) with slope in between 0.3 - 0.4 [PO02] [PO19].

Random coil structures are typically an indication of linear polymers, whereas sphere like molecular structures are an evidence of hyperbranched molecules. According to Figure 4.6, S5 was classified as a random coil conformation with a plot of 0.63 while S6 and S7 were considered, as spheres (hyperbranched structures) since their conformation plot slope were 0.36 and 0.41 respectively.

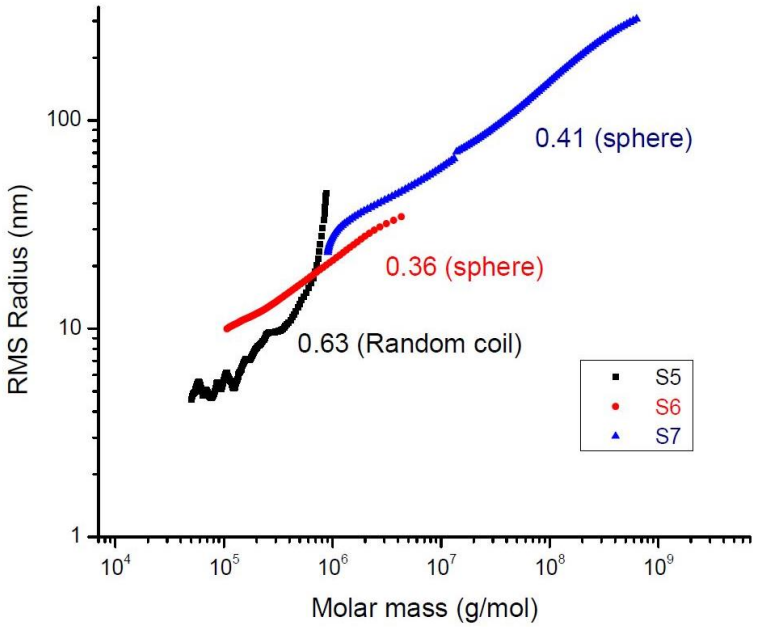

Figure 4.6. Conformation plots of samples S5-S7.

The seven sampling points were successfully characterised by the SEC-MALS coupling providing important information about the average molar mass, the molar-mass dispersity and conformation of the growing polymers. Therefore, a better understanding of the impact of the macromolecules on the rheology of the medium would be possible by correlating these findings with the reaction kinetics of the hydrosilylation reaction. However, before correlating the data obtained from different characterisation techniques of the devised platform, it was important to correlate the alkene conversion obtained in RBF with the Rheo-Raman-FTIR setup.

4.4. Linking the reaction kinetics occurring across the platform

The reaction occurring on the Rheo-Raman-FTIR setup was correlated to the reaction occurring in RBF *via* the alkene conversion obtained from both setups. This was possible as the polymerisation reaction occurred across both setups had the same concentration of reagents and same experimental conditions. To fully understand and to better control the macromolecular growth of preceramic polymer, a mathematical model was applied to the alkene conversion curves so that the conversion data were linked in a continuous manner. Hence, suitable functions were applied to the alkene conversion obtained from the platform (Rheo-Raman-IR setup and in RBF). Among them, the SRichards2 sigmoidal model, which is used as a growth model, was selected [HO22]. It fitted well the alkene conversion curve with a regression of 0.999 as shown in Figure 4.7.

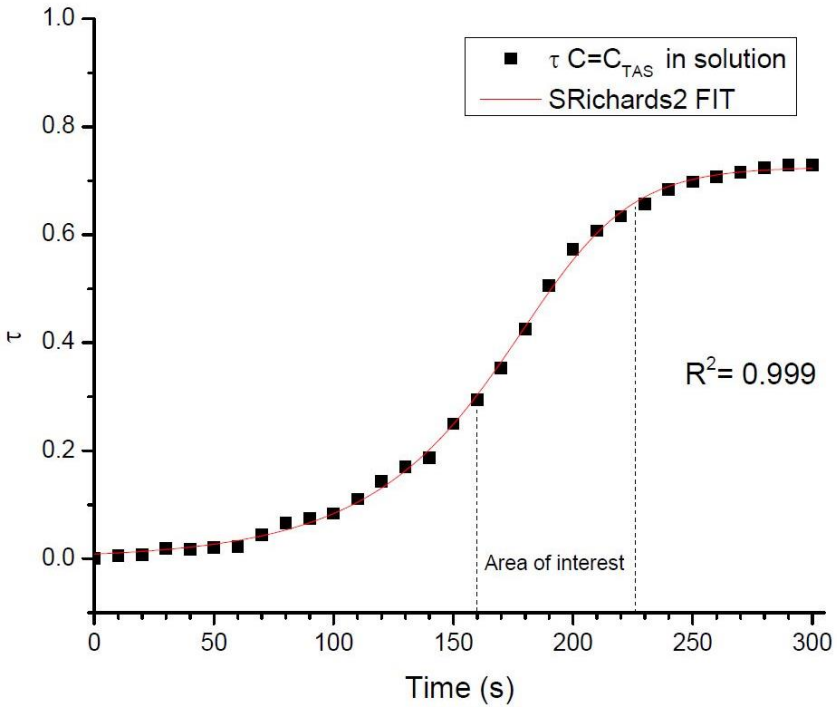

Figure 4.7. SRichards2 function applied to the alkene conversion in RBF.

The SRichards2 sigmoidal function can be expressed as:

$$\tau = a[1 + (d-1)e^{-k(t-xc)}]^{\frac{1}{(1-d)}}, \qquad \text{Eq. (4.3)}$$

where: a = 0.72 (top asymptote); xc = 179.2 (centre); d = 3.12 (constant parameter); K = 0.05 (constant parameter).

The kastedt's catalyst contain small amount of oxygen which when mixed with the reaction mixture, led to the formation of nanoparticles. The oxygen present in the catalyst helped in keeping the size of the nanoparticles. The nanoparticles act as colloidal, which increase the kinetics of the reaction. After an induction period, an extremely fast reaction occurred with a high turnover number. Normally, the sigmoidal curve is an indication of a reaction of catalysis by nanoparticles [VR12].

The SRichards2 sigmoidal curve could be associated with the phenomenon occurring during the hydrosilylation reaction [SA01] [HO22]. The slow increase observed at the beginning of the reaction could be linked to the induction period whereby the formation of nanoparticles in the reaction mixture is taking place. A rapid increase in the alkene conversion indicated that the rate of reaction has increased due to the high turnover of the catalysis. Ultimately, the SRichards2 curve stabilised as the reactants were less available due to steric hindrance occurring during the polymerisation reaction. Therefore, since the SRichards2 sigmoidal function suited the phenomenon occurring during the hydrosilylation

reaction, it was applied to the other alkene conversion curves obtained from the Rheo-Raman-IR setup as shown in Figure 4.8.

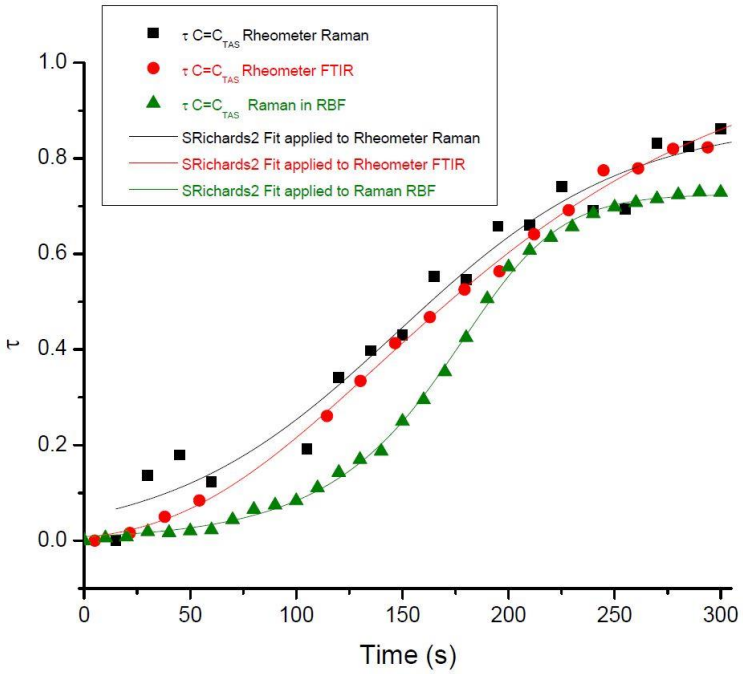

Figure 4.8. Alkene conversion obtained from the platform (Raman and FTIR spectroscopy).

The alkene conversion in RBF had more data points than the one obtained from the Rheo-Raman-IR setup. This was because in the Rheo-Raman-FTIR setup a compromise between a good signal and the number of data points acquired during the polymerisation reaction was made due to the small volume being probed while in RBF a good signal was obtained from start since the immersion probe was in direct contact with the reaction mixture. Moreover, qualitatively the spectrum obtained from the Raman lens had a higher noise ratio in contrast to the immersion probe. For these reasons, the alkene conversion obtained from the immersion probe was used as a reference.

Moreover, it was noticed that the alkene conversion curves obtained from the Rheo-Raman-FTIR setup (*i.e.* the FTIR and Raman alkene conversion) have the same trend. Any one of the two curves could have been used to correlate the reaction kinetics occurring from the Rheo-Raman-FTIR setup to the alkene conversion obtained from RBF. However, since Raman data obtained from the Rheo-Raman-FTIR setup were slightly more dispersed than the FTIR data, it was envisaged to use the FTIR alkene conversion.

In addition, it was observed that the alkene conversion from RBF had a similar trend as the one obtained from the Rheo-FTIR-Raman setup but with a slightly different rate of reaction. A plausible explanation might be the oscillation effect on the polymer solution was different even though the shear rate from the rheometer matched the speed of rotation of the

magnetic stirrer. Despite this difference in oscillation effects, the results could still be correlated *via* the alkene conversion.

The curves of the alkene conversion from both setups were correlated by applying the SRichards2 sigmoidal function. Consequently, the alkene conversion from the RBF corresponded to any data point at any given time of the alkene conversion of the FTIR data, thanks to the applied function.

4.5. Relationship between molar mass, alkene conversion and viscosity of reaction medium

The last step of this chapter was to link the viscosity of the reaction medium with the average molar mass of the collected sample *via* the alkene conversion. Figure 4.9 illustrated the coupling results from the Rheo-Raman-FTIR setup combined with the reference alkene conversion obtained from RBF. Since the synchronisation of the reaction kinetics from both setups was achieved, each point of the alkene conversion from RBF could be correlated to a viscosity value obtained from the Rheo-FTIR-Raman setup. Thus, at any moment in time, we could deduce the viscosity value for a corresponding alkene conversion value and linked the latter to its average molar mass.

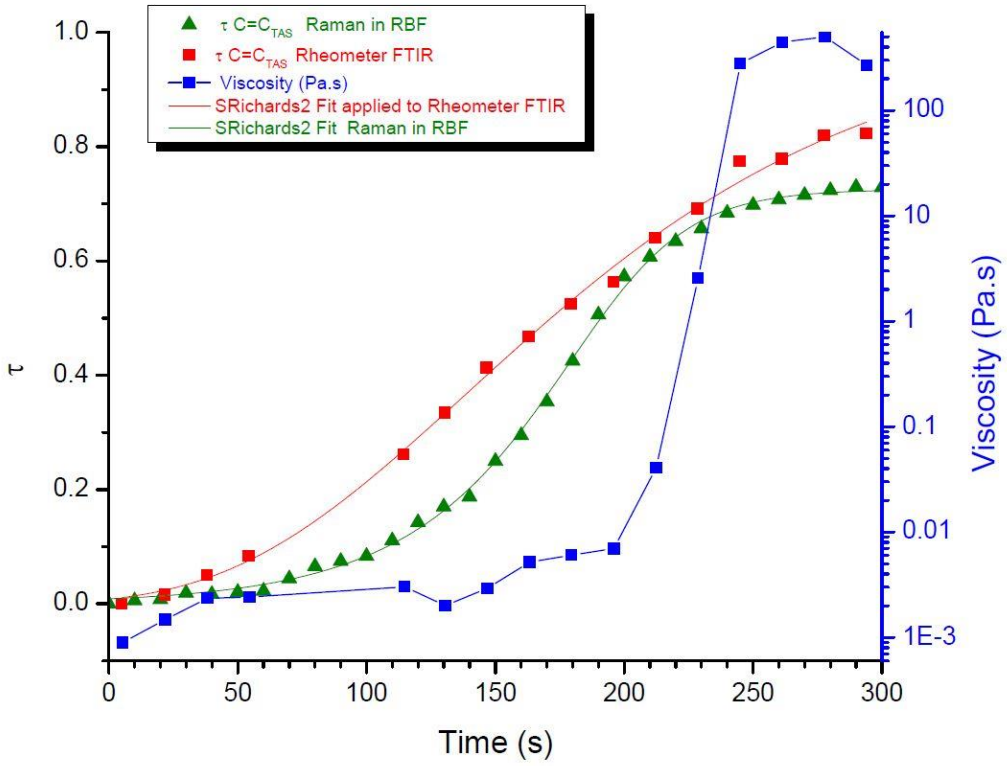

Figure 4.9. Coupling results from the Rheo-Raman-FTIR setup combined with the reference alkene conversion obtained from RBF together with the evolution macromolecules of S1-S7 from window C.

Based on Figure 4.10 it was noticed that the average molar mass and the viscosity increased gradually from an alkene conversion in the range of 0.32 to 0.65. The transition between random coil structures to hyperbranched structures occurred at a critical alkene conversion of 0.58 where the macromolecular networks started to influence the viscosity of the reaction medium. At an alkene conversion of 0.62 most of the active sites during the polymerisation reaction were consumed. In addition, the molar-mass dispersity recorded a sudden decrease since the macromolecules present at this moment of the polymerisation reaction were approximately of same molar mass range.

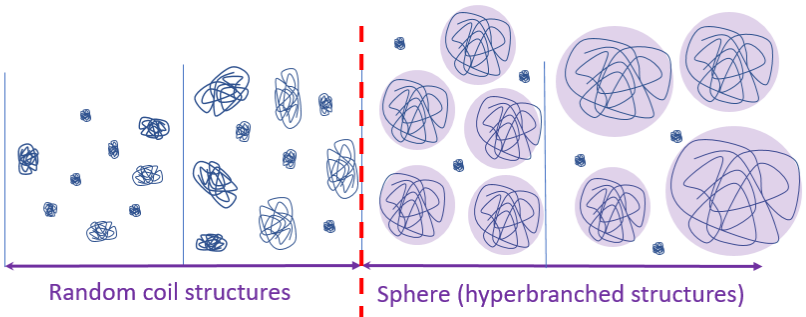

Samples	S1-4	S5	S6	S7
$\overline{M}_W\ (g, mol^{-1})$	4,386-3,1080	40,230	320,200	28200,000
Đ	1.56-5.37	7.81	1.35	11.48
η (mPa.s)	2-5	7	17	125
τ	0.32-0.51	0.58	0.62	0.65

Figure 4.10. Structures of the S1-7 along with their average molar mass, molar-mass dispersity, alkene conversion and viscosity.

Finally, at an alkene conversion of 0.65, the molar mass, the molar-mass dispersity, and the viscosity had a significant increase moments before the gel turned into a solid form. Moreover, at this alkene conversion, the macromolecules with varying molar mass 10^6-10^8 g·mol^{-1} made up the hyperbranched structures of polycarbosilanes.

Figure 4.11 illustrated a 3D graph of alkene conversion against average molar mass and the viscosity. Each sampling points could be correlated to an alkene conversion (x-axis), viscosity of the medium (y-axis) and the average molar mass of the macromolecules (z-axis) during the polymerisation reaction as shown in Figure 4.11. As expected, it was only after the critical alkene conversion (0.58) that the molar mass and the viscosity of the sample increased drastically. Based on Figure 4.11, a viscosity window ranging from 2 to 125 mPa·s was established. Moreover, within this viscosity window, the polymerisation process can be stopped at any given moment by using to obtain a suitable viscosity that correspond to a particular shaping process.

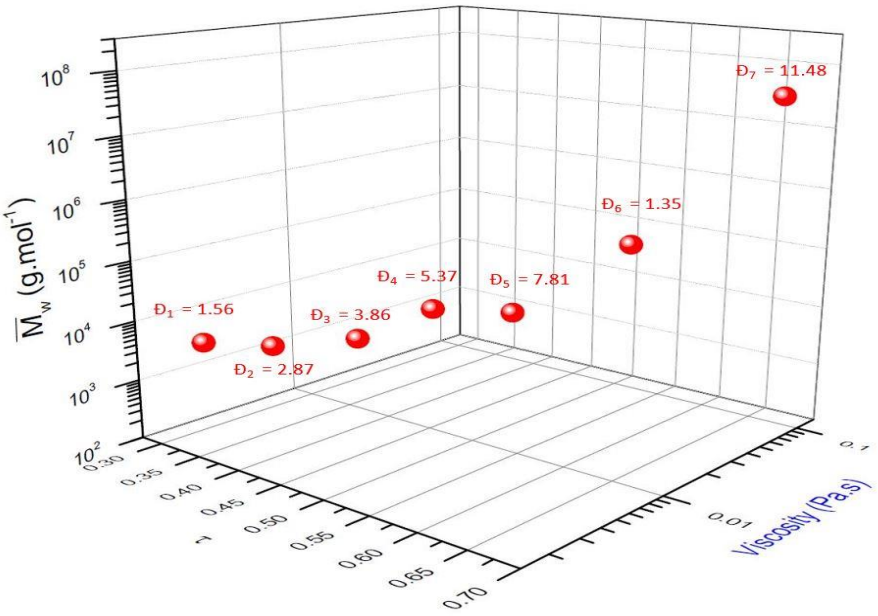

Figure 4.11. 3D representation of alkene conversion plotted against average molar mass and viscosity of the medium from an alkene conversion 0.32 to 0.65.

According to the literature, the viscosity domain obtained could correspond to shaping process such as spin coating, inkjet print and plasma spraying at a shear rate around 10^3 to 10^6 s^{-1} [CAR20]. This is one of the major achievements of this project, to be able to correlate the viscosity of the preceramic polymer to a shaping process. Normally polymer samples are subjected to a wide range of shear rates that can affect the quality of the shaping process and eventually the final product. Hence, it is pivotal to understand and control the rheological properties of the polymer sample during the shaping process to avoid problems of clogging, lack of fluidity, or agglomeration. Thus, the platform will adapt the viscosity of a polymer sample to a corresponding shear rate required to carry out the shaping process at optimum conditions.

Since the platform has successfully correlated the architecture of the synthesised polycarbosilane and the kinetics of the reaction with the rheology of the medium, the experimental conditions could be reviewed to find an adapted viscosity for other types of shaping process. For instance, the catalyst concentration, monomer concentration could be increased/decreased or the hydrosilylation reaction could be activated by temperature.

Moreover, the elaboration of this platform will provide the opportunity to monitor other macromolecular structure like linear polymer one wherein a contrast can be drawn between the synthesis of a hyperbranched polymer to determine the branching ratio of the hyperbranched polymer. Furthermore, other types of preceramic polymers (polysiloxanes, polysilazanes, polysilycarbodiimides, etc.) as well as other types of polymerisation reaction (ring-opening polymerisation, polycondensation) could be studied *via* this platform. Thus, this work will strengthen several research topics in IRCER.

4.6. Conclusion

The polymerisation reaction carried out on the Rheo-Raman-FTIR setup was repeated in RBF to facilitate sampling of polymer solutions during the real time monitoring of the reaction. Three sampling windows were considered during the reaction namely A, B and C. Sampling window C was selected since it reported sufficient MALS signal and its sampling window was the nearest to the moment when the gel turned into a solid form. Seven samples were collected within the sampling window C ranging from 160 s to 226 s. The sampling time corresponded to an alkene conversion of 0.32 to 0.65. Moreover, the seven sampling points collected were characterised by the SEC-MALS to gather information about the evolution of the structures of the macromolecules in terms of molar mass, molar-mass dispersity and conformation of the polymer structure.

Based on the SEC-MALS results, for S1-6 the average molar mass increased steadily from 4386 $g.mol^{-1}$ to 320200 $g \cdot mol^{-1}$ before registering a rapid increase of nearly 2 orders of magnitude for the last sample (S7) as the crosslinking was more consequent around 216 s. In parallel, the molar-mass dispersity increased from 1.56 to 11.48 as the polymerisation reaction progressed. However, S6 reported a sudden decrease in molar-mass dispersity (1.35) that could be attributed to the crosslinking of macromolecules leading to polymer networks having close molar mass. Furthermore, it was noticed, based on the conformation plot of log RMS radius against log molar mass, that the structures of the macromolecules developed from a random coil to a sphere (hyperbranched structures) during the polymerisation reaction.

One of the objectives was to synchronise the reaction taking place in RBF to that on the Rheo-Raman-FTIR. This was achieved *via* the alkene conversion obtained from both setups *i.e.* the alkene conversion in RBF was synchronised to the alkene conversion obtained from the FTIR data.

By combining the data obtained from the platform, a better understanding and control of the macromolecular growth were achieved. For an alkene conversion of 0.32 to 0.65, the corresponding average molar mass was correlated to the viscosity of the medium. Thus, within this range of alkene conversion, the real-time monitoring of the structures of the macromolecules with respect to the viscosity of the medium was achieved. A viscosity window ranging from 2 to 125 mPa·s was established. Based on literature, this viscosity could correspond to shaping processes like spin coating, inkjet print and plasma spraying [CAR20].

The development of this platform constitutes an important aspect in understanding fundamental study of preceramic polymer since a direct correlation in real time between viscosity and average molar mass of the developing macromolecules was put in evidence.

General conclusion

This project deals with the development of a platform to monitor the *in-situ* synthesis of a preceramic polycarbosilane starting from two suitable monomers. The idea was to access rheological, structural and physical information, to master the synthesis of preceramic polymers. To reach this goal, a unique platform consisting in a rheometer dynamically combined with infrared and Raman spectrometers, plus a MALS detector, has been developed.

The Rheo-FTIR setup initially performed a real time monitoring of the hydrosilylation reaction by starting with di- and tetrafunctional monomers. Subsequently a *hb*-PCS was synthesised with a yield of 94 %. The structural changes were successfully correlated with the rheological moduli. However, the information obtained from FTIR (ATR mode) provided only a surface information which were not representative of what is happening within the volume of the sample. To overcome this key point, a Raman spectrometer associated to a lens which lead to a larger depth penetration was added to the existing Rheo-FTIR. Hence, the new platform used two complementarily vibrational techniques to perform a structural analysis of the sample. It was the first time that a Raman spectrometer was attached to a Rheo-FTIR device. The optimisation of the new platform was carried out in terms, of gap (0.6 mm), intensity of the Raman signal, and concentration of the catalyst. Moreover, it was found out that the viscosity increased rapidly only after a critical alkene conversion of 0.58 was reached. Below this value, the conversion evolved faster but without any impacts on the viscosity. This was due to the fact that the macromolecular networks were not built enough during the hydrosilylation reaction to properly affect the viscosity of the medium. This finding was a first step in understanding the relationship between the kinetics of the polymerisation and the rheological behaviour. The development of the Rheo-FTIR-Raman setup is an innovation for monitoring real time polymerisation reaction as it provides an analysis of the molecular structure of the analyses sample that could be correlated to the rheology of the medium. To better understand the impact of the polymer architecture on the rheology of the medium, the SEC-MALS coupling would provide addition information about the structure of the macromolecules in terms of average molar mass, molar-mass dispersity and its conformation structure. Thus, the relationship between the average molar mass of the macromolecules and the structural changes were put in evidence.

The polymerisation reaction carried out on the Rheo-Raman-FTIR setup was repeated in RBF by keeping the same concentration of the reagents and under same experimental conditions. During the sampling process, seven samples were obtained between 163 s to 226 s during the real time monitoring of the hydrosilylation reaction. The sampling time from 163 s to 226 s corresponded to an alkene conversion of 0.32 to 0.65. Within this timeframe, a sufficient MALS signal for all samples was registered as sampling occurred near the moment

the gel turned into a solid form. The seven samples (S1-7) were characterised by the coupling SEC-MALS to gather information about the evolution of the structures the macromolecules in terms of molar mass, molar-mass dispertsity and conformation of the polymer structure. Based on the SEC-MALS results, for S1-6 the average molar mass increased steadily from 4386 $g.mol^{-1}$ to 320200 $g.mol^{-1}$ before registering a rapid increase of nearly 2 orders of magnitude for the last sample (S7) as the crosslinking was more consequent around 216 s. In parallel, the molar-mass dispersity increased from 1.56 to 11.48 as the polymerisation reaction progressed. However, S6 reported a sudden decrease in molar-mass dispersity (1.35) that could be attributed to the crosslinking of macromolecules leading to polymer networks having close molar mass. Moreover, according to the conformation plot, the polymer solution sampled developed from a random coil to a sphere (hyperbranched structures) during the reaction.

The synchronisation of the reaction taking place in RBF to that on the Rheo-Raman-FTIR was performed *via* the monomer conversion. In this way, for an alkene conversion of 0.32 to 0.65, the corresponding the average molar mass of the macromolecules could be correlated to the viscosity of the medium. Thus, within this range of alkene conversion, the real-time monitoring of the structures of the macromolecules with respect to the viscosity of the medium was achieved. A viscosity window ranging from 2 to 125 mPa·s was established. Based on literature review, this viscosity would correspond to shaping processes such as inkjet print, plasma spraying and spin coating at a shear rate around 10^3 to 10^6 s^{-1} [CAR20]. This is one of the major achievements of this project, to be able to correlate the viscosity of the preceramic polymer to a shaping process. Therefore, the platform has enabled the monitoring of the *in-situ* hydrosilylation reaction.

The platform can still be optimised, as one of the difficulties experienced on the Rheo-Raman-FTIR setup was to optimise the intensity of the Raman signal on a gap of 0.6 mm. A pinhole can be used during the experiment to block some of the stray light. However, this might decrease the signal that reach the detector. Another possibility will be to increase the gap distance between the plate-plate configurations according to the wettability of the reagents. Furthermore, the domain of temperature provided by the rheometer from ambient to 400 °C can be useful to check the behaviour of the polymers in terms of stability and shaping, and to head for polymers with lower processing temperatures. In addition, the polymerisation reaction can be carried out in an argon atmosphere as the impact of atmosphere is of importance given the sensitivity of carbosilanes in air. Moreover, the ratio of monomers can be varied as well as the catalyst concentration to adapt the viscosity to a particular shaping process. The addition of fillers in the monomers composition can reduce the rate of crosslinking of the reaction, thus extending the time available to shape the

preceramic polymer before the pyrolysis step. Suitable models can be applied to the viscosity curve and the to the kinetics of the polymerisation including the induction effect of the catalyst during the hydrosilylation reaction.

Since the platform has successfully linked the average molar mass to the viscosity of the medium, this will enable the monitoring of other polymerisation reactions. For instance, a linear polymer can be synthesised, wherein a contrast can be drawn between the syntheses of a hyperbranched polymer structure to determine the branching ratio of the hyperbranched polymer. Furthermore, the platform can be used to facilitate other shaping processes as by starting with defined monomers, the relationship between the average molar mass and viscosity of the medium can be established. The platform will provide a better understanding and control of the polymerisation reaction, thus enabling a better control on the ceramic material generated.

References

[AB11] H. Abderrazak, E. Hmida, «Silicon carbide: synthesis and properties», *IntechOpen*, p. 361-388, 2011, DOI: 10.5772/615;

[AC93] E. G. Acheson, «Carborundum: Its history, manufacture and uses», *Journal of the Franklin Institute*, vol. 136, no 4, p. 279-289, 1893, DOI: https://doi.org/10.1016/0016-0032(93)90369-6;

[AI60] F. W. Ainger, J. M. Herbert, «The preparation of Phosphorous-Nitrogen Compounds as Non-Porous Solids», *Special Ceramics*, Academic Press New York, p.168-182, 1960;

[AL98] F. Aldinger, M. Weinmann, J. Bill, «Precursor-derived Si-BCN ceramics», *Pure Appl. Chem.*, vol. 70, no 2, p. 439–448, 1998, DOI: 10.1351/pac199870020439;

[AT70] P. W. Atkins, M. S. Child, C. S. G. Phillips, Tables for Group Theory, *Oxford University Press*, 1970, ISBN: 978-0198551317;

[AU15] M. Auriemma, A. Piscitelli, R. Pasquino, P. Cerruti, M. Malinconico, N. Grizzuti, «Blending poly(3-hydroxybutyrate) with tannic acid: Influence of a polyphenolic natural additive on the rheological and thermal behavior», *Eur. Polym. J.*, vol. 63, p. 123-131, 2015, DOI: https://doi.org/10.1016/j.eurpolymj.2014.12.021;

[AZ18] M. El-Azazy, «Introductory chapter: infrared spectroscopy - A synopsis of the fundamentals and applications», *Infrared Spectroscopy-Principles, Advances and Applications*, IntechOpen, 2018, DOI: 10.5772/intechopen.82210;

[BA89] H. A. Barnes, J. F. Hutton, K. Walters, An introduction to rheology, *Elsevier*, 1989, ISBN: 978-0-444-87469-6;

[BA92] M. Balat, G. Flamant, G. Male, et G. Pichelin, «Active to passive transition in the oxidation of silicon carbide at high temperature and low pressure in molecular and atomic oxygen», *Journal of Materials Science*, vol. 27, no 3, p. 697-703, 1992, DOI: https://doi.org/10.1007/BF02403882;

[BA96] M. J. Balat, «Determination of the active-to-passive transition in the oxidation of silicon carbide in standard and microwave-excited air», *Journal of the European Ceramic Society*, vol. 16, no 1, p. 55-62, 1996, DOI: https://doi.org/10.1016/0955-2219(95)00104-2;

[BA99] P. Baldus, M. Jansen, D. Sporn, «Ceramic fibers for matrix composites in high-temperature engine applications», *Science*, vol. 285, no 5428, p. 699–703, 1999, DOI: 10.1126/science.285. 5428.699;

[BA14] M. J. Baker et al., «Using Fourier transform IR spectroscopy to analyze biological materials», *Nature Protocols*, vol. 9, no 8, p. 1771-1791, 2014, DOI: https://doi.org/10.1038/nprot.2014.110;

[BE24] J. J. Berzelius, «Untersuchungen über die Flussspathsäure und deren merkwürdigsten Verbindungen», *Annalen der Physik*, vol. 77, no 6, p. 169-230, 1824, DOI: https://doi.org/10.1002/ andp.18240770603;

[BE01] S. R. Bean, G. L. Lookhart, «Factors influencing the characterization of gluten proteins by size-exclusion chromatography and multiangle laser light scattering (SEC-MALLS)», *Cereal Chemistry*, vol. 78, no 5, p. 608-618, 2001, DOI: 10.1094/CCHEM.2001.78.5.608;

[BE05] S. Bernard, M. Weinmann, D. Cornu, P. Miele, F. Aldinger, «Preparation of high-temperature stable Si-B-C-N fibers from tailored single source polyborosilazanes», *J. Eur. Ceram. Soc.*, vol. 25, no 2-3, p. 251-256, 2005, DOI: 10.1016/j.jeurceramsoc.2004.08.015;

[BE13] S. Bernard, O. Majoulet, F. Sandra, A. Malchere, et P. Miele, «Direct Synthesis of Periodic Mesoporous SilicoBoron CarboNitride Frameworks via the Nanocasting from Ordered Mesoporous

Silica with Boron-Modified Polycarbosilazane», *Adv. Eng. Mater.*, vol. 15, no 3, p. 134-140, 2013, DOI: 10.1002/adem.201200168;

[BEL13] L. Bellamy, The Infra-red Spectra of Complex Molecules, *Springer Science & Business Media*, 2013, ISBN: 978-0-412-13850-8;

[BE17] M. C. Bechelany, V. Proust, A. Lale, P. Miele, S. Malo, C. Gervais, S. Bernard, «Nanocomposites through the Chemistry of Single-Source Precursors: Understanding the Role of Chemistry behind the Design of Monolith-Type Nanostructured Titanium Nitride/Silicon Nitride», *Chemistry – A European Journal*, vol. 23, no 4, p. 832 845, 2017, DOI: 10.1002/chem.201603661;

[BI95] J. Bill, F. Aldinger, «Precursor-derived Covalent Ceramics», *Adv. Mater.*, vol. 7, no 9, p. 775-787, 1995, DOI: 10.1002/ADMA.19950070903;

[BO87] M. Bougoin, F. Thevenot, J. Dubois, G. Fantozzi, «Synthese et proprietes thermomecaniques de ceramiques denses composites carbure de bore-carbure de silicium», *Journal of the Less Common Metals*, vol. 132, no 2, p. 209-228, 1987, DOI: https://doi.org/10.1016/0022-5088(87) 90577-7;

[BO92] B. Boury, R. J. P. Corriu, D. Leclercq, H. Mutin, J. M. Planeix, A. Vioux, «A Catalytic Preparation of a New Preceramic Polymer: Transformation Into SiC», *Inorganic and Organometallic Polymers with Special Properties*, Springer, 1992, p. 255-266, DOI: 10.1007/978-94-011-2612-0_18;

[BO14] R. K. Bose, J. Kötteritzsch, S. J. Garcia, M. D. Hager, U. S. Schubert, S. van der Zwaag, «A rheological and spectroscopic study on the kinetics of self-healing in a single-component diels–alder copolymer and its underlying chemical reaction», *J. Polym. Sci. Part Polym. Chem.*, vol. 52, no 12, p. 1669-1675, 2014, DOI: https://doi.org/10.1002/pola.27164;

[BO16] F. Bouzat, A.-R. Graff, R. Lucas, S. Foucauda, «Preparation of C/SiC ceramics using a preceramic polycarbosilane synthesized via hydrosilylation», *Journal of the European Ceramic Society*, vol. 36, no 12, p. 2913-2921, 2016, DOI: https://doi.org/10.1016/j.jeurceramsoc.2015. 11.032;

[BR13] N. Brun, I. Youssef, M.-C. Chevrel, D. Chapron, C. Schrauwen, S. Hoppe, P. Bourson, A. Durand, «In situ monitoring of styrene polymerization using Raman spectroscopy. Multi-scale approach of homogeneous and heterogeneous polymerization processes», *J. Raman Spectrosc.*, vol. 44, no 6, p. 909-915, 2013, DOI: https://doi.org/10.1002/jrs.4279;

[BR14] N. Brun, M.-C. Chevrel, L. Falk, S. Hoppe, A. Durand, D. Chapron, P. Bourson, «Contribution of Raman Spectroscopy to In Situ Monitoring of a High- Impact Polystyrene Process», *Chemical Engineering & Technology*, vol. 37, no 2, p. 275-282, 2014, DOI: 10.1002/CEAT.201300421;

[BR18] M. Q. Brisebourg, F. Rebillat, F. Teyssandier, «Oxidation of ß-SiC at high temperature in Ar/O2, Ar/CO2, Ar/H2O gas mixtures: Kinetic study of the silica growth in the passive regime», *Journal of the European Ceramic Society*, vol. 38, no 13, p. 4309-4319, 2018, DOI: https://doi.org/10.1016/ j.jeurceramsoc.2018.05.029;

[BU16] G. S. Bumbrah, R. M. Sharma, «Raman spectroscopy – Basic principle, instrumentation and selected applications for the characterization of drugs of abuse», *Egyptian Journal of Forensic Sciences*, vol. 6, no 3, p. 209-215, 2016, DOI: https://doi.org/10.1016/j.ejfs.2015.06.001;

[CA97] A. Cadenato, J. Salla, X. Ramis, J. Morancho, L. Marroyo, J. Martin, «Determination of gel and vitrification times of thermoset curing process by means of TMA, DMTA and DSC techniques: TTT diagram», *Journal of Thermal Analysis and Calorimetry*, vol. 49, no 1, p. 269-279, 1997, DOI: https://doi.org/10.1007/BF01987448;

[CA20] J. M. Cameron, C. Bruno, D. R. Parachalil, M. J. Baker, F. Bonnier, H. J. Butler, H. J. Byrne, «Vibrational spectroscopic analysis and quantification of proteins in human blood plasma and serum», *Vibrational Spectroscopy in Protein Research*, Elsevier, p. 269-314, 2020, DOI: https://doi.org/10.1016/B978-0-12-818610-7.00010-4;

[CAR20] V. Carnicer Cervera, M. D. C. Alcazar Rodrigo, M. J. Orts Tarí, E. Sánchez-Vilches, R. Moreno, «Microfluidic rheology: A new approach to measure viscosity of ceramic suspensions at extremely high shear rates», *Open Ceramics*, vol. 5, 100052, 2020, DOI: https://doi.org/10.1016/j.oceram. 2020.100052;

[CH06] X. Cheng, Z. Xie, Y. Song, J. Xiao, Y. Wang, «Structure and properties of polycarbosilane synthesized from polydimethylsilane under high pressure», *Journal of applied polymer science*, vol. 99, no 3, p. 1188-1194, 2006, DOI: https://doi.org/10.1002/app.22594;

[CH08] J. Chen, G. He, Z. Liao, B. Zeng, J. Ye, L. Chen, H. Xia, L. Zhang, «Control of structure formation of polycarbosilane synthesized from polydimethylsilane by Kumada rearrangement», *Journal of applied polymer science*, vol. 108, no 5, p. 3114-3121, 2008, DOI: 10.1002/app.27262;

[CH12] M.-C. Chevrel, S. Hoppe, L. Falk, B. Nadège, D. Chapron, P. Bourson, A. Durand, «Rheo-Raman: A Promising Technique for In Situ Monitoring of Polymerization Reactions in Solution», *Ind. Eng. Chem. Res.*, vol. 51, no 49, p. 16151-16156, 2012, DOI: https://doi.org/10.1021/ie302054k;

[CH14] M.-C. Chevrel, N. Brun, S. Hoppe, D. Meimaroglou, L. Falk, D. Chapron, P. Bourson A. Durand, «In situ monitoring of acrylic acid polymerization in aqueous solution using rheo-Raman technique. Experimental investigation and theoretical modelling», *Chem. Eng. Sci.*, vol. 106, p. 242-252, 2014, DOI: https://doi.org/10.1016/j.ces.2013.11.039;

[CH18] V. Chauhan, A. Kumar, N. A. Bhalla, M. Danish, V. Ranjan, «Numerical study of shear thickening fluid with distinct particles dispersed in carrier fluid», *Vibroengineering PROCEDIA*, vol. 21, p. 242-247, 2018, DOI: https://doi.org/10.21595/vp.2018.20397;

[CH20] Y. C. Cho, S. I. Ahn, «Fabricating a Raman spectrometer using an optical pickup unit and pulsed power», *Sci. Rep.*, vol. 10, no 1, p. 11692, 2020, DOI: https://doi.org/10.1038/s41598-020-68650-7;

[CH65] P. G. Chantrell, P. Popper, «Inorganic Polymers for ceramics», *Special Ceramics*, Academic Press, New York p. 67, 1965;

[CHA65] A. J. Chalk, J. F. Harrod, «Homogeneous Catalysis. II. The Mechanism of the Hydrosilation of Olefins Catalyzed by Group VIII Metal Complexes», *Journal of the American Chemical Society*, vol. 87, no 1, 1965, DOI: https://doi.org/10.1021/ja01079a004;

[CH91] N. S. Choong Kwet Yive, R. Corriu, D. Leclercq, H. Mutin, A. Vioux, «Polyvinylsilazane: a novel precursor to silicon carbonitride», *New J. Chem.*, vol. 15, no 1, p. 85-92, 1991, DOI: 10.1016/0955-2219(91)90098-k;

[CH92] N. S. Choong Kwet Yive, R. J. P. Corriu, D. Leclercq, P. H. Mutin, A. Vioux, «Silicon carbonitride from polymeric precursors: Thermal cross-linking and pyrolysis of oligosilazane model compounds», *Chemistry of materials*, vol. 4, no 1, p. 141–146, 1992, DOI: https://doi.org/10.1021/cm00019a029;

[CH97] B.-S. Chiou, S. A. Khan, «Real-Time FTIR and in Situ Rheological Studies on the UV Curing Kinetics of Thiol-ene Polymers», *Macromolecules*, vol. 30, no 23, p. 7322-7328, 1997, DOI: https://doi.org/10.1021/ma9708656;

[CO02] P. Colombo, J. R. Hellmann, «Ceramic foams from preceramic polymers», *Materials Research Innovations*, vol. 6, no 5, p. 260-272, 2002, DOI: https://doi.org/10.1007/s10019-002-0209-z;

[CO07] B. Coto, J. M. Escola, I. Suárez, M. J. Caballero, «Determination of dn/dc values for ethylene–propylene copolymers», *Polymer testing*, vol. 26, no 5, p. 568-575, 2007, DOI: https://doi.org/ 10.1016/ j.polymertesting.2007.02.001;

[CO10] P. Colombo, G. Mera, R. Riedel, G. D. Sorarù, «Polymer-Derived Ceramics: 40 Years of Research and Innovation in Advanced Ceramics», *J. Am. Ceram. Soc.*, vol. 93, no 7, p. 1805-1837, 2010, DOI: https://doi.org/10.1111/j.1551-2916.2010.03876.x;

[DA15] G. Darsy, F. Bouzat, M. Muñoz, R. Lucas, S. Foucaud, C. Coelho, Diogo, F. Babonneau, Y. Leconte, A. Maître, «Monitoring a polycycloaddition by the combination of dynamic rheology and

FTIR spectroscopy», *Polymer*, vol. 79, p. 283-289, 2015, DOI: https://doi.org/10.1016/j.polymer. 2015.10.030;

[DA73] G. Davidson, P. G. Harrison, E. M. Riley, «The vibrational spectra of tetra-allyl silane and tetra-allyl tin», *Spectrochimica Acta Part A: Molecular Spectroscopy*, vol. 29, no 7, p. 1265-1272, 1973, DOI: 10.1016/0584-8539(73)80189-8;

[DU07] S. Duperrier, C. Gervais, S. Bernard, D. Cornu, F. Babonneau, C. Balan, P. Miele, «Design of a series of preceramic B-tri (methylamino) borazine-based polymers as fiber precursors: Architecture, thermal behavior, and melt-spinnability», *Macromolecules*, vol. 40, no 4, p. 1018-1027, 2007, DOI: https://doi.org/10.1021/ma0623035;

[DUS07] S. Duperrier, S. Bernard, A. Calin, C. Sigala, R. Chiriac, P. Miele, C. Balan, «Design of a series of preceramic B-tri (methylamino) borazine-based polymers as fiber precursors: Shear rheology investigations», *Macromolecules*, vol. 40, no 4, p. 1028–1034, 2007, DOI: https://doi.org/10.1021/ ma062304x;

[FA89] J. Fahrenfort, «Attenuated total reflection: A new principle for the production of useful infra-red reflection spectra of organic compounds», *Spectrochimica Acta Part A: Molecular Spectroscopy*, vol. 45, p. 251-263, 1989, DOI: 10.1016/S0584-8539(89)80276-4;

[FA13] G. Fantozzi, J.-C. Niepce, G. Bonnefont, «Les céramiques industrielles: Propriétés, mise en forme et applications», *Dunod*, 2013, ISBN: 978-2100577392;

[FR56] G. Fritz, B. Raabe, «Bildung siliciumorganischer Verbindungen. V. Die Thermische Zersetzung von Si(CH3)4 und Si(C2H5)4», *Zeitschrift für anorganische und allgemeine Chemie*, vol. 286, no 3-4, p. 149-167, 1956, DOI: 10.1002/zaac.19562860307;

[FR17] G. Franchin, L. Wahl, P. Colombo, «Direct ink writing of ceramic matrix composite structures», *Journal of the American Ceramic Society*, vol. 100, no 10, p. 4397–4401, 2017, DOI: 10.1111/jace.15045;

[FR18] G. Franchin, H. Maden, L. Wahl, A. Baliello, M. Pasetto, P. Colombo, «Optimization and characterization of preceramic inks for direct ink writing of ceramic matrix composite structures», *Materials*, vol. 11, no 4, p. 515, 2018, DOI: 10.3390/ma11040515;

[GE00] P. Greil, «Polymer Derived Engineering Ceramics», *Advanced Engineering Materials*, vol. 2, no 6, p. 339-348, 2000, DOI: https://doi.org/10.1002/1527-2648(200006)2:6<339::AID-ADEM339> 3.0.CO;2-K;

[GL13] S. E. Glassford, B. Byrne, S. G. Kazarian, «Recent applications of ATR FTIR spectroscopy and imaging to proteins», *Biochimica et Biophysica Acta (BBA)-Proteins and Proteomics*, vol. 1834, no 12, p. 2849-2858, 2013, DOI: 10.1016/j.bbapap.2013.07.015;

[GR00] P. Greil, «Polymer Derived Engineering Ceramics», *Advanced Engineering Materials*, vol. 2, no 6, p. 339-348, 2000, DOI: https://doi.org/10.1002/1527-2648(200006)2:6<339::AID-ADEM339>3.0. CO;2-K;

[GR83] P. R. Griffiths, «Fourier transform infrared spectrometry», *Science*, vol. 222, no 4621, p. 297-302, 1983, DOI: 10.1126/science.6623077;

[GU02] P. Gupta, S. Garg, «Semisolid dosage forms for dermatological application», *Pharmaceutical technology*, p. 144-162, 2002;

[GU11] R. K. Gupta, R. Mishra, R. K. Tiwari, A. Ranjan, A. K. Saxena, «Studies on the Rheological Behavior of Polycarbosilane Part I: Effect of Time, Temperature and Atmosphere», *Silicon*, vol. 3, no 1, p. 27-35, 2011, DOI: 10.1007/s12633-010-9054-7;

[GU14] R. K. Gupta, A. K. Saxena, «Rheological Behavior of Polycarbosilane Part II: Effect of Heterometal (Al) Content and Nature of Bonding with Si of Polycarbosilane», *Silicon*, vol. 6, no 4, p. 233-246, 2014, DOI: 10.1007/s12633-014-9225-z;

[GU72] E. A. Gulbransen, S. A. Jansson, «The high-temperature oxidation, reduction and volatilization reactions of silicon and silicon carbide», *Oxid. Met.*, vol. 4, no 3, p. 181-201, 1972, DOI: 10.1007/BF00613092;

[GU97] P. J. Guichelaar, «Acheson process», *Carbide, Nitride and Boride Materials Synthesis and Processing*, Springer, p. 115-129, 1997, DOI: 10.1007/978-94-009-0071-4_4;

[HA04] R. Harshe, C. Balan, R. Riedel, «Amorphous Si (Al) OC ceramic from polysiloxanes: bulk ceramic processing, crystallization behavior and applications», *Journal of the European Ceramic Society*, vol. 24, no 12, p. 3471-3482, 2004, DOI: https://doi.org/10.1016/j.jeurceramsoc.2003.10.016;

[HA07] T. Hayashi, K. Yamasaki, «C–E bond formation through asymmetric hydrosilylation of alkenes», R.H.Crqbtree, D.M.P. Mingos (Eds.), *Comprehensive Organometallic Chemistry III*, vol.10, Elsevier Ltd., Oxford, 2007, DOI: 10.1016/b0-08-045047-4/00140-0;

[HA13] B. Harder, N. Jacobson, D. Myers, «Oxidation transitions for SiC part II. Passive-to-active transitions», *Journal of the American Ceramic Society*, vol. 96, no 2, p. 606-612, 2013, DOI: https://doi.org/10.1111/jace.12104;

[HA60] N. J. Harrick, «Surface chemistry from spectral analysis of totally internally reflected radiation», *The Journal of Physical Chemistry*, vol. 64, no 9, p. 1110-1114, 1960, DOI: https://doi.org/10.1021/j100838a005;

[HE20] F. J. Hernández-Rangel, M. Z. Saavedra-Leos, J. Morales-Morales, H. Bautista-Santos, V. A. Reyes-Herrera, J. M. Rodríguez-Lelis, P. Cruz-Alcantar, «Continuous Improvement Process in the Development of a Low-Cost Rotational Rheometer», *Processes*, vol. 8, no 8, p. 935, 2020, DOI: https://doi.org/10.3390/pr8080935;

[HE90] A. H. Heuer, V. L. Lou, «Volatility diagrams for silica, silicon nitride, and silicon carbide and their application to high-temperature decomposition and oxidation», *Journal of the American Ceramic Society*, vol. 73, no 10, p. 2789-2803, 1990, DOI: 10.1111/j.1151-2916.1990.tb06677.x;

[HI13] T. HINOKI et al., «Silicon Carbide and Silicon Carbide Composites for Fusion Reactor Application», *Materials Transactions*, vol. 54, no 4, p. 472-476, 2013, DOI: 10.2320/matertrans.MG201206;

[HI76] J. W. Hinze, H. C. Graham, «The Active Oxidation of Si and SiC in the Viscous Gas-Flow Regime», *J. Electrochem. Soc.*, vol. 123, no 7, p. 1066, 1976, DOI: 10.1149/1.2132997;

[HO17] R. J. Hofmann, M. Vlatković, F. Wiesbrock, «Fifty Years of Hydrosilylation in Polymer Science: A Review of Current Trends of Low-Cost Transition-Metal and Metal-Free Catalysts, Non-Thermally Triggered Hydrosilylation Reactions, and Industrial Applications», *Polymers*, vol. 9, no 10, Art. no 10, 2017, DOI: 10.3390/polym9100534;

[HO22] X. Hou, P. D. Lund, Y. Li, «Controlling anodization time to monitor film thickness, phase composition and crystal orientation during anodic growth of TiO2 nanotubes», *Electrochemistry Communications*, vol. 134, p. 107168, 2022, DOI: https://doi.org/10.1016/j.elecom.2021.107168;

[HQ01] H. Q. Ly, R. Taylor, R. J. Day, F. Heatley, «Conversion of polycarbosilane (PCS) to SiC-based ceramic Part 1. Characterisation of PCS and curing products», *Journal of Materials science*, vol. 36, no 16, p. 4037-4043, 2001, DOI: https://doi.org/10.1023/A:1017942826657;

[ID01] A. Idesaki, M. Narisawa, K. Okamura, M. Sugimoto, Y. Morita, T. Seguchi, M. Itoh, «Application of electron beam curing for silicon carbide fiber synthesis from blend polymer of polycarbosilane and polyvinylsilane», *Radiation Physics and Chemistry*, vol. 60, no 4-5, p. 483-487, 2001, DOI: https://doi.org/10.1016/S0969-806X(00)00394-7;

[ID04] A. Idesaki, M. Sugimoto, S. Tanaka, M. Narisawa, K. Okamura, M. Itoh, «Synthesis of a minute SiC product from polyvinylsilane with radiation curing Part I Radiation curing of polyvinylsilane», *Journal of materials science*, vol. 39, no 18, p. 5689-5694, 2004, DOI: 10.1023/B:JMSC.0000040077.94183.ac;

[IN00] L. V. Interrante, Q. Shen, «Polycarbosilanes», *Silicon-Containing Polymers: The Science and Technology of Their Synthesis and Applications*, R. G. Jones, W. Ando, et J. Chojnowski, Éd. Dordrecht: Springer Netherlands, p. 247-321, 2000, DOI: 10.1007/978-94-011-3939-7_10;

[IN02] L. V. Interrante, K. Moraes, Q. Liu, N. Lu, A. Puerta, L. G. Sneddon, «Silicon-based ceramics from polymer precursors», *Pure and applied chemistry*, vol. 74, no 11, p. 2111-2117, 2002, DOI: https://doi.org/10.1351/pac200274112111;

[IN97] L. V. Interrante, J. M. Jacobs, W. Sherwood, C. W. Whitmarsh, «Fabrication and properties of fiber-and particulate-reinforced SiC matrix composites obtained with (A) HPCS as the matrix source», *Key Engineering Materials*, 1997, vol. 127, p. 271-278, DOI: 10.4028/www.scientific.net/KEM.127-131.271;

[IO12] E. Ionescu, R. Riedel, «Polymer Processing of Ceramics», *Ceramics and Composites Processing Methods*, John Wiley & Sons, Ltd, p. 235-270, 2012, ISBN: 978-0-470-55344-2;

[IS15] K. Ismail, «Fabrication and characterisation of SERS substrates through photo-deposition of Gold Nanoparticles», *Thesis for postgraduate diploma*, IMEC-Belgium (EnergyVille), 2015, DOI: 10.13140/RG.2.1.4401.0963;

[JA13] N. Jacobson, B. Harder, D. Myers, «Oxidation transitions for SiC Part I. Active-to-passive transitions», *Journal of the American Ceramic Society*, vol. 96, no 3, p. 838-844, 2013, DOI: https://doi.org/10.1111/jace.12108;

[JI17] P. Ji, X. Pei, Y. Miao, L. He, Q. Huang, «Effect of ultraviolet irradiation on the cross-linking process and ceramic yield of liquid hyperbranched polycarbosilane», *Advances in Applied Ceramics*, vol. 116, no 8, p. 445-451, 2017, DOI: 10.1080/17436753.2017.1352110;

[KA16] S. Kaur, G. Mera, R. Riedel, E. Ionescu, «Effect of boron incorporation on the phase composition and high-temperature behavior of polymer-derived silicon carbide», *Journal of the European Ceramic Society*, vol. 36, no 4, p. 967-977, 2016, DOI: 10.1016/j.jeurceramsoc.2015.11.037;

[KI05] Y. Kim, D. G. Shin, H. R. Kim, H. S. Park, D. H. Riu, «Preparation of polycarbosilane using a catalytic process and its practical uses», *Key Engineering Materials*, vol. 287, p. 108-111, 2005, DOI: https://doi.org/10.4028/www.scientific.net/KEM.287.108;

[KI09] C. Kim, J. Sainte Beuve, S. Guilbert, F. Bonfils, «Study of chain branching in natural rubber using size-exclusion chromatography coupled with a multi-angle light scattering detector (SEC-MALS)», *European polymer journal*, vol. 45, no 8, p. 2249-2259, 2009, DOI: https://doi.org/10.1016/ j.eurpolymj.2009.05.015;

[KO98] R. Koc, S. V. Cattamanchi, «Synthesis of beta silicon carbide powders using carbon coated fumed silica», *Journal of Materials Science*, vol. 33, no 10, p. 2537-2549, 1998, DOI: 10.1023/A:1004392900267;

[KU04] N. Kubo, T. Kawase, S. Asahina, N. Kanayama, H. Tsuda, A. Moritani, K. Kitahara, «Growth of SiC films using tetraethylsilane», *Materials Science Forum*, vol. 457, p. 269-272, 2004, DOI: https://doi.org/10.4028/www.scientific.net/MSF.457-460.269;

[LA17] P. Larkin, Infrared and Raman Spectroscopy: Principles and Spectral Interpretation, *Elsevier*, 2017, ISBN: 978-0-12-804162-8;

[LA97] C. Lach, P. Müller, H. Frey, R. Mülhaupt, «Hyperbranched polycarbosilane macromonomers bearing oxazoline functionalities», *Macromolecular rapid communications*, vol. 18, no 3, p. 253-260, 1997, DOI: https://doi.org/10.1002/marc.1997.030180306;

[LAA17] H. Laadoua, R. Lucas, Y. Champavier, S. Foucaud, R. Zerrouki, F. Brouillette, «Processing of in situ synthesized polycarbosilane-derived porous SiC using kraft pulp fibers», *Materials Letters*, vol. 191, p. 46-49, 2017, DOI: https://doi.org/10.1016/j.matlet.2017.01.004;

[LE17] E. A. Levashov, A. S. Mukasyan, A. S. Rogachev, D. V. Shtansky, «Self-propagating high-temperature synthesis of advanced materials and coatings», *International Materials Reviews*, vol. 62, no 4, p. 203-239, 2017, DOI: 10.1080/09506608.2016.1243291;

[LI00] J. Li, J. Tian, L. Dong, «Synthesis of SiC precursors by a two-step sol–gel process and their conversion to SiC powders», *Journal of the European Ceramic Society*, vol. 20, no 11, p. 1853-1857, 2000, DOI: 10.1016/S0955-2219(00)00055-8;

[LI02] L.-A. Liew, Y. Liu, R. Luo, T. Cross, L. An, V. Bright, M. Dunn, J. Daily, R. Raj, «Fabrication of SiCN MEMS by photopolymerization of pre-ceramic polymer», *Sensors and Actuators A: Physical*, vol. 95, no 2-3, p. 120-134, 2002, DOI: 10.1016/S0924-4247(01)00723-3;

[LI09] H. Li, L. Zhang, L. Cheng, Y. Wang, «Oxidation analysis of 2D C/ZrC–SiC composites with different coating structures in CH4 combustion gas environment», *Ceramics International*, vol. 35, no 6, p. 2277-2282, 2009, DOI: 10.1016/j.ceramint.2008.12.002;

[LI14] J. Liu, H. Ishida, J. Maia, «Vinyl ester/clay based nanocomposites: a complementary study of vinyl ester polymerization by hyphenated rheo-Fourier transform infrared and separate rheology/Fourier transform infrared measurements», *Polym. Int.*, vol. 63, no 3, p. 521-528, 2014, DOI: 10.1002/ pi.4546;

[LI15] C. Liu, K. Li, H. Li, S. Zhang, Y. Zhang, X. Hou, «Synthesis, characterization, and ceramization of a SiC–ZrC–C preceramic polymer precursor», *Journal of materials science*, vol. 50, no 7, p. 2824–2831, 2015, DOI: 10.1007/s10853-015-8840-4;

[LI89] J. C. Liao, J. L. Crowley, P. H. Klein, «β-Silicon Carbide Prepared by Rapid Thermal Chemical Vapor Deposition», *Amorphous and Crystalline Silicon Carbide II*, Berlin, Heidelberg, p. 20-25, 1989, DOI: 10.1007/978-3-642-75048-9_4;

[LO15] M. Lodhe, N. Babu, A. Selvam, M. Balasubramanian, «Synthesis and characterization of high ceramic yield polycarbosilane precursor for SiC», *Journal of Advanced Ceramics*, vol. 4, no 4, p. 307-311, 2015, DOI: https://doi.org/10.1007/s40145-015-0165-x;

[LO95] F. Loumagne, F. Langlais, R. Naslain, «Reactional mechanisms of the chemical vapour deposition of SiC-based ceramics from CH3SiCl3H2 gas precursor», *Journal of crystal growth*, vol. 155, no 3-4, p. 205-213, 1995, DOI: 10.1016/0022-0248(95)00181-6;

[MA08] B. Marciniec, «Hydrosilylation: a comprehensive review on recent advances», *Springer*, 2009, ISBN: 978-1-4020-8171-2;

[MA15] K. Mangala, P. S. Sinija, K. Sreekumar, «Palladium(II) supported on polycarbosilane: Application as reusable catalyst for Heck reaction», *Journal of Molecular Catalysis A: Chemical*, vol. 407, p. 87-92, 2015, DOI: 10.1016/j.molcata.2015.06.012;

[MA20] T. G. Mayerhöfer, S. Pahlow, J. Popp, «The Bouguer-Beer-Lambert law: Shining light on the obscure», *ChemPhysChem*, vol. 21, no 18, p. 2029, 2020, DOI: https://doi.org/10.1002/cphc. 202000464;

[MC85] D. C. McKean, A. R. Morrisson, I. Torto, M. I. Kelly, «Infrared studies of SiH stretching vibrations in some C-Si-H systems and effects of conformation, substitution and change of phase», *Spectrochim. Acta Part Mol. Spectrosc.*, vol. 41, no 1, p. 25-33, 1985, DOI: 10.1016/0584-8539(85)80081-7;

[MEI16] T. K. Meister, K. Riener, P. Gigler, J. Stohrer, W. A. Herrmann, F. E. Kühn, «Platinum Catalysis Revisited—Unraveling Principles of Catalytic Olefin Hydrosilylation», *ACS Catal.*, vol. 6, no 2, p. 1274-1284, 2016, DOI: 10.1021/acscatal.5b02624;

[ME13] G. Mera, E. Ionescu, «Silicon-Containing Preceramic Polymers», *Encyclopedia of Polymer Science and Technology*, American Cancer Society, 2013, DOI: https://doi.org/10.1002/ 0471440264.pst591;

[ME15] G. Mera, M. Gallei, S. Bernard, E. Ionescu, «Ceramic Nanocomposites from Tailor-Made Preceramic Polymers», *Nanomaterials*, vol. 5, no 2, p. 468-540, 2015, DOI: https://doi.org/10.3390/ nano5020468;

[ME20] T. Mezger, The rheology handbook, *Vincent Network*, 2020, ISBN: 978-374-860370-2;

[MI07] P. Miele, S. Bernard, D. Cornu, B. Toury, «Recent Developments in Polymer-Derived Ceramic Fibers (PDCFs): Preparation, Properties and Applications – A Review», *Soft Materials*, vol. 4, no 2-4, p. 249-286, 2007, DOI: 10.1080/15394450701310228;

[MI87] K. Minato, K. Fukuda, «Chemical vapor deposition of silicon carbide for coated fuel particles», *Journal of Nuclear Materials*, vol. 149, no 2, p. 233-246, 1987, DOI: 10.1016/0022-3115(87)90482-X;

[MI89] R. D. Miller, J. Michl, «Polysilane high polymers», *Chemical Reviews*, vol. 89, no 6, p. 1359-1410, 1989, DOI: https://doi.org/10.1021/cr00096a006;

[MO06] M. D. Morris, «Modern Raman Spectroscopy: A Practical Approach», *ACS Publications*, 2006, DOI: https://doi.org/10.1021/ac069338n;

[MO08] Z. Movasaghi, S. Rehman, D. I. ur Rehman, «Fourier transform infrared (FTIR) spectroscopy of biological tissues», *Applied Spectroscopy Reviews*, vol. 43, no 2, p. 134-179, 2008, DOI: https://doi.org/ 10.1080/05704920701829043;

[MO14] T. Van Mourik, M. Bühl, M.-P. Gaigeot, «Density functional theory across chemistry, physics and biology», *The Royal Society Publishing*, *Philos. Trans. A Math. Phys. Eng. Sci.,* 10;372, 20120488, 2014, DOI: 10.1098/rsta.2012.0488;

[MO94] H. Morkoc, S. Strite, G. B. Gao, M. E. Lin, B. Sverdlov, M. Burns, «Large-band-gap SiC, III-V nitride, and II-VI ZnSe-based semiconductor device technologies», *Journal of Applied physics*, vol. 76, no 3, p. 1363-1398, 1994, DOI: https://doi.org/10.1063/1.358463;

[MU00] A. Müller, P. Gerstel, M. Weinmann, J. Bill, F. Aldinger, «Correlation of boron content and high temperature stability in Si–B–C–N ceramics», *J. Eur. Ceram. Soc.*, vol. 20, no 14, p. 2655-2659, 2000, DOI: 10.1016/S0955-2219(00)00131-X;

[MU04] A. Müller, P. Gerstel, E. Butchereit, K. G. Nickel, F. Aldinger, «Si/B/C/N/Al precursor-derived ceramics: Synthesis, high temperature behavior and oxidation resistance», *J. Eur. Ceram. Soc*., vol. 24, no 12, p. 3409-3417, 2004, DOI: https://doi.org/10.1016/j.jeurceramsoc.2003.10.018;

[NA86] R. Naslain, F. Langlais, «CVD-Processing of Ceramic-Ceramic Composite Materials», *Tailoring Multiphase and Composite Ceramics*, R. E. Tressler, G. L. Messing, C. G. Pantano, R. E. Newnham, Éd. Boston, MA: *Springer* US, 1986, p. 145-164, DOI: 10.1007/978-1-4613-2233-7_12;

[NA98] R. Nagarajan, S. I. Chung, D. T. Wasan, «Biconical Bob Oscillatory Interfacial Rheometer», *Journal of Colloid and Interface Science*, vol. 204, no 1, p. 53-60, 1998, DOI: https://doi.org/10.1006/ jcis.1998.5583;

[NA99] M. Narisawa, A. Idesaki, S. Kitano, K. Okamura, M. Sugimoto, T. Seguchi, M. Itoh, «Use of blended precursors of poly (vinylsilane) in polycarbosilane for silicon carbide fiber synthesis with radiation curing», *Journal of the American Ceramic Society*, vol. 82, no 4, p. 1045-1051, 1999, DOI: https://doi.org/10.1111/j.1151-2916.1999.tb01871.x;

[OK06] K. Okamura, T. Shimoo, K. Suzuya, K. Suzuki, «SiC-based ceramic fibers prepared via organic-to-inorganic conversion process-A review», *Nippon Seramikkusu Kyokai Gakujutsu Ronbunshi*, vol. 114, no 1330, p. 445-454, 2006, DOI: https://doi.org/10.2109/jcersj.114.445;

[OM15] Z. Omidi, A. Ghasemi, S. R. Bakhshi, «Synthesis and characterization of SiC ultrafine particles by means of sol-gel and carbothermal reduction methods», *Ceramics International*, vol. 41, no 4, p. 5779-5784, 2015, DOI: 10.1016/j.ceramint.2015.01.005;

[OU10] T. Ouyang, C. Balan, «Modeling of Fiber Spinning Flows of Pre-ceramic Polymer Melts», *UPB Sci. Bull.*, Series B, vol. 72, no 4, 2010, ISSN: 1454-2358;

[PA15] A. Paar, «Basics of Rheology», *Luentomoniste. Luettu*, vol. 6, p. 2015, 2012;

[PH07] T. A. Pham, P. Kim, M. Kwak, K. Y. Suh, D.-P. Kim, «Inorganic polymer photoresist for direct ceramic patterning by photolithography», *Chemical Communications*, no 39, p. 4021-4023, 2007, DOI: https://doi.org/10.1039/B708480C;

[PI18] C. Piriou, L. Viers, R. Lucas, F. Bouzat, H. Laadoua, Y. Champavier, S. Foucaud, C. Coelho, F. Babonneau, «Rheological and thermal behaviours of a hyperbranched polycarbosilane», *Applied Organometallic Chemistry*, vol. 32, no 9, p. e4443, 2018, DOI: https://doi.org/10.1002/aoc.4443;

[PO02] Š. Podzimek, «A review of the analysis of branched polymers by SEC-MALS», *American Laboratory (USA)*, vol. 34, no 1, p. 38, 2002;

[PO11] Š. Podzimek, Light scattering, size exclusion chromatography and asymmetric flow field flow fractionation: powerful tools for the characterization of polymers, proteins and nanoparticles, *John Wiley & Sons*, 2011, ISBN: 978-047-038617-0;

[PO19] Š. Podzimek, «Multi-Angle Light Scattering: An Efficient Tool Revealing Molecular Structure of Synthetic Polymers», Volume 384, Issue 1, 1800174, 2019, DOI: https://doi.org/10.1002/masy.2018 00174;

[RA17] H. Rashid, A. Koel, T. Rang, R. Gähwiler, M. Grosberg, R. Jõemaa, «Nanoscale and microscale simulations of nn junction heterostructures of 3c-4h silicon carbide», *WIT Transactions on Engineering Sciences*, vol. 116, p. 235-248, 2017, DOI: 10.2495/MC170241;

[RA28] C. V. Raman, K. S. Krishnan, «A new type of secondary radiation», *Nature*, vol. 121, no 3048, p. 501-502, 1928, DOI: https://doi.org/10.1038/121501c0;

[RA95] V. Raman, O. P. Bahl, U. Dhawan, «Synthesis of silicon carbide through the sol-gel process from different precursors», *Journal of materials science*, vol. 30, no 10, p. 2686-2693, 1995, DOI: https://doi.org/10.1007/BF00362153;

[RE14] W. F. Reed, A. M. Alb, Monitoring polymerization reactions: from fundamentals to applications, *John Wiley & Sons*, 2014, ISBN 978-0-470-91738-1;

[RE58] M. Reiner, «Rheology», *Elasticity and Plasticity / Elastizität und Plastizität*, S. Flügge, Éd. Berlin, Heidelberg: Springer, p. 434-550, 1958, DOI: 10.1007/978-3-662-43081;

[RI06] R. Riedel, G. Mera, R. Hauser, A. Klonczynski, «Silicon-based polymer-derived ceramics: synthesis properties and applications-a review dedicated to Prof. Dr. Fritz Aldinger on the occasion of his 65th birthday», *Journal of the Ceramic Society of Japan*, vol. 114, no 1330, p. 425-444, 2006, DOI: https://doi.org/10.2109/jcersj.114.425;

[RI92] R. Riedel, G. Passing, H. Schönfelder, R. J. Brook, «Synthesis of dense silicon-based ceramics at low temperatures», *Nature*, vol. 355, no 6362, p. 714-717, 1992, DOI: https://doi.org/10.1038/355714a0;

[RI96] R. Riedel, W. Dressler, «Chemical formation of ceramics», *Ceramics International*, vol. 22, no 3, p. 233-239, 1996, DOI: https://doi.org/10.1016/0272-8842(95)00097-6;

[RI98] R. Riedel, L. M. Ruswisch, L. An, R. Raj, «Amorphous silicoboron carbonitride ceramic with very high viscosity at temperatures above 1500 C», *Journal of the American Ceramic Society*, vol. 81, no 12, p. 3341-3344, 1998, DOI: https://doi.org/10.1111/j.1151-2916.1998.tb02780.x;

[SA01] M. M. Samar, M. S. Neira, S. L. Resnik, A. Pacin, «Effect of fermentation on naturally occurring deoxynivalenol (DON) in Argentinean bread processing technology», *Food Additives & Contaminants*, vol. 18, no 11, p. 1004-1010, 2001, DOI: https://doi.org/10.1080/02652030110051284;

[SA04] S. E. Saddow, A. K. Agarwal, Advances in silicon carbide processing and applications, *Artech House*, 2004, ISBN: 1580537405;

[SA13] J. A. Salem, «Transparent Armor Ceramics as Spacecraft Windows», *Journal of the American Ceramic Society*, vol. 96, no 1, p. 281-289, 2013, DOI: 10.1111/jace.12089;

[SC01] D. Schawaller, B. Clauss, «Preparation of Non-Oxide Ceramic Fibers in the Systems Si-C-N and Si-B-C-N», *High Temperature Ceramic Matrix Composites*, p. 56–61, 2001;

[SC04] M. Schulz, M. Börner, J. Göttert, T. Hanemann, J. Haußelt, G. Motz, «Cross linking behavior of preceramic polymers effected by UV-and synchrotron radiation», *Advanced Engineering Materials*, vol. 6, no 8, p. 676-680, 2004, DOI: https://doi.org/10.1002/adem.200400082;

[SC13] F. Schröder, Si Silicon: System Si-C. SiC: Natural Occurrence. Preparation and Manufacturing Chemistry. Special Forms. Manufacture. Electrochemical Properties. Chemical Reactions. Applications. Ternary and Higher Systems with Si and C, *Springer Science & Business Media*, 2013;

[SH04] S. K. Shukla, R. K. Tiwari, A. Ranjan, A. K. Saxena, G. N. Mathur, «Some thermal studies of polysilanes and polycarbosilanes», *Thermochimica Acta*, vol. 424, no 1-2, p. 209-217, 2004, DOI: https://doi.org/10.1016/j.tca.2004.06.003;

[SI20] G. Simon, «Spectroscopies vibrationnelles: Théorie, aspects pratiques et applications», *Editions des archives contemporaines*, 2020;

[SM53] A. L. Smith, «The Infrared Spectra of the Methyl Chlorosilanes», *J. Chem. Phys.*, vol. 21, no 11, p. 1997-2004, 1953, DOI: 10.1063/1.1698730;

[SM60] A. L. Smith, «Infrared spectra-structure correlations for organosilicon compounds», *Spectrochim. Acta*, vol. 16, no 1, p. 87-105, 1960, DOI: 10.1016/0371-1951(60)80074-4;

[SM86] T. L. Smith Jr., «Process for the production of silicon carbide by the pyrolysis of a polycarbosilane polymer», 1986;

[SO13] S. Somiya, Handbook of advanced ceramics: materials, applications, processing, and properties, *Academic press*, 2013, ISBN: 978-0-12-385469-8;

[SR10] R. Sreeja, B. Swaminathan, A. Painuly, T. V. Sebastian, S. Packirisamy, «Allylhydridopolycarbosilane (AHPCS) as matrix resin for C/SiC ceramic matrix composites», *Materials Science and Engineering: B*, vol. 168, no 1-3, p. 204-207, 2010, DOI: https://doi.org/ 10.1016/j.mseb.2009.12.033;

[ST04] B. H. Stuart, Infrared spectroscopy: fundamentals and applications, *John Wiley & Sons*, 2004, ISBN: 9780470854273;

[SU04] T. Sun, R. R. Chance, W. W. Graessley, D. J. Lohse, «A study of the separation principle in size exclusion chromatography», *Macromolecules*, vol. 37, no 11, p. 4304-4312, 2004, DOI: https://doi.org/10.1021/ma030586k;

[TA16] J. Tajuelo, J. M. Pastor, M. A. Rubio, «A magnetic rod interfacial shear rheometer driven by a mobile magnetic trap», *Journal of Rheology*, vol. 60, no 6, p. 1095-1113, 2016, DOI: https://doi.org/ 10.1122/1.4958668;

[TA87] T. Taki, S. Maeda, K. Okamura, M. Sato, T. Matsuzawa, «Oxidation curing mechanism of polycarbosilane fibres by solid-state 29 Si high-resolution NMR», *Journal of materials science letters*, vol. 6, no 7, p. 826-828, 1987, DOI: 10.1007/BF01729026;

[TR02] S. Trassl, H.-J. Kleebe, H. Störmer, G. Motz, E. Rössler, G. Ziegler, «Characterization of the Free-Carbon Phase in Si-C-N Ceramics: Part II, Comparison of Different Polysilazane Precursors», *J. Am. Ceram. Soc.*, vol. 85, no 5, p. 1268-1274, 2002, DOI: https://doi.org/10.1111/j.1151-2916.2002.tb00256.x;

[VA06] C. Vahlas, B. Caussat, P. Serp, G. N. Angelopoulos, «Principles and applications of CVD powder technology», *Materials Science and Engineering: R: Reports*, vol. 53, no 1, p. 1-72, 2006, DOI: 10.1016/j.mser.2006.05.001;

[VA90] W. L. Vaughn, H. G. Maahs, «Active-to-passive transition in the oxidation of silicon carbide and silicon nitride in air», *Journal of the American Ceramic Society*, vol. 73, no 6, p. 1540-1543, 1990;

[VE74] W. Verbeek, G. Winter, «Formkoerper aus siliciumcarbid und verfahren zu ihrer herstellung», *DE Patent*, vol. 2236078, p. A1, 1974;

[VER74] W. Verbeek, «Production of shaped articles of homogeneous mixtures of silicon carbide and nitride», 1974;

[VR12] J. C. de Vries, «When does catalysis with transition metal complexes turn into catalysis by nanoparticles?», *ChemInform*, vol. 43, no 15, p. no, 2012, ISBN: 9783527635696;

[WA04] C. Wang, J. Wang, C. B. Park, Y.-W. Kim, «Cross-linking behavior of a polysiloxane in preceramic foam processing», *J. Mater. Sci.*, vol. 39, no 15, p. 4913–4915, 2004, DOI: 10.1023/B:JMSC.0000035335.92101.7c;

[WA19] Q. Wang, A. Shi, F. Shah, «Rheology instruments for food quality evaluation», *Evaluation Technologies for Food Quality*, Elsevier, p. 465-490, 2019, DOI: https://doi.org/10.1016/B978-0-12-814217-2.00018-4;

[WA20] Y. Wang, X. Li, X. Pei, L. He, Z. Huang, et Q. Huang, «Preparation of highly porous SiC via ceramic precursor conversion and evaluation of its thermal insulation performance», *Advances in Applied Ceramics*, vol. 119, no 7, p. 398-406, 2020, DOI: https://doi.org/10.1080/17436753.2020.1789940;

[WE00] M. Weinmann et al., «Synthesis and Thermal Behavior of Novel Si−B−C−N Ceramic Precursors», *Chem. Mater.*, vol. 12, no 3, p. 623-632, 2000, DOI: 10.1021/cm9910299;

[WE01] M. Weinmann, S. Nast, F. Berger, G. Kaiser, K. Müller, F. Aldinger, «Dehydrocoupling oftris(hydridosilylethyl)boranes with ammonia or amines: a novel route to Si-B-C-N preceramic polymers: Dehydrocoupling of tris(hydridosilylethyl)boranes», *Appl. Organomet. Chem.*, vol.15, no 10, p. 867-878, 2001, DOI: https://doi.org/10.1002/aoc.240;

[WE93] A. W. Weimer, K. J. Nilsen, G. A. Cochran, et R. P. Roach, «Kinetics of carbothermal reduction synthesis of beta silicon carbide», *AIChE Journal*, vol. 39, no 3, p. 493-503, 1993, DOI: 10.1002/aic.690390311;

[WE98] M. Weinmann, R. Haug, J. Bill, M. de Guire, et F. Aldinger, «Boron-modified polysilylcarbodiimides as precursors for Si–B–C–N ceramics: Synthesis, plastic-forming and high-temperature behavior», *Applied Organometallic Chemistry*, vol. 12, no 10-11, p. 725-734, 1998, DOI: 10.1002/(SICI)1099-0739(199810/11)12:10/11<725::AID-AOC777>3.0.CO;2-2;

[WI74] G. D. Winter, W. D. Verbeek, M. D. Mansmann, «Formkoerper aus homogenen mischungen von siliciumcarbid und siliciumnitrid und verfahren zu ihrer herstellung», *German patent* No DE2243527A1, 1974;

[WU02] H. J. Wu, L. V. Interrante, «Preparation of a polymeric precursor to silicon carbide via ring-opening polymerization: synthesis of poly[(methylchlorosilylene)methylene] and poly(silapropylene)», 2002. https://pubs.acs.org/doi/pdf/10.1021/cm00005a019 (consulté le avr. 23, 2021);

[WU89] H. J. Wu, L. V. Interrante, «Preparation of a polymeric precursor to silicon carbide via ring-opening polymerization: synthesis of poly [(methylchlorosilylene) methylene] and poly (silapropylene)», *Chemistry of Materials*, vol. 1, no 5, p. 564-568, 1989, DOI: https://doi.org/10.1021/ cm00005a019;

[WU92] H. J. Wu, L. V. Interrante, «Preparation of poly (dichlorosilaethylene) and poly (silaethylene) via ring-opening polymerization», *Macromolecules*, vol. 25, no 6, p. 1840-1841, 1992, DOI: https://doi.org /10.1021/ma00032a036;

[XI19] H. Xiong, L. Zhao, H. Chen, X. Wang, K. Zhou, D. Zhang, «3D SiC containing uniformly dispersed, aligned SiC whiskers: Printability, microstructure and mechanical properties», *Journal of Alloys and Compounds*, vol. 809, p. 151824, 2019, DOI: 10.1016/j.jallcom.2019.151824;

[YA75] S. Yajima, J. Hayashi, M. Omori, «Continuous silicon carbide fiber of high tensile strength», *Chem. Lett.*, vol. 4, no 9, p. 931-934, 1975, DOI: 10.1246/cl.1975.931;

[YA76] S. Yajima, K. Okamura, J. Hayashi, M. Omori, «Synthesis of Continuous Sic Fibers with High Tensile Strength», *Journal of the American Ceramic Society*, vol. 59, no 7-8, p. 324-327, 1976, DOI: https://doi.org/10.1111/j.1151-2916.1976.tb10975.x;

[YA78] S. Yajima, Y. Hasegawa, J. Hayashi, M. Iimura, «Synthesis of continuous silicon carbide fibre with high tensile strength and high Young's modulus», *J. Mater. Sci.*, vol. 13, no 12, p. 2569-2576, 1978, DOI: 10.1007/BF02402743;

[YAJ78] S. Yajima, Y. Hasegawa, K. Okamura, T. Matsuzawa, «Development of high tensile strength silicon carbide fibre using an organosilicon polymer precursor», *Nature*, vol. 273, no 5663, p. 525-527, 1978, DOI: 10.1038/273525a0;

[YU05] Y. Yu, P. J. DesLauriers, D. C. Rohlfing, «SEC-MALS method for the determination of long-chain branching and long-chain branching distribution in polyethylene», *Polymer*, vol. 46, no 14, p. 5165-5182, 2005, DOI: 10.1016/j.polymer.2005.04.036;

[ZI99] G. Ziegler, H.-J. Kleebe, G. Motz, H. Müller, S. Traßl, W. Weibelzahl, «Synthesis, microstructure and properties of SiCN ceramics prepared from tailored polymers», *Materials chemistry and physics*, vol. 61, no 1, p. 55–63, 1999, DOI: https://doi.org/10.1016/S0254-0584(99)00114-5;

[ZO16] A. Zocca, G. Franchin, H. Elsayed, E. Gioffredi, E. Bernardo, P. Colombo, «Direct ink writing of a preceramic polymer and fillers to produce hardystonite (Ca2ZnSi2O7) bioceramic scaffolds», *Journal of the American Ceramic Society*, vol. 99, no 6, p. 1960–1967, 2016, DOI: https://doi.org/10.1111/jace.14213;

Mise en forme de céramiques non-oxydes : vers une plateforme multi-analyse intégrée pour le suivi de la synthèse in situ de polycarbosilanes

Dans le domaine des céramiques non-oxydes, la voie des céramiques dérivées de polymères a constitué une avancée majeure pour obtenir des céramiques à base de carbure de silicium (SiC) à partir de polycarbosilanes. Afin de générer des céramiques pouvant être facilement mises en forme, la connaissance de la rhéologie des précurseurs précéramiques lors de la polymérisation est cruciale. Ainsi, dans le but de maîtriser la synthèse du polymère précéramique, il était primordial de suivre les changements structuraux survenant lors de la polymérisation d'un carbosilane, tout en accédant à ses propriétés rhéologiques. Pour répondre à cette problématique, une nouvelle plateforme a été développée, qui peut être divisée en deux parties. La première comprend un rhéomètre couplé à un spectromètre infrarouge à transformée de Fourier (FTIR) et un spectrophotomètre Raman (configuration Rheo-Raman-FTIR). La configuration Rheo-Raman-FTIR a permis en termes de spectroscopies vibrationnelles et de rhéologie le suivi d'une réaction de polymérisation in-situ en temps réel sous atmosphère et température contrôlées. La deuxième partie est la chromatographie d'exclusion stérique/diffusion de lumière à multi-angles (SEC-MALS). Cette technique a permis de caractériser la masse molaire moyenne des macromolécules formées lors de la polymérisation. Le lien entre ces deux parties a été réalisé grâce au taux de conversion des monomères obtenu dans chaque cas par la spectroscopie vibrationnelle (Raman/FTIR). Pour illustrer les intérêts de cette plateforme, une réaction d'hydrosilylation sera étudiée pour synthétiser avec succès un polycarbosilane hyperbranché, précurseur du SiC.

Mots-clés : hydrosilylation, spectroscopie Raman et infrarouge, polycarbosilane, rhéologie, carbure de silicium.

Non-oxide ceramic shaping: towards an integrated multi-analysis platform to monitor in-situ polycarbosilanes syntheses

In the area of non-oxide ceramics, the polymer-derived ceramic route was a breakthrough to obtain silicon carbide (SiC)-based ceramics from polycarbosilanes. To obtain ceramics that could be easily shaped, the knowledge of the rheology of the preceramic precursors during the polymerisation is crucial. Thus, to master the synthesis of the preceramic polymer, it was pivotal to monitor the structural changes occurring during the polymerization of a carbosilane, while accessing their rheological properties. To answer this issue, a new platform was developed that could be divided into two parts. The first one included a rheometer coupled to a Fourier transform infrared spectrometer (FTIR) and a Raman spectrophotometer (Rheo-Raman-FTIR setup). The Rheo-Raman-FTIR setup allowed for the monitoring in terms of vibrational spectroscopies and rheology of an in-situ polymerization reaction in real time at controlled atmosphere and temperature. The second part is the Size-Exclusion Chromatography/Multi Angle Light Scattering detector (SEC-MALS). This technique helped to characterise the average molar mass of the macromolecules formed during the polymerisation. The link between these two parts was made by the monomer conversion obtained in each case by vibrational spectroscopy (Raman/FTIR). To illustrate the interests of this original instrumental platform, a hydrosilylation reaction will be studied to successfully synthesise a hyperbranched polycarbosilane, precursor of SiC.

Keywords: hydrosilylation, Raman and infrared spectroscopy, polycarbosilane, rheology, silicon carbide.